United States Department of Commerce
National Institute of Standards and Technology

NISTIR 3952

STUDY OF STATIC AND DYNAMIC FRACTURE USING STRAIN MEASUREMENTS

John R. Berger
James W. Dally

NISTIR 3952

STUDY OF STATIC AND DYNAMIC FRACTURE USING STRAIN MEASUREMENTS

John R. Berger
James W. Dally

Materials Reliability Division
Materials Science and Engineering Laboratory
National Institute of Standards and Technology
Boulder, Colorado 80303-3328

September 1990

U.S. DEPARTMENT OF COMMERCE, Robert A. Mosbacher, Secretary
NATIONAL INSTITUTE OF STANDARDS AND TECHNOLOGY, John W. Lyons, Director

CONTENTS

LIST OF TABLES

LIST OF FIGURES

ABSTRACT

The analysis of strain fields surrounding both stationary and propagating cracks is presented. Series expansions of the static and dynamic strain fields are developed. Gage orientation angles are then studied to optimize the strain response. The orientation angles are found to be dependent on gage type and material.

Algorithms are developed which use the temporal or spatial strain variations to extract fracture parameters. The accuracy of the parameter determinations is shown to be excellent, and limits are placed on the validity of the developed methods. The methods are then applied to the analysis of a large-scale crack arrest test conducted in a pressure vessel steel. The behavior of the crack-tip position with time and the propagation toughness with time, temperature and position are determined. From this information, details of the conditions at crack arrest are extracted. The propagation toughness-crack-velocity relation is then constructed.

Key Words: crack arrest; dynamic fracture; fracture mechanics; propagation toughness; strain gages; stress intensity

CHAPTER 1
INTRODUCTION

Characterizing fracture in engineering materials requires measuring stress field quantities relevant to the type and mode of fracture and comparing them with the appropriate material property that describes the fracture resistance. In terms of driving force, which is the approach taken here, the characterization can be accomplished in terms of the stress intensity factor, K, for fracture that is primarily cleavage (or satisfies small-scale yielding criteria) or in terms of Rice's J-integral for ductile hole joining fractures. These quantities depend not only on the mode of fracture, that is, opening or forward shear modes for planar problems, but also on the extent of dynamic effects in the body.

Previous experimental approaches to the general problem of determining K or J in opaque materials have emphasized optical methods including reflection photoelasticity [1.1-1.3], caustics [1.4-1.6], and moire interferometry [1.7-1.9]. Additionally, methods using acoustic emission [1.10] and acoustic birefringence [1.11] have been employed. Most of these methods are full field measurements and are experimentally complex. The method of strain gages has started to receive attention only in recent years [1.3,1.12-1.18], although their use to determine K was suggested by Irwin more than thirty years ago [1.19].

Strain gage methods are extremely attractive in terms of experimental simplicity. However, since a measurement is made only at a material point specified by the gage position and not over an entire region, the strain field surrounding the crack tip must be well understood in order to position the gage properly for optimum response. Therefore, a necessary precursor to studying fracture behavior using strain gages is to investigate the strain field surrounding the crack tip.

In this report we first establish methodologies for analyzing the response of both single and multi-element strain gages near either a stationary or moving crack tip. Proof-of-concept investigations will be described for each of the developed analysis procedures. The developed methodologies will then be applied to two current topics in the mechanics of fracture: (1) determining crack arrest toughness and (2) the propagation toughness-crack speed constitutive relation in a nuclear pressure vessel steel.

1.1 THE PROPAGATION TOUGHNESS - CRACK SPEED CONSTITUTIVE RELATION AND CRACK ARREST

The general relationship between propagation toughness, K_{ID}, and crack speed, c, at constant temperature is illustrated in figure 1.1. Provided that linear elastic conditions prevail, that is, the one-parameter characterization of the stress intensity factor holds, the propagation toughness-crack speed relationship can be considered a constitutive law in the sense that it completely characterizes the dynamic fracture behavior of a material.

Based on extensive experimental data [1.20, 1.21] the K_{ID}-c relation is unique for a given material at a given temperature and is therefore independent of specimen size and geometry. Some evidence of nonuniqueness in K_{ID}-c relations has been presented in the literature [1.22-1.24]. However, in [1.22] extensive nonelastic deformation occurred during crack growth in the material being used, which invalidates the one-parameter characterization of linear elastic fracture mechanics. The experimental method of caustics employed in [1.23] and [1.24] has unresolved geometric effects which raises questions concerning the conclusions of this particular study [1.25].

Referring to figure 1.1, in region I on the K_{ID}-c curve, the

crack is propagating rapidly and large increases in driving force increase crack speed only a small amount. A terminal crack speed, c_T, is indicated in figure 1.1; above c_T the amount of energy going into the fracture process is so large that the crack branches in order to consume energy in the creation of multiple fracture surfaces. Although branching behavior is of interest in fragmentation and blasting studies, it is not of immediate interest for structural steels and will not be studied in this investigation.

In region II there is a transition in which increasing the driving force brings about a corresponding increase in crack speed. Finally, in region III small changes in driving force bring about very large changes in crack speed. The arrest toughness of the material can be found in region III where $c = 0$. It is in this context that crack arrest is viewed here; as a crack approaches arrest, a point on the K_{ID}-c curve is tracked from region I or II into region III and finally to arrest where $c = 0$.

The approach taken here toward crack arrest measurement falls between the fully dynamic approach advanced by Hahn and his co-workers at Battelle Columbus Laboratories (BCL) [1.26] and the static approach advanced by Crosley and Ripling at Materials Research Laboratory (MRL) [1.27]. The BCL approach accounts for the dynamics of the specimen through the use of reference curves generated from a finite-difference computer code for standard specimen geometries. The reference curves enable us to determine K_{ID} from the stress intensity at initiation, K_{Iq}, and the crack length at arrest. However, the crack-speed dependence of K_{ID} was not accounted for in the generation of the reference curves.

The MRL procedure for determining K_{Ia} uses the crack opening displacement (COD) measured approximately 1 ms after arrest and the final crack arrest length to predict K_{Ia} from an elasto-static equation. This procedure therefore assumes that the value of K determined 1 ms after arrest is not significantly different from

the value of K at arrest. Furthermore, the response of the COD may lag the events at the crack-tip by times exceeding the 1 ms interval [1.21]. The current ASTM standard for determining crack arrest toughness in ferritic materials is based on this static approach.

In either the BCL or MRL procedure for determining arrest toughness, measurements of the final crack length are combined with a "remote" variable (either a relatively low-frequency measurement of COD or a value of K_{Iq}) to determine K_{Ia}. However, in the approach developed here, K_{Ia} is determined at the moment of arrest from strains in the immediate vicinity of the arresting crack tip. This provides a more meaningful insight into the field surrounding the arresting crack. Although a dynamic (crack speed dependent) strain field is employed in portions of this study, the contribution of kinetic energy to the dynamic stress intensity is not accounted for as it is in a fully dynamic analysis. However, the manifestation of the energy return in terms of the resulting perturbation of the local strain field is used.

For brittle materials, crack propagation occurs by cleavage, and little plasticity develops near the propagating or arresting crack tip. Under these conditions of small scale plasticity, the linear elastic approach is entirely valid, and the strain gage methodologies developed in this dissertation can be applied directly to develop the K_{ID}-c relation.

The characterization of propagation toughness as a function of crack speed for a ductile, high toughness steel can be accomplished, to some extent, by the same methods used for the brittle material characterization. However, for a ductile material the problem is more complex due to the transition from cleavage to fibrous fracture modes in a run-arrest event, as well as mode change from fibrous to cleavage in initiation and post-arrest conditions. No attempt will be made here to characterize the ductile tearing portion of the fracture event

because the need to characterize the cleavage behavior is more critical.

As described in [1.28] and [1.29], cleavage fracture occurs in a ductile steel when the normal stress some distance ahead of the ductile, blunted crack tip reaches a critical value over a potential initiation site. For the pressure vessel steel analyzed in Chapter 5, the initiation site is usually at an inclusion or at a cluster of inclusions [1.28]. Once cleavage initiates, the crack runs at high speed with little plasticity, primarily due to the large strain rates (10^4 s^{-1} or more [1.30, 1.31]) near the crack tip and the associated increase in yield stress. For this portion of the fracture, linear elastic conditions prevail and the fracture analysis methodologies using strain gages may be directly applied.

As the crack slows to arrest, the strain rate near the crack tip decreases, the ability of the material to flow increases, and the plastic zone increases in size. At some point the plastic zone and the stresses and strains on its boundary are no longer fully described by the stress intensity factor--the fracture can no longer be analyzed by a linear elastic model. The question of whether the linear theory fails before or after the arrest event has recently been examined [1.32,1.33]. These studies concluded that cleavage conditions exist up to and including arrest. This result justifies the application of the methods developed in this dissertation to the analysis of cleavage crack run-arrest events in ductile steels. Once arrest occurs, the plastic zone size increases and, depending on testing machine compliance and the kinetic energy available in the specimen, the crack tip blunts and ductile tearing begins. Cleavage initiation may again occur after this point depending on the availability of suitable initiation sites.

1.2 OVERVIEW OF THE REPORT

In the chapters to follow we develop the tools necessary to analyze the strain field measured in the vicinity of a stationary or moving crack tip in order to extract fracture parameters. Since the stationary crack problem is considerably simpler, we concentrate on it first. Equations suitable for modeling the response of both single element strain gages and two-element strain gage rosettes are developed. An overdetermined analysis scheme for analyzing the strains in order to determine K_I values is then presented. The static methodology has potential use in the analysis of complex geometries such as structural components, where suitable expressions for the stress intensity factor are not available. Although finite element analysis can be employed to obtain this information, it is usually desirable to obtain some measure of experimental validation before proceeding with a fracture mechanics analysis.

The analysis of strains near a moving crack is presented next. We develop expressions for both single element and rosette strain gages using the strain field representation for a propagating crack. The orientation of the gage with respect to the crack path is studied in order to optimize the response in terms of the analysis. Two analysis schemes from which both the strain field parameters and crack-tip position are obtained are presented. Which algorithm to employ depends on the velocity gradient of the crack tip.

Due to the increased complexity of the dynamic problem, a separate chapter is devoted to several issues related to the strain analysis. The first issue concerns the extent of validity of the strain representation in terms of the distance of the gage from the crack tip. Using the results of this study, we specify limits on which gages to employ in the strain analysis.

The second issue concerns the determination of the crack tip

position when strain gage rosettes are used. There are data which were recorded during dynamic fracture experiments where rosettes which were not oriented to optimize the strain response were used. We study the difficulty in extracting crack tip position from these records as opposed to extracting the information from gages whose orientation is optimized. Finally, the accuracy of the crack tip determination is discussed.

The analysis of the dynamic crack problem is undertaken to determine arrest toughnesses as well as propagation toughness-crack speed relations. As discussed above, the arrest toughness determined by such a procedure is accomplished using information (strains) local to the arresting crack. This approach is certainly more attractive than inferring an arrest toughness from a more remote measurement. The methods developed for dynamic analysis are used to analyze the dynamic fracturing of a large-scale, wide-plate test of a nuclear pressure vessel steel. For this material, the propagation toughness-crack speed relation as well as the arrest toughness is determined.

REFERENCES

[1.1] Kobayashi,T., and Dally, J.W., "Dynamic Photoelastic Determination of the c-K Relation for 4340 Alloy Steel," **Crack Arrest Methodology and Applications**, ASTM STP 711, G.T. Hahn and M.F. Kanninen, Eds., American Society of Testing and Materials, 1980, pp. 189-210.

[1.2] Der, V.K., Barker, D.B., and Holloway, D.C.,"A Split Birefringent Coating Technique to Determine Dynamic Stress Intensity Factors," **Mechanics Research Communications**, Vol. 5, No.6, pp. 313-318 (1978).

[1.3] Shukla, A, Agarwal, R.K., and Nigam, H., "Dynamic Fracture Studies on 7075-T6 Aluminum and 4340 Steel Using Strain Gages and Photoelastic Coatings," **Engineering Fracture Mechanics**, Vol. 31, No. 3, pp. 501-515 (1989).

[1.4] Shockey, D., Kalthoff, J.F., Klemm, W., and Winkler, S., "Simultaneous Measurements of Stress Intensity for Fast Running Cracks in Steel," **Experimental Mechanics**, Vol. 23, No. 2., pp. 140-145 (1983).

[1.5] Ravi-Chandar, K., and Knauss, W.G., "An Experimental Investigation into Dynamic Fracture I: Crack Initiation and Arrest," **International Journal of Fracture**, Vol. 25, pp. 247-262 (1984).

[1.6] Rosakis, A.J., "Analysis of the Optical Method of Caustics for Dynamic Crack Propagation," **Engineering Fracture Mechanics**, Vol.13, No. 2, pp. 331-347 (1980).

[1.7] Epstein, J.S., Deason, V.A., and Reuter, W.G., "Dynamic Moire Interferometry Studies of Stress Wave/Crack Tip Diffraction Events in 1018 Steel," **Fracture Mechanics: Nineteenth Symposium**, ASTM STP 969, T.A. Cruse, Ed., American Society for Testing and Materials, pp. 482-503 (1988).

[1.8] Kang, B.S. and Kobayashi, A.S., "J Resistance Curves in Aluminum SEN Specimens Using Moire' Interferometry," **Experimental Mechanics**, Vol. 28, No. 2, pp. 154-158 (1988).

[1.9] Barker, D.B., Sanford, R.J. and Chona, R., "Determining K and Related Stress-Field Parameters from Displacement Fields," **Experimental Mechanics**, Vol. 25, No. 4, pp. 399-407 (1985).

[1.10] Dunegan, H.L., Harris, D.O., and Tatro, C.A., "Fracture Analysis by Use of Acoustic Emission," **Engineering Fracture Mechanics**, Vol. 1, No. 1, pp. 105-122 (1968).

[1.11] Clark, A.V., Mignogna, R.B., and Sanford, R.J., "Acousto-elastic Measurement of Stress and Stress Intensity Factors Around Crack Tips," **Ultrasonics**, March 1983, pp. 57-64.

[1.12] Dally, J.W. and Sanford, R.J., "Strain Gage Methods for Measuring the Opening Mode Stress Intensity Factor, K_I," **Experimental Mechanics**, Vol. 27, No. 4, pp. 381-388 (1988).

[1.13] Berger, J.R. and Dally, J.W., "An Overdeterministic Approach for Measuring K_I Using Strain Gages," **Experimental Mechanics**, Vol.28, No. 2, pp. 142-145 (1988).

[1.14] Dally, J.W. and Berger, J.R., "Determining K_I and K_{II} in a Mixed Mode Stress Field Using Strain Gages," **Proceedings 1986 SEM Spring Conference on Experimental Mechanics**, pp. 603-612, New

Orleans, LA.

[1.15] Dally, J.W. and Sanford, R.J., "On Measuring the Instantaneous Stress Intensity Factor for Propagating Cracks," Proceedings, **International Conference on Fracture Mechanics VII**, Houston, TX (1989).

[1.16] Dally, J.W., Sanford, R.J., and Berger, J.R., "An Improved Strain Gage Method for Measuring K(t) for a Propagating Crack," **Journal of Strain Analysis for Engineering Design**, Vol. 25, No. 3 (1990).

[1.17] Berger, J.R., Dally, J.W. and Sanford, R.J., "Determining the Dynamic Stress Intensity Factor with Strain Gages Using a Crack Tip Locating Algorithm," **Engineering Fracture Mechanics**, Vol. 36, No. 1, pp. 145-156 (1990).

[1.18] Read, D.T., "Analysis of Strains Measured During a Wide Plate Crack Arrest Test," **Proceedings of the 20th Session of the German Society for Materials Testing**, Working Group on Fracture, Frankfurt, Federal Republic of Germany (1988).

[1.19] Irwin, G. R., "Analysis of Stresses and Strains Near the End of a Crack Traversing a Plate," **ASME Journal of Applied Mechanics**, Vol. 24, No. 3, pp. 361-364 (1957).

[1.20] Fourney, W.L., Chona, R., and Sanford, R.J., "Dynamic Crack Growth in Polymers," **Workshop on Dynamic Fracture**, California Institute of Technology, pp. 75-99 (1983).

[1.21] Irwin, G. R., Kobayashi, T., Fourney, W.L., Metcalf, J. T., and Dally, J. W., "Photoelastic Studies of Crack Propagation

and Arrest in Polymers and 4340 Steel," **U.S. NRC Report**, NUREG/CR-0542, University of Maryland (1978).

[1.22] Dahlberg, L., Nilsson, F., and Brickstad, B., "Influence of Specimen Geometry on Crack Propagation and Arrest Toughness," **Crack Arrest Methodology and Applications**, ASTM STP 711, G.T. Hahn and M.F. Kanninen, Eds., American Society for Testing and Materials, pp. 211-227 (1980).

[1.23] Knauss, W.G. and Ravi-Chandar, K., "Fundamental Considerations in Dynamic Fracture," **Engineering Fracture Mechanics**, Vol. 23, No. 1, pp. 9-20 (1986).

[1.24] Takahashi, K. and Arakawa, K., "Dependence of Crack Acceleration on the Dynamic Stress Intensity Factor in Polymers," **Experimental Mechanics**, Vol. 27, No. 2, pp. 195-200 (1987).

[1.25] Kobayashi, T., discussion of reference [1.24], **Experimental Mechanics**, Vol. 27, No. 2, p. 200 (1987).

[1.26] Hahn, G.T., et. al., "A Cooperative Program for Evaluating Crack Arrest Testing Methods," **Crack Arrest Methodology and Applications**, ASTM STP 711, G.T. Hahn and M.F. Kanninen, Eds., American Society for Testing and Materials, 248-269 (1980).

[1.27] Crosley, P.B. and Ripling, E.J., "Comparison of Crack Arrest Methodologies," **Crack Arrest Methodology and Applications**, ASTM STP 711, G.T. Hahn and M.F. Kanninen, Eds., American Society for Testing and Materials, pp. 211-227 (1980).

[1.28] Heerens, J. and Read, D.T., "Fracture Behavior of a Pressure Vessel Steel in the Ductile-to-Brittle Transition Region," **National Institute of Standards and Technology Internal**

Report, NISTIR 88-3099, Boulder, CO, (1988).

[1.29] Ritchie, R.O., Knott, J.F., and Rice, J.R., "On the Relationship Between Critical Tensile Stress and Fracture Toughness in Mild Steels," **Journal of the Mechanics and Physics of Solids**, Vol. 21, pp. 395-410 (1973).

[1.30] Freund, L.B. and Hutchinson, J.W., "High Strain Rate Crack Growth in Rate Dependent Plastic Solids," **Journal of the Mechanics and Physics of Solids**, Vol. 33, No. 2, pp. 169-191 (1985).

[1.31] Freund, L.B., Hutchinson, J.W., and Lam, P.S., "Analysis of High Strain Rate Elastic Plastic Crack Growth," **Engineering Fracture Mechanics**, Vol. 23, No. 1, pp. 119-129 (1986).

[1.32] Naus, D.J., et. al., "Crack Arrest Behavior in SEN Wide Plates of Quenched and Tempered A533 Grade B Steel Tested Under Non-Isothermal Conditions," **U.S. NRC Report,** NUREG/CR-4930, Oak Ridge National Laboratory (1987).

[1.33] Fields, R.J. and deWit, R., "Plastic Zone Formation Around an Arresting Crack," **International Journal of Fracture**, Vol. 42, pp. 231-238 (1990).

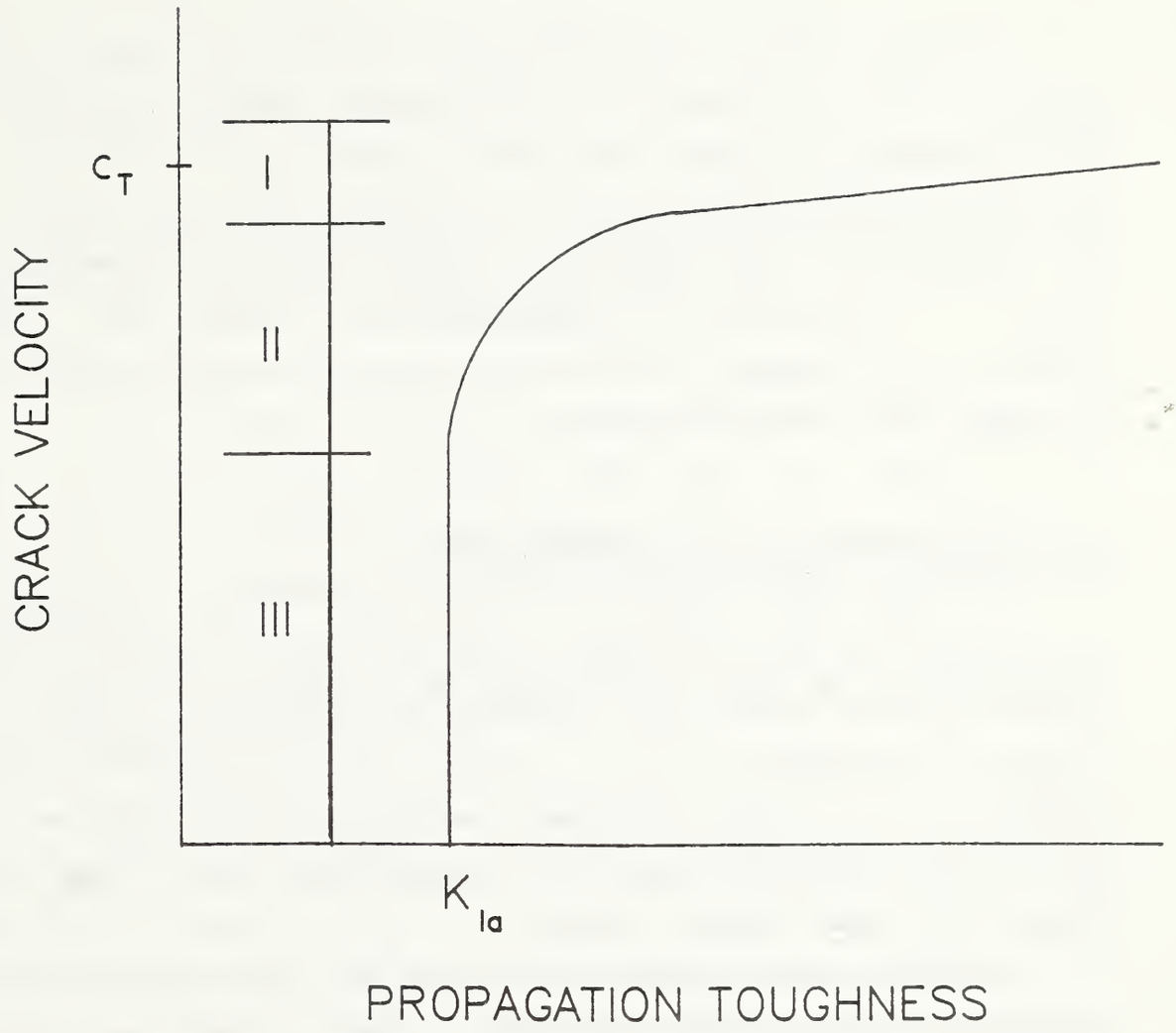

Fig. 1.1 General relationship between propagation toughness and crack velocity.

CHAPTER 2

STATIC ANALYSIS

In this section we consider the problem of analyzing the strain field surrounding a stationary crack subjected to time-independent loading. The strain field will be modeled using the generalized Westergaard series stress functions appropriate for single crack tips subjected to remote loading in opening mode (Mode I). The problem is formulated as a linear least squares problem in the unknown series coefficients which yields the stress intensity factor upon solution.

2.1 STATIC STRAIN FIELD REPRESENTATION

We begin the analysis of the static mode I problem by formulating the equations describing the strain sensed by a gage oriented at an angle, α, situated at a material point P as originally examined in [2.1], figure 2.1. In previous static analyses [2.2-2.4] the Westergaard method of analysis proved to be quite useful and convenient for representing the static stress field; it is used here as well.

As first demonstrated by Irwin [2.5], modifications to the original two-dimensional Westergaard equations are necessary to completely model two-dimensional, finite body, opening-mode crack problems. By re-examining the work of Sih [2.6] and Eftis and Liebowitz [2.7], Sanford [2.8] has shown that the most general form of the Westergaard equations for the finite body problem follows from an Airy stress function of the form

$$\phi = \mathrm{Re}\ \bar{\bar{Z}}(z) + y\ \mathrm{Im}\ \bar{Z}(z) + y\ \mathrm{Im}\ \bar{Y}(z) \tag{2.1}$$

where

$$Z(z) = \frac{d}{dz}\bar{\bar{Z}}(z) = \frac{d^2}{dz^2}\bar{\bar{Z}}(z), \tag{2.2}$$

$$Y(z) = \frac{d}{dz} \bar{Y}(z), \tag{2.3}$$

and

$$z = x + i\, y. \tag{2.4}$$

The function Z(z) is one of a family of Westergaard stress functions that have the required property

$$\text{Re } Z(z) = 0 \tag{2.5}$$

on the traction-free portions of the crack faces. The choice of Z(z) depends on the geometry and type of loading under consideration. Sanford and Berger [2.9] have described a methodology for choosing appropriate forms for Z(z) for the finite body problem.

The function Y(z) is a second complex-valued function which has the required property

$$\text{Im } Y(z) = 0 \qquad \text{on } y = 0. \tag{2.6}$$

This function is representative of the generalization of the Westergaard equations due to Sanford, since the most general solution to eq (2.6) is not a real constant as was selected in previous analyses [2.6,2.7]. Y(z) can be represented generally as a power series in z,

$$Y(z) = \sum_{m=0}^{\infty} B_m z^m \quad ; \quad \text{Im } B_m = 0 \tag{2.7}$$

since, on $y = 0$, Y(z) reduces to a power series in the real variable, x. For infinite body problems only the constant leading term B_0 is admissible for Y(z) to remain bounded at infinity.

The Cartesian stress components referred to a coordinate system situated at the crack tip are given in terms of Z(z) and Y(z) as

$$\sigma_{xx} = \text{Re } Z(z) - y \text{ Im } Z'(z) - y \text{ Im } Y'(z) + 2 \text{ Re } Y(z) \qquad (2.8)$$

$$\sigma_{yy} = \text{Re } Z(z) + y \text{ Im } Z'(z) + y \text{ Im } Y'(z) \qquad (2.9)$$

$$\sigma_{xy} = - y \text{ Re } Z'(z) - y \text{ Re } Y'(z) - \text{Im } Y(z), \qquad (2.10)$$

where the primes indicate derivatives with respect to the complex variable, z. Substituting eqs (2.8)-(2.10) in Hooke's law yields the strain field equations,

$$E\varepsilon_{xx} = (1 - \nu) \text{ Re } Z(z) - (1 + \nu) y \text{ Im } Z'(z) - (1 + \nu) y \text{ Im } Y'(z) + 2 \text{ Re } Y(z), \qquad (2.11)$$

$$E\varepsilon_{yy} = (1 - \nu) \text{ Re } Z(z) + (1 + \nu) y \text{ Im } Z'(z) + (1 + \nu) y \text{ Im } Y'(z) - 2 \nu \text{ Re } Y(z), \qquad (2.12)$$

$$\mu\gamma_{xy} = - y \text{ Re } Z'(z) - y \text{ Re } Y'(z) - \text{Im } Y(z), \qquad (2.13)$$

where E is Young's modulus and μ is the shear modulus.

The strain in the rotated coordinate system (x',y') shown in figure 2.1 can be found through the complex form of the strain transformation equation,

$$\varepsilon_{y'y'} - \varepsilon_{x'x'} + i \gamma_{x'y'} = e^{2i\alpha} (\varepsilon_{yy} - \varepsilon_{xx} + i \gamma_{xy}), \qquad (2.14)$$

and the first strain invariant,

$$\varepsilon_{y'y'} + \varepsilon_{x'x'} = \varepsilon_{yy} + \varepsilon_{xx}. \qquad (2.15)$$

Substituting eqs (2.11)-(2.13) in eqs (2.14) and (2.15), the strain field is

$$2\mu\varepsilon_{x'x'} = \frac{(1-\nu)}{(1+\nu)} \{ \text{Re } Z(z) + \text{Re } Y(z)\} - \{y \text{ Im } Z'(z) + y \text{ Im } Y'(z) - \text{Re } Y(z)\} \cos (2\alpha) - \{y \text{ Re } Z'(z) + y \text{ Re } Y'(z) + \text{Im } Y(z)\} \sin (2\alpha), \qquad (2.16)$$

$$2\mu\varepsilon_{y'y'} = \frac{(1-\nu)}{(1+\nu)} \{ \text{Re } Z(z) + \text{Re } Y(z)\} + \{y \text{ Im } Z'(z) + y \text{ Im } Y'(z) - \text{Re } Y(z)\} \cos(2\alpha) + \{y \text{ Re } Z'(z) + y \text{ Re } Y'(z) + \text{Im } Y(z)\} \sin(2\alpha), \quad (2.17)$$

$$\mu\gamma_{x'y'} = \{ y \text{ Im } Z'(z) + y \text{ Im } Y'(z) - \text{Re } Y(z) \} \sin(2\alpha) + \{ - y \text{ Re } Z'(z) - y \text{ Re } Y'(z) - \text{Im } Y(z) \} \cos(2\alpha). \quad (2.18)$$

Before developing the strain equations further a selection must be made for the form of the Westergaard function, Z(z). For purposes of this investigation the problem involves a single crack tip subjected to an arbitrary time-independent remote stress with no point forces acting on the crack faces or anywhere inside the body, figure 2.2. A suitable form for Z(z) for the finite body problem is

$$Z(z) = \sum_{j=0}^{\infty} A_j z^{j-1/2} \quad (2.19)$$

where $K_I = A_0 \sqrt{2\pi}$.

The series representations of eqs (2.7) and (2.19) involve an infinite number of terms to completely solve the finite body problem. However, if a small error is acceptable, we can truncate the series at a finite number of terms. In boundary collocation studies [2.10-2.12], the number of terms is large, since information is obtained only at the boundary. For experimental analysis the number of terms that must be retained is relatively small, since experimental data are obtained in the local region surrounding the crack tip. The method of obtaining the singular and nonsingular parameters from experimental near tip data has been termed "local collocation" [2.13-2.15] due to its

mathematical similarity to the boundary collocation method. Hybrid approaches incorporating both local and boundary collocation procedures have recently been developed by Kirk [2.16].

2.1.1 SINGLE-ELEMENT STRAIN GAGE

For a single-element strain gage coincident with the x'-axis of figure 2.1, the strain response of the gage, ε_g, using three-term expansions of eqs (2.7) and (2.19) is

$$\begin{aligned} 2\mu\varepsilon_g &= A_0 r^{-1/2} \{k \cos(\theta/2) - (1/2) \sin\theta \sin(3\theta/2) \cos(2\alpha) \\ &+ (1/2) \sin\theta \cos(3\theta/2) \sin(2\alpha)\} + B_0\{k + \cos(2\alpha)\} \\ &+ A_1 r^{1/2} \cos(\theta/2) \{k + \sin^2(\theta/2) \cos(2\alpha) \\ &- (1/2) \sin\theta \sin(2\alpha)\} + B_1 r \cos\theta \{(k + \cos(2\alpha)) \cos\theta \\ &- 2 \sin\theta \sin(2\alpha)\} + A_2 r^{3/2} \{k \cos(3\theta/2) \\ &- (3/2) \sin\theta \sin(\theta/2) \cos(2\theta) - (3/2) \sin\theta \cos(\theta/2) \sin(2\alpha)\} \\ &+ B_2 r^2 \{k \cos(2\theta) - 2 \sin^2\theta \cos(2\alpha) - 2 \sin\theta \cos\theta \sin(2\alpha) \\ &- \cos(2\theta - 2\alpha)\}, \end{aligned} \tag{2.20}$$

where $k = (1 - \nu)/(1 + \nu)$. For brevity we introduce the notation

$$2\mu\varepsilon_g = A_0 f_0 + B_0 g_0 + A_1 f_1 + B_1 g_1 + A_2 f_2 + B_2 g_2, \tag{2.21}$$

where the f_j and g_j are separable functions of r and θ given above.

2.1.2 STRAIN GAGE ROSETTE

In some applications it is desired to compensate the strain gage response for temperature. This can easily be accomplished using a strain gage rosette with its individual sensors connected to adjacent arms of the Wheatstone bridge. For this case the gage response, ε_g, is the difference in strains $\varepsilon_{y'y'} - \varepsilon_{x'x'}$:

$$2\mu(\varepsilon_{y'y'}-\varepsilon_{x'x'}) = (1/2)\ A_0 r^{-1/2} \sin\theta \{ \sin(3\theta/2) \cos(2\alpha) - \cos(3\theta/2) \sin(2\alpha)\} - B_0 \cos(2\alpha) + (1/2)\ A_1 r^{1/2} \sin\theta \{\cos(\theta/2) \sin(2\alpha) - \sin(\theta/2) \cos(2\alpha)\} + B_1 r \{ 2 \sin\theta \sin(2\alpha) - \cos\theta \cos(2\alpha) \} + (3/2)\ A_2 r^{3/2} \sin\theta \{ \sin(\theta/2) \cos(2\alpha) + \cos(\theta/2) \sin(2\alpha)\} + B_2 r^2 \{2 \sin^2\theta \cos(2\alpha) + 2 \sin\theta \cos\theta \sin(2\alpha) - \cos(2\theta + 2\alpha)\}. \quad (2.22)$$

When eq (2.22) is written in the form of eq (2.21), the f_j and g_j are obtained from eq (2.22).

2.2 OVERDETERMINED ANALYSIS

Dally and Sanford [2.1] previously described a single-gage technique for the static mode I case where the gage is positioned at an orientation angle, α, determined by

$$\cos 2\alpha = -(1 - \nu)/(1 + \nu) \quad (2.22)$$

to eliminate the B_0 contribution and positioned along a radial line at an angle θ determined by

$$\tan(\theta/2) = \cos 2\alpha \quad (2.23)$$

to eliminate the A_1 contribution. The stress intensity factor, K_I, is then given to three-term accuracy by

$$K_I = \sqrt{(8/3)\pi r_g}\ E\ \varepsilon_g \quad (2.24)$$

where r_g is the radial position to the gage and ε_g is the strain sensed by the gage.

The present single-gage analysis builds on the results described above to eliminate two constraints associated with the original approach. By increasing the order of the series representation from three terms to six terms, we enlarge the field of data acquisition, and prior knowledge of the extent of validity of a three-term model is not required. Second, using a large number of gages positioned farther from the crack tip eliminates the need for a plastic zone correction.

The six undetermined coefficients in eq (2.21) can be determined by analyzing the data taken from gages oriented at various angles around the crack tip. The orientation angles for the gages are determined by eqs (2.22) and (2.23). Provided that a sufficient number of data points are obtained to ensure adequate redundancy, a system of equations linear in the unknown coefficients can be formed. The linear problem can then be solved directly in a least squares sense.

For n strain sensors eq (2.21) can be applied repeatedly to form the system

$$2\mu\varepsilon_{g_1} = A_0 f_{0_1} + B_0 g_{0_1} + A_1 f_{1_1} + B_1 g_{1_1} + A_2 f_{2_1} + B_2 g_{2_1}$$

. . . . . (2.25)

$$2\mu\varepsilon_{g_n} = A_0 f_{0_n} + B_0 g_{0_n} + A_1 f_{1_n} + B_1 g_{1_n} + A_2 f_{2_n} + B_2 g_{2_n}$$

or equivalently in matrix form

$$\mathbb{D}\,\mathbf{c} = \mathbf{b}, \qquad (2.26)$$

where $\mathbf{c}$ is the vector containing the unknown coefficients. Traditionally, linear least squares problems of the type given by eq (2.26) are solved through the formation of the normal equations,

$$\hat{\mathbf{c}} = (\mathbb{D}^T \mathbb{D})^{-1} \mathbb{D}^T \mathbf{b}, \tag{2.27}$$

which can be shown to minimize the Euclidean norm of the residual vector [2.18], $\| \mathbf{r} \|_2$, where

$$\mathbf{r} = \mathbf{b} - \mathbb{D} \hat{\mathbf{c}} \tag{2.28}$$

and $\hat{\mathbf{c}}$ is the least squares estimate of $\mathbf{c}$. Appendix A includes a formal discussion of the linear least squares problem and a derivation of the solution given by eq (2.27).

Alternative solutions of systems of equations of the type given by eq (2.26), based on orthogonal transformations, have been found to have broader application in linear least squares theory [2.19, 2.20]. Specifically, the normal equations tend to exhibit numerical instabilities when either the row-space or column-space dimension of the coefficient matrix $\mathbb{D}$ becomes large. One such orthogonalization process is the QR decomposition. The theory of the QR decomposition is detailed in [2.21] and summarized in Appendix A. The decomposition was implemented using the Linpack collection of FORTRAN subroutines [2.22].

2.3 EXPERIMENTAL VERIFICATION

A compact tension specimen with W = 305 mm was fabricated from a 6.4 mm thick plate of 6061-T6 aluminum for verifying the analysis procedure described above. A simulated crack of length 153 mm was machined into the specimen, providing an a/W ratio of 0.5. For aluminum, Poisson's ratio is 0.33, and the orientation angles are equal: $\alpha = \theta = 60^\circ$. Since for this case the strain $\varepsilon_{x'x'}$ is equivalent to the radial strain ε_{rr}, the specimen was instrumented with 10-element strip strain gages with active gage lengths of 1.6 mm on 2.0 mm centers positioned at $\theta = 0^\circ$, 45°, and 90° to provide 30 data points for the analysis. The strip gages were located 5.8 mm, 11.1 mm, and 4.6 mm from the crack tip, respectively. The specimen geometry and gage layout are shown in

figure 2.4.

The specimen was loaded in a servo-hydraulic closed-loop material-test system. Strains were recorded at 1780 N loading increments to a maximum load of 8900 N. The strain distributions at maximum load are shown in figure 2.5 for each of the strip gages. Only 29 data points are shown on the graph, because one element was damaged during installation or testing and was not functioning.

The overdetermined analysis was implemented in two ways. First, only the data corresponding to the actual gage readings were used to form the system of equations given by eq (2.25). The order of the model was increased sequentially up to a maximum of six parameters. The results of each analysis are presented in table 2.1. The value of K_I is obtained with relatively low error regardless of the number of terms retained in the model. The results of the two- and three-parameter models provide the lowest error in estimating K_I, while the largest errors were obtained for the five- and six-parameter models.

A second overdetermined analysis was performed using the smooth distributions of strains shown in figure 2.5. Data from the curves were obtained at 2.5 mm increments in radial position, r, to increase the number of data points from 29 to 48. This increased the redundancy in the analysis from five to eight. The results of the second analysis are presented in table 2.2. Clearly, the degree of redundancy was adequate in the first analysis, and no further improvement in calculating K_I was obtained.

Values of the first five nonsingular coefficients for the specimen geometry employed here were previously determined by Chona [2.17] using photoelasticity. For the six-parameter analyses performed above we would expect to obtain reliable results for the values of the first three coefficients. The values of B_0 and A_1 obtained through the strain field analysis are

compared with Chona's values in table 2.3. Examination of the results indicates that the value of B_0 obtained with a fifth-order model compares favorably with Chona's value. However, the value of A_1 does not compare well with the photoelastically determined value, even though the coefficient value has stabilized.

To examine the reason for failing to accurately obtain the value of A_1, Chona developed a plot showing areas in the field where one-, two-, three- and four-parameter models can be used to describe the strains to within five percent accuracy. The comparison is based on the six-parameter solution of Chona. Presented in [2.24], this plot indicates that the regions in which the gages were positioned were insensitive to the value of A_1. For the gages positioned on $\theta = 45^\circ$ and 90° the strain field is adequately described by one or two parameters. The data taken along $\theta = 0^\circ$ do require a three-parameter model for an accurate description of the strain field; however, the coefficient multiplying the A_1 term when $\theta = 0^\circ$ is $(r^{1/2}/2)$ which is too weak in comparison to the multipliers of A_0, $(r^{-1/2}/2)$, and B_0, $(3r^0/2)$, to strongly influence the results.

The analysis developed in this section is accurate enough to evaluate fracture parameters obtained from strain gages within engineering accuracy. The value of the first nonsingular coefficient, B_0, was obtained as well. This coefficient is of interest since it is relates directly to the value of the constant stress acting parallel to the crack faces. The value of A_1 was not obtained to sufficient accuracy from the strain field measurements primarily due to the positioning of the gages.

REFERENCES

[2.1] Dally, J.W. and Sanford, R. J., "Strain-Gage Methods for Measuring the Opening-Mode Stress Intensity Factor, K_I," **Experimental Mechanics**, Vol. 27, No. 4, pp. 381 - 388 (1987).

[2.2] Chona, R., Irwin, G.R., and Sanford, R.J., "Influence of Specimen Size and Shape on the Singularity-Dominated Zone," **Fracture Mechanics: Fourteenth Symposium-Volume I: Theory and Analysis**, ASTM STP 791, J.C. Lewis and G. Sines, Eds., American Society for Testing and Materials, pp. I-3 - I-23 (1983).

[2.3] Wah, T., "Stress Intensity Factors Determined by Use of Westergaard's Stress Functions,", **Engineering Fracture Mechanics**, Vol. 20, No. 1, pp. 65-73 (1984).

[2.4] Clark, A.V., Mignogna, R.B. and Sanford, R.J., "Acousto-elastic Measurement of Stress Intensity Factors Around Crack Tips," **Ultrasonics**, March, 1982, pp. 57 - 64.

[2.5] Irwin, G.R., Discussion of: "The Dynamic Stress Distribution Surrounding a Running Crack - a Photoelastic Analysis," **Proceedings SESA**, XVI, pp. 93-96 (1958).

[2.6] Sih, G.C., "On the Westergaard Method of Crack Analysis," **International Journal of Fracture Mechanics**, Vol. 2, pp. 628-631 (1966).

[2.7] Eftis, J. and Liebowitz, H., "On the Modified Westergaard Equations for Certain Crack Problems," **International Journal of Fracture Mechanics**, Vol. 8, pp. 383-392 (1972).

[2.8] Sanford, R.J., "A Critical Re-Examination of the Westergaard

Method for Solving Opening-Mode Crack Problems," **Mechanics Research Communications**, Vol. 6, pp. 289-294 (1979).

[2.9] Sanford, R.J. and Berger, J.R., "The Numerical Solution of Opening Mode Finite Body Fracture Problems Using Generalized Westergaard Functions," **Engineering Fracture Mechanics** (In Press).

[2.10] Newman, J.C., "Stress Analysis of the Compact Tension Specimen Including the Effects of Pin Loading," **Fracture Analysis**, ASTM STP 560, American Society for Testing and Materials, pp. 105-121 (1974).

[2.11] Srawley, J.E. and Gross, B., "Stress Intensity Factors for Crackline Loaded Edge Crack Specimens," **Materials Research and Standards**, Vol. 7, No. 4, pp. 155-162 (1967).

[2.12] Pei-Qing, P., "Stress Intensity Factors for a Rectangular Plate with a Point-Loaded Edge Crack by a Boundary Collocation Procedure, and an Investigation into the Convergence of the Solution," **Engineering Fracture Mechanics**, Vol. 22, No. 2, pp. 295-305 (1985).

[2.13] Sanford, R.J. and Link, R.E., "Local Collocation - A Hybrid Technique in Fracture Mechanics," **Proceedings SECTAM XII**, The Southeastern Conference on Theoretical and Applied Mechanics, 1984.

[2.14] Sanford, R.J. and Chona, R., "Photoelastic Calibration of the Short-Bar Chevron-Notch Specimen," **Chevron-Notched Specimens: Testing and Stress Analysis**, ASTM STP 855, J.H. Underwood, S.W. Freiman, and F.I. Baratta, Eds., American Society for Testing and Materials, Philadelphia, pp. 81-97 (1984).

[2.15] Sanford, R.J., "Determining Fracture Parameters with Full Field Optical Methods," **Experimental Mechanics**, Vol. 29, No. 3, pp. 241-247 (1989).

[2.16] Kirk, M.T., **A Hybrid Collocation Technique for Solution of the Finite Body Single Ended Crack Problem**, M.S. Thesis, University of Maryland, 1989.

[2.17] Chona, R., **Non-Singular Stress Effects in Fracture Test Specimens - A Photoelastic Study**, M.S. Thesis, University of Maryland, 1985.

[2.18] Leon, S.J., **Linear Algebra with Applications**, Macmillan Publishing Company, New York, NY, 1980.

[2.19] Eason, E., "A Review of Least Squares Methods for Solving Partial Differential Equations," **International Journal for Numerical Methods in Engineering**, Vol. 10, pp. 1021-1046 (1976).

[2.20] Longley, J.W., **Least Squares Computations Using Orthogonalization Methods**, Marcel Dekker, Inc., New York, NY, 1984.

[2.21] Stewart, G.W., **Introduction to Matrix Computations**, Academic Press, Inc., New York, NY, 1973.

[2.22] Dungarra, J.J., Moler, C.B., Bunch, J.R., and Stewart, G.W., **Linpack Users Guide**, Society for Industrial and Applied Mathematics, 1979.

[2.23] ASTM E 399-83, "Standard Test Method for Plane-Strain Fracture Toughness of Metallic Materials," **1989 Annual Book of ASTM Standards**, Vol. 03.01, American Society of Testing and

Materials, Philadelphia, Pennsylvania (1989).

[2.24] Berger, J. R., and Dally, J. W., "An Overdeterministic Approach for Measuring K_I Using Strain Gages," **Experimental Mechanics**, Vol. 28, No. 2, pp. 142-145 (1988).

Table 2.1

Results for K_I with 29 strain gage readings.

Parameters	K_I (Mpa $\sqrt{m}$)	$\bar{r}$ ($\mu\varepsilon$)	Error* (%)
A_0	25.4	1033.6	3.59
A_0, B_0	24.4	290.1	-0.45
A_0, B_0, A_1	24.8	229.8	1.35
A_0, B_0, A_1, B_1	25.2	168.3	2.69
A_0, B_0, A_1, B_1, A_2	25.4	139.7	3.59
A_0, B_0, A_1, B_1, A_2, B_2	25.8	121.1	5.38

*K_I = 24.5 Mpa $\sqrt{m}$ from [2.23]

Table 2.2

Results for K_I with 48 data points.

Parameters	K_I (Mpa $\sqrt{m}$)	$\bar{r}$ ($\mu\varepsilon$)	Error* (%)
A_0	25.3	1049.8	3.14
A_0, B_0	24.3	272.9	-0.90
A_0, B_0, A_1	24.7	224.0	0.90
A_0, B_0, A_1, B_1	25.1	166.7	2.24
A_0, B_0, A_1, B_1, A_2	25.4	126.2	3.59
A_0, B_0, A_1, B_1, A_2, B_2	25.7	121.9	4.93

*K_I = 24.5 Mpa $\sqrt{m}$ from [2.23]

Table 2.3

Comparison of higher order coefficients (48 data points).

No. of Parameters	B_0 (MPa)	Error (%)	A_1 (MPa·$m^{-1/2}$)	Error (%)
2	6.51	33.1	--	--
3	9.81	0.9	-100.4	-21.9
4	11.1	14.2	-156.6	22.0
5	9.49	-2.1	-157.5	22.6
6	9.17	-5.7	-161.8	25.9

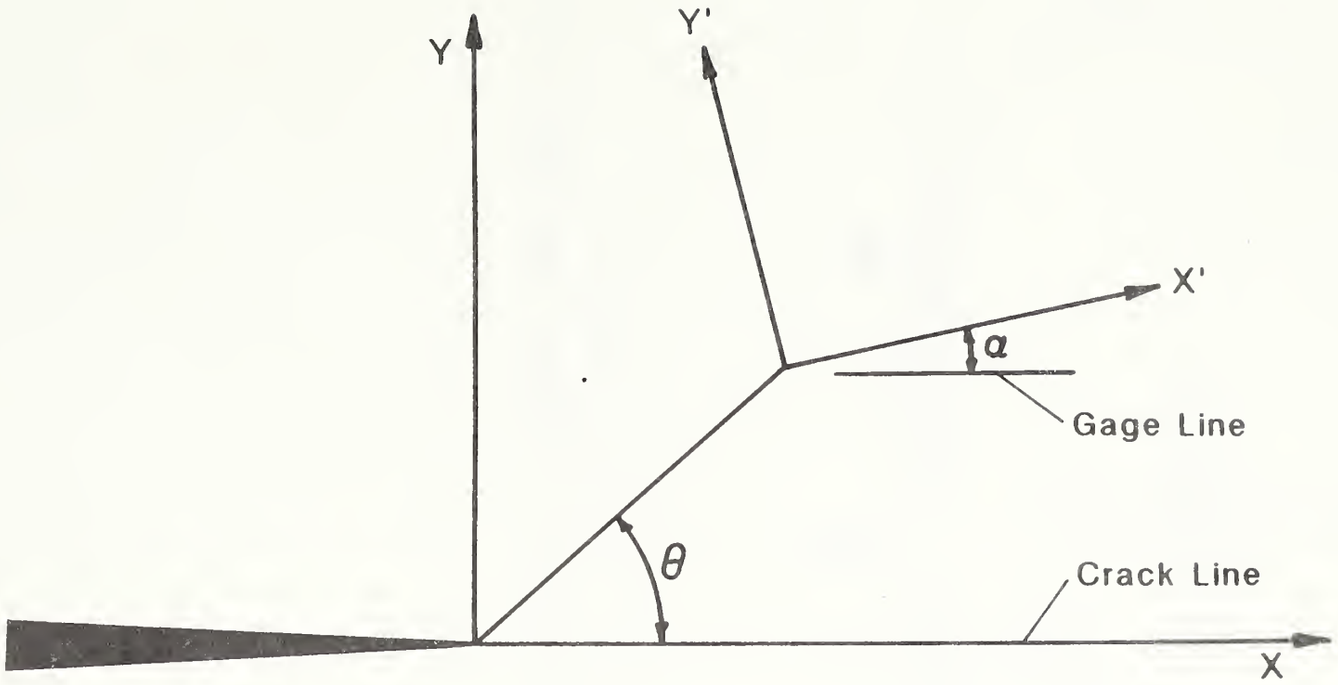

Fig. 2.1 Definition of the rotated coordinate system.

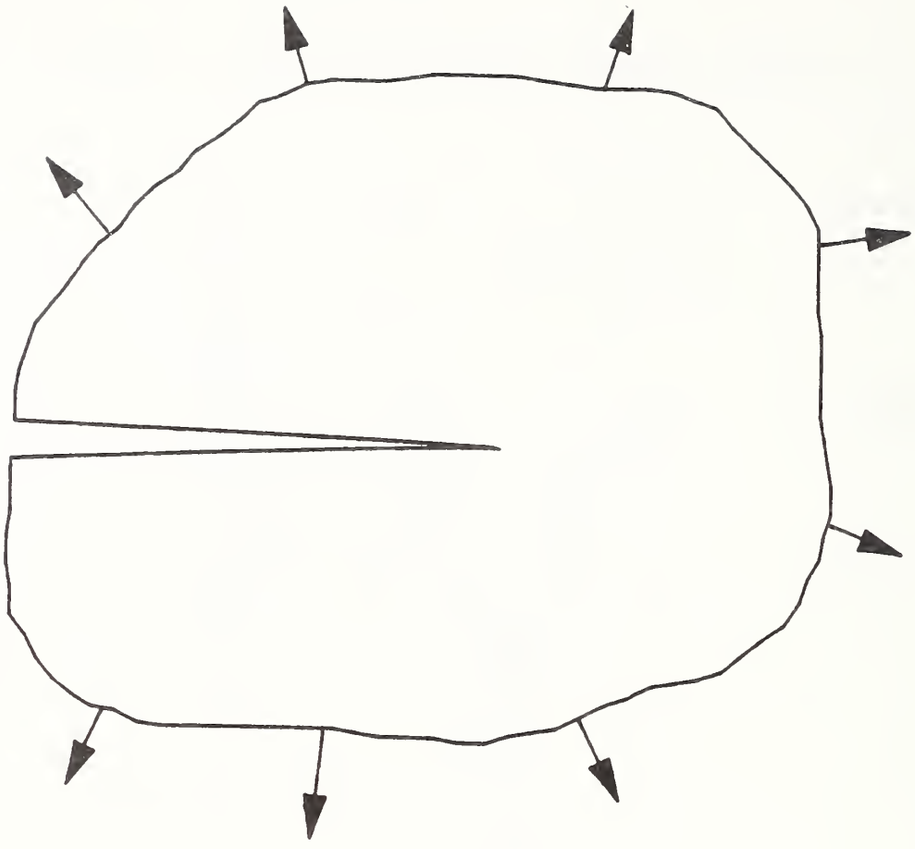

Fig. 2.2 Single crack tip, infinite body fracture problem.

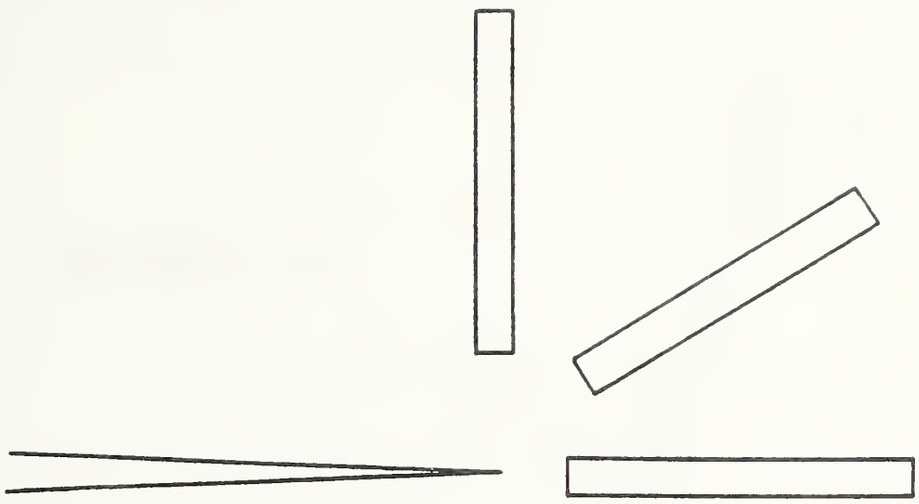

Fig. 2.3 Strip gage locations for the Al 6061-T6 compact specimen

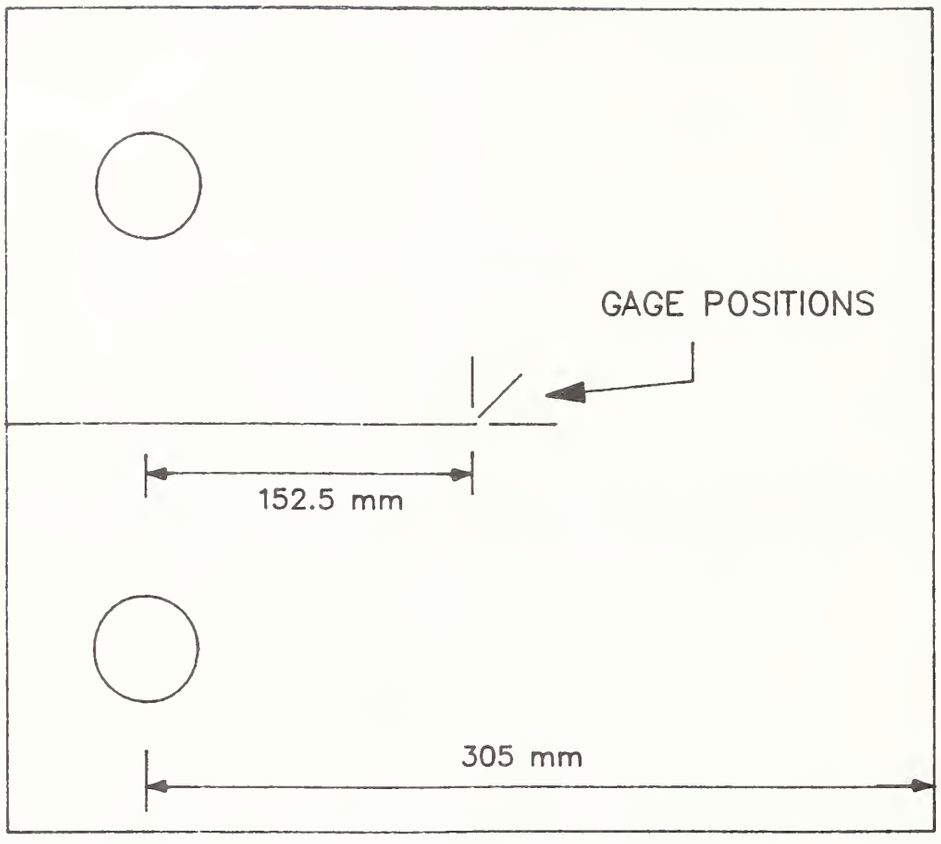

Fig. 2.4 Geometry of the Al 6061-T6 compact specimen.

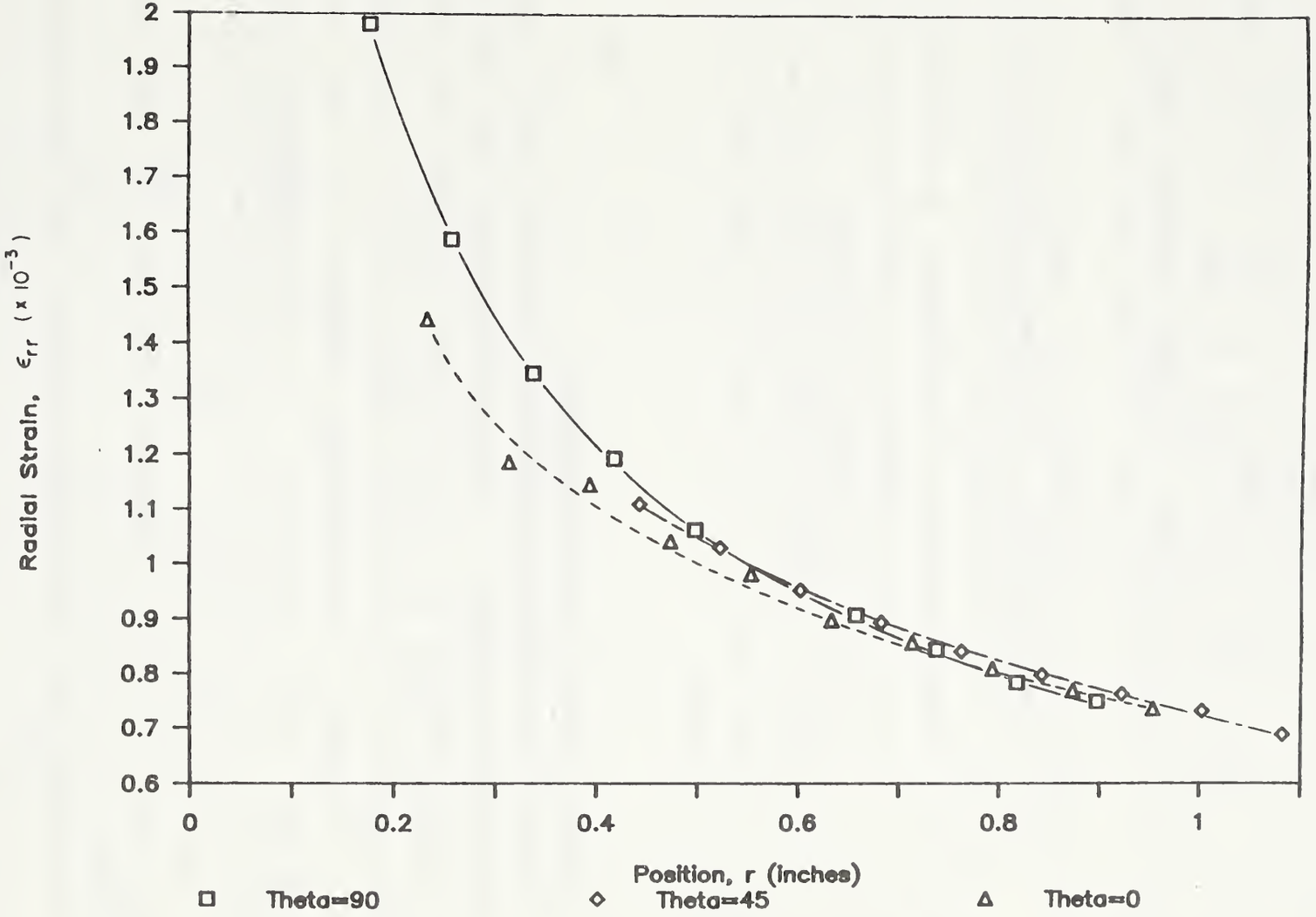

Fig. 2.5 Experimentally recorded radial strain distributions for the Al 6061-T6 compact specimen.

CHAPTER 3
DYNAMIC ANALYSIS

The analysis of the strain field surrounding a propagating crack subjected to time-independent loading will be considered in this section. A series solution to the mode I problem will be used to examine the strain field in order to optimize the positioning of the strain gage. Analysis procedures based on the temporal and spatial variations of strain sensed by a gage or series of gages will be developed.

Unlike the static problem, the dynamic problem is inherently non-linear due to the unknown position of the crack tip at a given time. For a temporal approach to the analysis, an algorithm which uses both iteration and triangulation to determine the crack tip position and the series coefficients is developed. For a spatial analysis approach, a modified version of the nonlinear least squares technique similar to that used in photoelastic analysis [3.1] will be used.

3.1 DYNAMIC STRAIN FIELD REPRESENTATION

We begin the analysis by considering which solution to employ for the dynamic problem. It must be recognized that there are three separate types of dynamic fracture problems: a stationary crack subjected to time-dependent loading [3.2-3.7], a propagating crack subjected to time-dependent loading [3.6 -3.9], and a propagating crack subjected to time-independent loading [3.10-3.15]. Here we concentrate on a propagating crack subjected to time-independent loading. This analysis has been used extensively for crack propagation analyses and crack arrest analyses [3.10, 3.11, 3.22-3.24].

The assumption of constant velocity and time-independent loading allows us to transform the time-dependent portion of the

equations of motion to the spatial variable in the direction of crack propagation. A series solution technique can then be employed to satisfy the elastic field equations and boundary conditions. Without assuming constant velocity, the transformation of variables cannot take place and series solutions cannot be employed [3.16]. Although several solutions have been advanced [3.10,3.12-3.15] for the constant velocity crack problem, the solution of Irwin [3.14] maintains many of the advantages of the Westergaard method of analysis for static problems and is used here.

Irwin used a dynamic transformation of the y-coordinate for a coordinate system attached to the moving crack tip given by

$$y_1 = \lambda_1 y, \tag{3.1}$$

$$y_2 = \lambda_2 y, \tag{3.2}$$

with the velocity dependent functions λ_1 and λ_2 defined as

$$\lambda_1 = \sqrt{1 - (c/c_1)^2}\ , \tag{3.3}$$

$$\lambda_2 = \sqrt{1 - (c/c_2)^2}\ , \tag{3.4}$$

where c_1 and c_2 are the longitudinal and shear wave speeds, respectively, and c is the crack speed (for plane stress problems, the plate wave speed is used for c_1). The dilatation, Δ, and rotation, ω, defined by

$$\Delta = \frac{\partial u}{\partial x} + \frac{\partial v}{\partial y}\ , \tag{3.5}$$

$$\omega = \frac{\partial v}{\partial x} - \frac{\partial u}{\partial y}\ , \tag{3.6}$$

can then be written as harmonic functions in the transformed

variables,

$$\nabla_1^2 \Delta = 0, \tag{3.7}$$

$$\nabla_2^2 \omega = 0, \tag{3.8}$$

where the notation,

$$\nabla_j^2 = \frac{\partial^2}{\partial x^2} + \frac{\partial^2}{\partial y_j^2} \; ; \; j = 1, \; 2, \tag{3.9}$$

has been used. By noting the form of the dilatation and rotation from the static analysis, the dynamic forms can be expressed as

$$\Delta = \rho \; (1 - \lambda_1^2) \; \text{Re} \; \Gamma_1(z_1), \tag{3.10}$$

$$\omega = \varphi \; (1 - \lambda_2^2) \; \text{Re} \; \Gamma_2(z_2). \tag{3.11}$$

The analytic functions $\Gamma_1(z_1)$ and $\Gamma_2(z_2)$ are complex-valued stress functions of the velocity transformed variables z_1 and z_2 defined by

$$z_k = x + i \; y_k \; ; \; k = 1, \; 2 \tag{3.12}$$

as shown in figure 3.1. The exact form of the stress functions depends on the geometry of the problem under consideration. The constants, ρ and φ, are to be determined after a suitable selection for the stress functions has been made.

Following an integration procedure and introducing Hooke's law, the stresses can be calculated as

$$\sigma_{xx} = \mu \; \{\rho \; (1 + 2\lambda_1^2 - \lambda_2^2) \; \text{Re} \; \Gamma_1 - 2\varphi\lambda_2 \; \text{Re} \; \Gamma_2\}, \tag{3.13}$$

$$\sigma_{yy} = \mu \; \{-\rho \; (1 + \lambda_2^2) \; \text{Re} \; \Gamma_1 + 2\varphi\lambda_2 \; \text{Re} \; \Gamma_2\}, \tag{3.14}$$

$$\sigma_{xy} = \mu \; \{-2\rho\lambda_1 \; \text{Im} \; \Gamma_1 + \varphi \; (1 + \lambda_2^2) \; \text{Im} \; \Gamma_2\}. \tag{3.15}$$

where μ is the shear modulus. Assuming that a square-root singularity exists at the crack tip as in the static situation, series stress functions similar to the static form, eq (2.19), can be considered. For the dynamic problem then,

$$\Gamma_k(z_k) = Z_k(z_k) = \sum_{j=0}^{\infty} A_j \; z_k^{j-1/2} \; ; \; k = 1, \; 2. \tag{3.16}$$

For this choice of stress functions, the crack faces are

traction-free. To satisfy the condition of $\sigma_{xy} = 0$ on $y = 0$, the constants ρ and φ must be related as

$$\varphi = \frac{2\,\lambda_1}{(1 + \lambda_2^2)}\,\rho. \tag{3.17}$$

In this derivation we assume that the A_j appearing in the Γ_1 series are the same as the A_j appearing in the Γ_2 series. The leading coefficient, A_0, is again related to the opening-mode stress intensity factor by

$$K_I = A_0\,\sqrt{2\pi}\ . \tag{3.18}$$

The existence of a square-root singularity is well documented for the problem being considered here [3.12,3.13,3.15]. This is distinctly different from the other types of dynamic problems mentioned previously. Both Freund [3.17] and Rosakis [3.18] found that a square-root singular field does not develop under time-dependent loading conditions for some time after the crack tip is loaded. This remains an open question for the analysis of stress wave-loaded fracture events.

A second choice of stress functions to be used in eqs (3.13)-(3.15) can be made again in direct parallel to the static Y(z) series as

$$\Gamma_k(z_k) = Y_k(z_k) = \sum B_m\, z_k^m \quad ;\ k = 1,\ 2. \tag{3.19}$$

The leading term of the above stress function is a constant, as in the static case. This choice for the stress function satisfies the condition of $\sigma_{xy} = 0$ on $y = 0$. To satisfy the boundary condition of traction-free crack surfaces the constants ρ and φ must be related as

$$\varphi = \frac{1 + \lambda_2^2}{2\,\lambda_2}\,\rho. \tag{3.20}$$

The constant, ρ, can be specified through the definition of K_I after superposing the stress functions in eqs 3.14 and 3.17. The

result is

$$\rho = \frac{1 + \lambda_2^2}{4\lambda_1\lambda_2 - (1 + \lambda_2^2)^2} . \tag{3.21}$$

Substituting eqs (3.16)-(3.21) into eqs (3.13)-(3.15) we arrive at the following general expressions for the dynamic stress field:

$$\sigma_{xx} = \beta_1 \{\beta_2 \text{ Re } Z_1 - \beta_3 \text{ Re } Z_2 + \beta_2 \text{ Re } Y_1 - \beta_4 \text{ Re } Y_2\}, \tag{3.22}$$

$$\sigma_{yy} = \beta_1 \{-\beta_4 \text{ Re } Z_1 + \beta_3 \text{ Re } Z_2 - \beta_4 \text{ Re } Y_1 + \beta_4 \text{ Re } Y_2\}, \tag{3.23}$$

$$\sigma_{xy} = 2\lambda_1\beta_1 \{-\text{Im } Z_1 + \text{Im } Z_2 - \text{Im } Y_1 + \beta_5 \text{ Im } Y_2\}, \tag{3.24}$$

where the velocity-dependent functions β_j, $j = 1, \ldots, 5$, have been introduced for brevity. The values of the β_j are

$$\beta_1 = \frac{1 + \lambda_2^2}{4\lambda_1\lambda_2 - (1 + \lambda_2^2)^2} , \tag{3.25}$$

$$\beta_2 = 1 + 2\lambda_1^2 - \lambda_2^2 , \tag{3.26}$$

$$\beta_3 = \frac{4\lambda_1\lambda_2}{1 + \lambda_2^2} , \tag{3.27}$$

$$\beta_4 = 1 + \lambda_2^2 , \tag{3.28}$$

$$\beta_5 = \frac{(1 + \lambda_2)^2}{4\lambda_1\lambda_2} . \tag{3.29}$$

Substituting eqs (3.22)-(3.24) into Hooke's law provides expressions for the Cartesian strain components,

$$\varepsilon_{xx} = \frac{\beta_1}{E} \{(\beta_2 + \nu\beta_4)\text{Re } Z_1 - \beta_3(1 + \nu)\text{Re } Z_2 + (\beta_2 + \nu\beta_4)\text{Re } Y_1$$

$$-\beta_4(1 + \nu)\text{Re } Y_2\}, \tag{3.30}$$

$$\varepsilon_{yy} = \frac{\beta_1}{E} \{-(\beta_4 + \nu\beta_2)\text{Re } Z_1 + \beta_3(1 + \nu)\text{Re } Z_2 - (\beta_4 + \nu\beta_2)\text{Re } Y_1$$

$$+\beta_4(1 + \nu)\text{Re } Y_2\}, \tag{3.31}$$

$$\gamma_{xy} = \frac{2\lambda_1\beta_1}{\mu} \{-\text{Im } Z_1 + \text{Im } Z_2 - \text{Im } Y_1 + \beta_5 \text{ Im } Y_2\}. \tag{3.32}$$

An approach similar to that taken in previous studies [3.19-3.24] will be used to determine the orientation of the strain gage relative to the crack propagation path. However, the influence of the $r^{1/2}$ term, which was neglected in [3.24], is shown to be of paramount importance in this study.

Consider a rotated coordinate system (x',y') as shown in figure 3.2. The strains in the rotated coordinate system are obtained by combining eqs (3.30)-(3.32), the first strain invariant and the strain transformation equation,

$$(\varepsilon_{y'y'} - \varepsilon_{x'x'}) + i\gamma_{x'y'} = e^{2i\alpha}(\varepsilon_{yy} - \varepsilon_{xx} + i\gamma_{xy}), \tag{3.33}$$

where α is the angle of rotation. Using eqs (3.30)-(3.33) the strain field in the rotated coordinate system is

$$2\mu\varepsilon_{x'x'} = \beta_1\{[k(\lambda_1^2-\lambda_2^2) + (1+\lambda_1^2)\cos2\alpha]\text{ Re } Z_1 - \beta_3\cos2\alpha\text{ Re } Z_2$$

$$+[k(\lambda_1^2-\lambda_2^2) + (1+\lambda_1^2)\cos2\alpha]\text{ Re } Y_1 - \beta_4\cos2\alpha\text{ Re } Y_2$$

$$+2\lambda_1\sin2\alpha\ [\ -\text{Im } Z_1 + \text{Im } Z_2 - \text{Im } Y_1 + \beta_5 \text{ Im } Y_2\ ]\}, \tag{3.34}$$

$$2\mu\varepsilon_{y'y'} = \beta_1\{[k(\lambda_1^2-\lambda_2^2) - (1+\lambda_1^2)\cos2\alpha]\ \mathrm{Re}\ Z_1 + \beta_3\cos2\alpha\ \mathrm{Re}\ Z_2$$
$$+[k(\lambda_1^2-\lambda_2^2) - (1+\lambda_1^2)\cos2\alpha]\ \mathrm{Re}\ Y_1 + \beta_4\cos2\alpha\ \mathrm{Re}\ Y_2$$
$$+2\lambda_1\sin2\alpha\ [\ \mathrm{Im}\ Z_1 - \mathrm{Im}\ Z_2 + \mathrm{Im}\ Y_1 - \beta_5\ \mathrm{Im}\ Y_2\ ]\},\qquad (3.35)$$

$$\mu\gamma_{x'y'} = \beta_1\ [-(1+\lambda_1^2)\ \mathrm{Re}\ Z_1 + \beta_3\mathrm{Re}\ Z_2 - (1+\lambda_1^2)\ \mathrm{Re}\ Y_1$$
$$+ \beta_4\mathrm{Re}\ Y_2]\ \sin2\alpha + 2\lambda_1\beta_1[\ -\mathrm{Im}\ Z_1 + \mathrm{Im}\ Z_2 - \mathrm{Im}\ Y_1$$
$$+ \beta_5\ Y_2\ ]\ \cos2\alpha,\qquad (3.36)$$

where $k = (1-\nu)/(1+\nu)$.

3.1.1 SINGLE-ELEMENT STRAIN GAGE

The strain, ε_g, on a single-element gage aligned with the x'-axis is given by eq (3.34). Using the results obtained in Chapter 4 of this report allows suitable locations for the gages to be specified where a three-term series expansion is valid. The dynamic strain field described by a three-parameter model along the gage axis is

$$2\mu\varepsilon_g = A_0\ f_0 + A_1\ f_1 + B_0\ g_0\ ,\qquad (3.37)$$

where

$$f_0 = r_1^{-1/2}\ \beta_1\{\cos(\theta_1/2)[k(\lambda_1^2-\lambda_2^2)+(1+\lambda_1^2)\cos2\alpha]+2\lambda_1\sin(\theta_1/2)\sin2\alpha\}$$
$$+\ r_2^{-1/2}\ \beta_1\{-\ \beta_3\ \cos(\theta_2/2)\cos2\alpha-2\lambda_1\sin(\theta_2/2)\sin2\alpha\},\qquad (3.38)$$

$$f_1 = r_1^{1/2}\ \beta_1\{\cos(\theta_1/2)[k(\lambda_1^2-\lambda_2^2)+(1+\lambda_1^2)\cos2\alpha]\ -\ 2\lambda_1\sin(\theta_1/2)\sin2\alpha\}$$
$$+\ r_2^{1/2}\ \beta_1\{-\ \beta_3\ \cos(\theta_2/2)\cos2\alpha+2\lambda_1\sin(\theta_2/2)\sin2\alpha\},\qquad (3.39)$$

$$g_0 = \beta_1(k+\cos 2\alpha)\ (\lambda_1^2-\lambda_2^2)\ . \qquad (3.40)$$

The coefficient of the B_0 term in eq (3.37) can be eliminated by selecting the orientation angle, α, such that

$$\cos 2\alpha = -k. \qquad (3.41)$$

Then eq (3.37) becomes:

$$2\mu\varepsilon_g = A_0 f_0 + A_1 f_1. \qquad (3.42)$$

Values of α for various Poisson's ratios are given in [3.20]. For the steel used in this investigation, $\nu = 0.30$ and $\alpha = 61.3^\circ$or $\alpha = 118.7^\circ$ to satisfy eq (3.41). It is important at this point to examine which of the two choices for α gives strain data more suitable for the accurate determination of $K_{ID}(t)$ using single-element strain gages.

The first issue to address in this selection of α is the features observed in the ε-t trace that are the most useful for determining either the crack position or velocity. To examine the strain-time trace it is convenient to rewrite eq (3.42) in a modified form as

$$2\mu\varepsilon_g/A_0 = f_0 + (A_1/A_0)\ f_1. \qquad (3.43)$$

For specified values of crack velocity, position of the gage line and the ratio A_1/A_0, the modified strain defined by eq (3.43) can be determined as a function of crack tip position, time or the angle θ. For the choice of $\alpha = 118.7^\circ$, as used in [3.24], the modified gage response is shown in figure 3.3. These results show that the maximum value of $2\mu\varepsilon_g/A_0$ is critically dependent (± 30%) on the magnitude of A_1/A_0. This indicates that an analysis with $\alpha = 118.7^\circ$ and A_1/A_0 taken as zero gives unacceptably large errors in any A_0 or K_{ID} determination. Furthermore, the peak in $2\mu\varepsilon_g/A_0$ will occur at the position of the gage (x = 0) if and only if $A_1/A_0 = 0$. For nonzero values of A_1/A_0, which are common, the peak value of $2\mu\varepsilon_g/A_0$ does not occur until the crack tip has

passed beyond the gage. In general, the peak value of $2\mu\varepsilon_g/A_0$ does not locate the position of the crack tip. Finally, a zero crossing does not occur as the gage is unloaded by the passage of the crack.

Selecting the alternative choice of $\alpha = 61.3^\circ$ results in an improved strain response that is presented in figure 3.4. The peak modified strain varies only ±3% with large changes in A_1/A_0. In an engineering approach to the analysis, this error is negligible and the effect of A_1 could be ignored in determining A_0. Such a procedure, however, would not locate the crack tip which is needed for a full dynamic fracture characterization of the material. A more refined analysis would therefore determine stress intensity and crack tip position by making use of the large amount of data available in addition to the peak values. Towards the development of such a procedure, note in figure 3.4 that a zero crossing occurs after the crack tip has passed the gage. The time of the zero crossing is dependent on A_1/A_0. This characteristic is exploited in Section 3.2 to locate the crack tip both spatially and temporally.

3.1.2 STRAIN GAGE ROSETTE

As previously mentioned in Section 2.1.2, it may be desired to have temperature compensation for some material testing applications. Again we consider the response of a strain gage rosette with its individual sensors connected to adjacent arms of a Wheatstone bridge. The bridge output is then equivalent to the difference in strain, $\varepsilon_{y'y'}-\varepsilon_{x'x'}$:

$$\mu(\varepsilon_{y'y'}-\varepsilon_{x'x'}) = = \beta_1 [-(1+\lambda_1^2)\ \mathrm{Re}\ Z_1 + \beta_3 \mathrm{Re}\ Z_2 - (1+\lambda_1^2)\ \mathrm{Re}\ Y_1 + \beta_4 \mathrm{Re}\ Y_2] \cos 2\alpha + 2\lambda_1\beta_1[- \mathrm{Im}\ Z_1 + \mathrm{Im}\ Z_2 - \mathrm{Im}\ Y_1 + \beta_5\ Y_2\ ] \sin 2\alpha. \qquad (3.44)$$

The gage response with a three-parameter model is

$$2\mu\varepsilon_g = A_0 f_0 + A_1 f_1 + B_0 g_0, \tag{3.45}$$

where

$$f_0 = 2r_1^{-1/2}\beta_1\{-(1+\lambda_1^2)\cos(\theta_1/2)\cos2\alpha - 2\lambda_1\sin(\theta_1/2)\sin2\alpha\}$$
$$+2r_2^{-1/2}\beta_1\{-\beta_3\cos(\theta_2/2)\cos2\alpha + 2\lambda_1\sin(\theta_2/2)\sin2\alpha\}, \tag{3.46}$$

$$f_1 = 2r_1^{1/2}\beta_1\{-(1+\lambda_1^2)\cos(\theta_1/2)\cos2\alpha + 2\lambda_1\sin(\theta_1/2)\sin2\alpha\}$$
$$+2r_2^{1/2}\beta_1\{\beta_3\cos(\theta_2/2)\cos2\alpha - 2\lambda_1\sin(\theta_2/2)\sin2\alpha\}, \tag{3.47}$$

$$g_0 = -2\beta_1(\lambda_1^2-\lambda_2^2)\cos2\alpha. \tag{3.48}$$

A factor of two has been introduced on both sides of eq (3.45) to allow direct comparison with the single-element gage response of eq (3.42) The coefficient of the B_0 term in eq (3.45) can be eliminated by selecting the orientation angle, α, so that

$$\cos2\alpha = 0. \tag{3.49}$$

Then eq (3.45) becomes:

$$2\mu\varepsilon_g = A_0 f_0 + A_1 f_1. \tag{3.50}$$

Unlike the analysis for the single-element gage, the orientation angle, α, specified by eq (3.49) is material independent; $\alpha = \pm 45^\circ$ to eliminate the B_0 contribution to the gage response for any given elastic material. It is helpful to examine a strain-time trace predicted by eq (3.50) by writing the equation in modified form as

$$2\mu\varepsilon_g/A_0 = f_0 + (A_1/A_0) f_1. \tag{3.51}$$

For specified values of crack velocity, position of the gage line, and the ratio A_1/A_0, the modified strain defined by eq (3.51) can be determined as a function of crack tip position, time, or the angle θ. For $\alpha = 45^\circ$, the predicted gage response is shown in

figure 3.5 for a variety of values for A_1/A_0. The gage height was 10.2 mm and the ratio of crack speed to Rayleigh wave speed was $c/c_R = 0.22$ for this plot.

Several features of the rosette response are evident when comparing the response shown in figure 3.5 with the response of the single-element gage shown in figure 3.4. First, the positive peak-to-negative peak amplitude is much larger for the rosette than for the single-element gage. This is potentially useful in the development of feature-extraction procedures similar to [3.19] and [3.22]. Second, the position of the peak in the modified strain for the rosette is insensitive to the value of A_1/A_0. However, the magnitude of the peak is sensitive to A_1/A_0.

3.2 TRIANGULATION AND ITERATION ALGORITHM

As discussed above, the zero crossing in strain shown in figures 3.4 and 3.5 can be used to locate the crack tip in both space and time. Before developing such a procedure, it is necessary to comment on the conditions under which a zero crossing will exist. Specifically, as the height of the gage above the crack path increases, the zero crossing eventually does not occur. This can be seen in the predicted rosette responses shown in figure 3.6 for increasing y_g-values. Results for the maximum possible y_g as a function of the A_1/A_0 ratio are presented in figure 3.7 for the single-element gage and in figure 3.8 for the rosette.

Consider two single-element gages, *a* and *b*, each located along a gage line located y_g above the crack propagation line with α selected to satisfy eq (3.41), as shown in figure 3.9. The crack is propagating in the positive x-direction with a velocity c, which is considered constant between adjacent gage pairs. This velocity can be determined from the spatial separation of the gages, s_{ab}, and the time between peaks or zero crossings observed

on the ε-t traces. The values of A_0 and A_1 are also considered to be constant between adjacent gage pairs. This is essentially a discretization of the variation of A_0 and A_1 with crack length, where the discretization interval is defined by the gage spacing.

The first step in the analysis is to locate the position of the crack tip on the crack line with respect to the gage pair. As previously discussed, the proper selection of the orientation angle, α, and gage height, y_g, results in a clearly defined zero crossing that can be used to locate the crack tip. Referring to figure 3.9, consider the zero crossing of gage *a* to occur at time t = 0 in the coordinate system (x,y,t) translating with the crack tip. The time at which this event occurs is easily extracted from the experimental data. Writing eq (3.43) for gage *a* at the zero crossing gives

$$w(\theta) = f_0 + (A_1/A_0)\, f_1 = 0, \tag{3.52}$$

where the f_i are defined in eqs (3.38) and (3.39) and $r = y_g/\sin\theta$. For specified values of A_1/A_0, y_g and c, eq (3.52) can be solved for the angle $(\theta_0)_a$ locating the crack tip with respect to gage *a* when the gage is sensing zero strain. Note that y_g and c are known *a priori* but the value of A_1/A_0 must be assumed. Since eq (3.52) is nonlinear in θ, the solution uses the Newton-Raphson iterative procedure; that is,

$$\theta_{n+1} = \theta_n - \frac{w(\theta_n)}{\partial w/\partial \theta_n}. \tag{3.53}$$

The convergence is rapid with θ obtained in one to five iterations. No problems were encountered with the multiple-valued trigonometric functions (f_i) or their derivatives, since all of the branch cuts were taken into account. The angle $(\theta_0)_a$ which locates the crack tip relative to gage *a* at the time associated

with the zero crossing condition is dependent on the crack velocity, gage height y_g, and the ratio A_1/A_0. Results showing θ_0 as functions of these variables are presented in figures 3.10 to 3.12.

For prescribed values of c, y_g, and an assumed value of A_1/A_0 the angle $(\theta_0)_a$ relative to gage *a* is now known. Next, the spatial positions of both gages *a* and *b* may be calculated, figure 3.13, from the relations

$$x_a = y_g/\tan (\theta_0)_a , \tag{3.54}$$

$$x_b = s_{ab} + x_a , \tag{3.55}$$

$$(\theta_0)_b = \tan^{-1}(y_g/[s_{ab} + x_a]) , \tag{3.56}$$

where x_a and x_b are the x-coordinates of gages *a* and *b* relative to the origin of the (x,y,t) system and (x,y,0) is taken at the time of the zero crossing of gage *a* on the ε-t trace.

A test is now made to check the value of A_1/A_0 used in the solution of eq (3.52) and to refine the estimation if necessary. In the verification procedure, use is made of the assumption that the ratio A_1/A_0 is constant as the crack propagates between the gages. Advantage may then be taken of the wealth of data available from the experimental ε-t traces. The most direct approach is to shift back from the time of the zero crossing by an increment Δt and calculate the ratio $(\varepsilon_a/\varepsilon_b)_{-\Delta t}$ using the estimated value of A_1/A_0. This strain ratio is compared to the experimentally recorded ratio at the time Δt. If the difference, ξ, is within some acceptable error bound, $\bar{\xi}$, then the current value of A_1/A_0 is acceptable. If the difference exceeds $\bar{\xi}$ then the estimate for A_1/A_0 must be revised by some amount δ and the entire procedure, starting with the $(\theta_0)_a$ calculation, is repeated

until $\xi \leq \bar{\xi}$ and an accurate estimate of A_1/A_0 is established. As a final check on the estimate of A_1/A_0 the individual strain components are recalculated and compared to the experimental values. This simple check is necessary, since the ratio of the strains is being compared and not their absolute values.

At this point the precise position of the crack tip at (x,y,0) is known as well as the ratio A_1/A_0. The dynamic stress intensity factor, K_{ID}, may then be calculated from the strain sensed by gage *b*, ε_b, at the time t = 0 when gage *a* is sensing zero strain:

$$K_{ID} = \frac{2\mu(\varepsilon_b)\sqrt{2\pi}}{(f_0)_b + (A_1/A_0)\,(f_1)_b}, \qquad (3.57)$$

where the $(f_i)_b$ are evaluated using $(\theta_0)_b$ as defined in figure 3.13. The entire iterative procedure is illustrated in the flowchart shown in figure 3.14.

3.3 SPATIALLY OVERDETERMINED ANALYSIS

Instead of using the temporal variation in strain at a particular material point, as was done in the preceding section, consideration is now given to analyzing the spatial variation in strains recorded by a series of strain gages at one particular point in time. By analyzing the strains over a sequence of time steps for crack length, a, and stress intensity, K_{ID}, complete histories for a(t) and $K_{ID}(t)$ may be formed. The method is essentially the dynamic parallel to the overdetermined static analysis described earlier. However, the situation is made more complicated due to the unknown crack-tip position and the resulting nonlinearities in the system of equations.

The analysis applies either eq (3.42) or eq (3.50) to J (J > 3) different strain-time traces which are showing changes in strain due to the dynamic crack growth at a prescribed time, $t = t_1$. In general, there are three independent unknowns in eq (3.40) or eq (3.50): A_0, A_1, and the crack tip position. The series coefficients, A_0 and A_1, will be the same for each individual strain-time trace; but the angle, θ, locating the position, P, relative to the crack tip is different for each gage. In order to make the analysis tractable it is useful to relate all of the angles, θ, to the angle the crack tip makes with the first gage, $\theta^{(1)}$, by using the spatial separations of the gages, s_{ij} :

$$\theta^{(j)} = \tan^{-1}\left(\frac{y_g}{x_1 + s_{1j}} \right) \quad ; \; j = 2,3,\ldots, J \qquad (3.58)$$

where y_g, x_1 and s_{ij} are defined in figure 3.15.

Using either eq (3.42) or eq (3.50) and eq (3.58) for J strain gages at time $t = t_1$, we develop the following system of equations,

$$\begin{bmatrix} 2\mu(\varepsilon_g)_1 \\ 2\mu(\varepsilon_g)_2 \\ 2\mu(\varepsilon_g)_3 \\ \vdots \\ 2\mu(\varepsilon_g)_J \end{bmatrix} = \begin{bmatrix} A_0(f_0)_1 + A_1(f_1)_1 \\ A_0(f_0)_2 + A_1(f_1)_2 \\ A_0(f_0)_3 + A_1(f_1)_3 \\ \vdots \\ A_0(f_0)_J + A_1(f_1)_J \end{bmatrix} \qquad (3.59)$$

The overdetermined system given by eq (3.59) is linear in the unknown coefficients A_0 and A_1 but nonlinear in the angle $\theta^{(1)}$ locating the crack tip with respect to the first gage. The

overdetermined system can be solved by a variety of nonlinear least squares methodologies. Since the number of unknowns is small, the Newton-Raphson iterative procedure is used here. The details of the solution procedure are presented in Appendix B.

Because an iterative technique is needed to solve the nonlinear least squares problem, a criterion must be specified for defining convergence. The criterion used here is based on a normalized residual defined as

$$\bar{r} = \left[\sum_{j=1}^{J} (\varepsilon_j^e - \varepsilon_j^c)^2 \right]^{1/2} / \left[J \sum_{j=1}^{J} \varepsilon_j^e \right], \qquad (3.60)$$

where

ε_j^e = experimentally recorded strain at gage j,

ε_j^c = calculated strain at gage j,

J = total number of gages.

The iterative solution procedure is repeated until the value of the normalized residual, $\bar{r}$, is less than 0.5%.

After solving eq (3.59) at $t = t_1$, the system of equations is formed for the next temporal data point taken at $t = t_2$. Proceeding in this way gives $A_0(t)$, $A_1(t)$, and $\theta^{(1)}(t)$ over the entire time history. However, care must be taken to avoid extending the region of data analysis to points P, where the three-parameter representation given by eqs (3.42) and (3.50) do not describe the strain field with sufficient accuracy. This issue is addressed in Chapter 4.

This particular method of analysis appears most attractive for applications to nonconstant crack velocity problems, since no assumptions are required concerning the behavior of the crack velocity or coefficient value between gages. However, the amount of data available to introduce redundancy into the analysis is limited to those gages close enough to the crack tip where a

three-parameter model is adequate.

3.4 EXPERIMENTAL VERIFICATION

An experiment was performed to demonstrate the methods described here. The sample used for the fracture experiment was a compact tension specimen fabricated from 12.7 mm thick 4340 alloy steel, as illustrated in figure 3.16. The alloy was heat treated to a hardness of $R_c = 51$, obtained with a straight quench in oil. The simulated crack was saw-cut into the specimen, and a blunted chevron notch was used to control the load required for initiation. Shallow side grooves on each side equal to 5% of the specimen thickness were used to control the crack line.

To account for the presence of side grooves a correction factor, C_g, was applied to the calculated K_{ID} values. The correction factor is defined by

$$C_g = (B/B_n)^{1/2} , \tag{3.61}$$

where B is the gross specimen thickness and B_n is the reduced thickness through the side-grooved region. For the specimen used in this experiment, $B = 12.7$ mm, $B_n = 11.6$ mm, and $C_g = 1.048$. This correction factor is very small; however, for the sake of completeness, it will be applied to all calculated values of stress intensity.

The specimen was instrumented with 6 single-element strain gages, each with an active grid length of 3.18 mm. Following the argument presented in [3.20] errors due to strain gradient over the gage length were negligible. The gages were oriented at $\alpha = 61.3^\circ$ and were placed along a gage line with $y_g = 10.4$ mm on 12.7 mm centers. The gages were connected to high-performance bridge and amplifier units with a frequency response from DC to 120 kHz. The strain gages were calibrated using shunt calibration values

obtained immediately prior to the experiment. Digital oscilloscopes were then used to record the output signals using a sampling rate of 200 ns per point. A closed-loop, servo-hydraulic test system was used to load the specimen. Voltage-time traces were downloaded from the oscilloscope bubble memories onto a personal computer. A commercial spreadsheet program was then used to postprocess the data. The resulting ε-t traces for the 6 gages referred to a common time base are shown in figure 3.17. Excellent agreement was obtained between the experimental traces and the predicted behavior shown in figure 3.4. Figure 3.17 shows that the predicted zero crossing is well defined, as required for the triangulation analysis. Also, the peak amplitude for gage 1 is larger than the peak amplitudes of the other 5 gages. We think that the crack velocity was higher upon initiation and that the velocity was decreasing as the crack approached the first gage. Additionally, the stress intensity sensed by the first gage was higher as the transition from the initiation stress intensity to the running stress intensity occurred.

Before performing the dynamic analysis, the stress intensity factor at initiation, K_{Iq}, was determined. Following [3.20], the strain sensed by a gage at a distance r_g from the crack tip is related to the stress intensity factor by

$$K_I = C_g \frac{2\mu\sqrt{2\pi r_g}}{f_0^s} \varepsilon_g^s , \qquad (3.62)$$

where ε_g^s = static strain level at initiation,

$$f_0^s = k\cos(\theta/2) - (1/2)\sin(\theta)\sin(3\theta/2)\cos(2\alpha) + (1/2)\sin(\theta)\cos(3\theta/2)\sin(2\alpha),$$

$$\alpha = 61.3^\circ,$$

r_g = distance from the crack tip to the strain gage,

C_g = side groove correction factor.

For gage 1 the static strain was 1.661×10^{-3} prior to crack initiation. Gage 1 is located at $\theta = 22.2^\circ$ and $r_g = 27.4$ mm from the static crack tip; therefore, from eq (3.62) $K_{Iq} = 160.6$ MPa $\sqrt{m}$.

Adjacent gage pairs were analyzed following the triangulation and iteration procedure using an error bound $\bar{\xi} = 0.001$ and an iteration increment on A_1/A_0 of $\delta = 0.492\ m^{-1}$. A_1/A_0 was initially assumed to be zero to start the algorithm. Convergence to the correct value of A_1/A_0 was sensitive to the time interval, Δt, used in the strain ratio test. The most consistent results were obtained when the time interval, Δt, was in the range $-20\ \mu s < \Delta t < -30\ \mu s$. This result follows from figure 3.17, because for times less than $-20\ \mu s$ before the zero crossing the strain is changing rapidly and any small error in time resolution leads to large errors in strain. Additionally, as figure 3.17 shows, the strain response in the region of $t < -20\ \mu s$ ($x < 13$ mm for $c = 650$ m/s) is not sensitive to the value of A_1/A_0. Therefore, in this experiment, times of less than $-20\ \mu s$ are inherently prone to error. For times greater than $-30\ \mu s$ the gage is nearing the limit where a three-parameter model fails to adequately describe the strain field.

Detailed results obtained from the data from gages 2 and 3 at five different times over the interval between $-20\ \mu s$ and $-30\ \mu s$ relative to the zero crossing as the crack propagated between the two gage stations are presented in table 3.1. The value of A_1/A_0 varies slightly with the time; however, $K_{ID}(t)$ remains essentially constant. As a final test, the strain at the two gages is calculated at each time step using the values of K_{ID}, A_1/A_0, and crack length established from the analysis. Close agreement between the measured and computed strains (-5.0% to

-7.3%) at both gages is noted as shown in table 3.1.

Results for K_{ID} and A_1/A_0 from the data for all five gage pairs are given in table 3.2. All of the results shown represent mean values taken over five time steps -20 μs < Δt < -30 μs. Standard deviations and coefficients of variation are given for K_{ID} and A_1/A_0. The time-averaged results indicate little variation in K_{ID} or A_1/A_0 with respect to the mean values. As noted in the discussion of table 3.1, the calculated values of K_{ID} exhibit the least amount of variance over the analysis interval.

The two assumptions made in the analysis, namely constant crack tip velocity and constant A_1/A_0 between adjacent gage pairs, are examined in light of the results given in table 3.2. Consider first the assumption made of constant crack speed. Using the calculated value θ_0 with the known time of the zero crossing and the spatial separation of the gages, a graph can be constructed of crack tip position versus time. As shown in figure 3.18, the slope of this curve is constant, which verifies the constant velocity assumption (c = 640 m/s).

For determining the effect of velocity on the determination of $K_{ID}(t)$, a parallel analysis was conducted using the first three terms of the static expressions given by eq (2.20) to represent the strain field. The same analysis procedures and the restrictions on the time steps as in the dynamic case were used to obtain the results presented in table 3.3. For the crack velocity c/c_R = 0.22 for this experiment, the difference between the static and dynamic results are negligible.

The assumption regarding constant A_1/A_0 between adjacent gage pairs must be addressed in two parts, since, in general, the ratio depends on velocity and crack length. The discussion above has verified the adequacy of a constant velocity assumption for the particular experiment which was analyzed. Therefore, it is justifiable to assume that the velocity-dependent portion of the A_1/A_0 ratio does not change since the velocity is not changing.

In regard to the variance with crack length of A_1/A_0, it is useful to recall that the assumption of constant A_1/A_0 is made only over discrete intervals which are defined by the gage spacings. For the particular experiment analyzed the gage spacing was 12.7 mm. This corresponds to an assumption of constant A_1/A_0 over an increment of crack growth $a/W = 0.05$. The effect of such a discretization interval for the smoothly varying behaviors of A_0 and A_1 with crack length is limited.

A second analysis was performed using the spatially overdetermined approach of Section 3.3. Results were obtained which are consistent with the results of the triangulation-iteration algorithm. Plots of $K_{ID}(t)$ and $a(t)$ from the overdetermined analysis are presented in figures 3.19 and 3.20.

REFERENCES

[3.1] Sanford, R. J., "Application of Least Squares to Photoelastic Analysis," **Experimental Mechanics**, Vol. 20, pp. 192-197 (1980).

[3.2] Thau, S. A. and Lu, T.-H., "Transient Stress Intensity Factors for a Finite Crack in an Elastic Solid Caused by a Dilatational Wave," **International Journal of Solids and Structures**, Vol. 7, pp. 731-750 (1971).

[3.3] Achenbach, J. D., "Extension of a Crack by a Shear Wave," **Journal of Applied Mathematics and Physics (ZAMP)**, Vol. 21, pp. 887-900 (1970).

[3.4] Jahanshahi, A., "A Diffraction Problem and Crack Propagation," **Journal of Applied Mechanics**, Vol. 34, pp. 100-103 (1967).

[3.5] Achenbach, J. D. and Nuismer, R., "Fracture Generated by a Dilatational Wave," **International Journal of Fracture Mechanics**, Vol. 7, No. 1, pp. 77-87 (1971).

[3.6] Freund, L. B., "Crack Propagation in an Elastic Solid Subjected to General Loading - III. Stress Wave Loading," **Journal of the Mechanics and Physics of Solids**, Vol. 21, pp. 47-61 (1973).

[3.7] Freund, L. B., "Crack Propagation in an Elastic Solid Subjected to General Loading - IV. Obliquely Incident Stress Pulse," **Journal of the Mechanics and Physics of Solids**, Vol. 22, pp. 137-146 (1974).

[3.8] Baker, B. R., "Dynamic Stresses Created by a Moving Crack," **Journal of Applied Mechanics**, Vol. 29, pp. 449-458 (1962).

[3.9] Homma, H., Ushiro, T., and Nazakawa, H., "Dynamic Crack Growth Under Stress Wave Loading," **Journal of the Mechanics and Physics of Solids**, Vol. 27, pp. 151-162 (1979).

[3.10] Freund, L. B., "Crack Propagation in an Elastic Solid Subjected to General Loading - I. Constant Rate of Extension," **Journal of the Mechanics and Physics of Solids**, Vol. 20, pp. 129-140 (1972).

[3.11] Freund, L. B., "Crack Propagation in an Elastic Solid Subjected to General Loading - II. Non-Uniform Rate of Extension," **Journal of the Mechanics and Physics of Solids**, Vol. 20, pp. 141-152 (1972).

[3.12] Radok, J. R. M., "On the Solution of Problems of Dynamic Plane Elasticity," **Quarterly of Applied Mathematics**, Vol. 14, pp. 289-298 (1956).

[3.13] Nishioka, T. and Atluri, S. N., "Path-Independent Integrals, Energy Release Rates, and General Solutions of Near-Tip Fields in Mixed-Mode Fracture Mechanics," **Engineering Fracture Mechanics**, Vol. 18, No. 1, pp. 1-22 (1983).

[3.14] Irwin, G. R., "Constant Speed Semi-Infinite Tensile Crack Opened by a Line Force, P, at a Distance, b, from the Leading Edge," **Lehigh University Lecture Notes on Fracture Mechanics** (1968).

[3.15] Nilsson, F., "Dynamic Stress-Intensity Factors for Finite Strip Problems," **International Journal of Fracture Mechanics**, Vol. 8, No. 4, pp. 403-411 (1972).

[3.16] Knauss, W. G. and Ravi-Chandar, K., "Fundamental Considerations in Dynamic Fracture," **Engineering Fracture Mechanics**, Vol. 23, No. 1, pp. 9-20 (1986).

[3.17] Freund, L. B., "Some Theoretical Results on the Dependence of Dynamic Stress Intensity Factor on Crack Speed," **Workshop on Dynamic Fracture**, Knauss, W. G., Ravi-Chandar, K. and Rosakis, A., Eds., California Institute of Technology, pp. 129-136 (1983).

[3.18] Krishnaswamy, S., and Rosakis, A. J., **On the Extent of Dominance of Asymptotic Elasto-Dynamic Crack-Tip Fields; Part 1: An Experimental Study Using Bifocal Caustics**, Graduate Aeronautical Laboratory Report SM 88-21, California Institute of Technology (1988).

[3.19] Dally, J. W. and Sanford, R. J., "On Measuring the Instantaneous Stress Intensity Factor for Propagating Cracks," **Proceedings, International Conference on Fracture Mechanics VII**, Houston TX, (1989).

[3.20] Dally, J.W. and Sanford, R. J., "Strain-Gage Methods for Measuring the Opening-Mode Stress Intensity Factor, K_I," **Experimental Mechanics**, Vol. 27, No. 4, pp. 381 - 388 (1987).

[3.21] Berger, J. R. and Dally, J. W., "An Overdeterministic Approach for Measuring K_I Using Strain Gages," **Experimental Mechanics**, Vol. 28, No. 2, pp. 142-145 (1988).

[3.22] Dally, J. W., Sanford, R. J., and Berger, J. R., "An Improved Strain Gage Method for Measuring $K_I(t)$ for a Propagating Crack," **Journal of Strain Analysis for Engineering Design** (In Press).

[3.23] Berger, J. R., Dally, J. W., and Sanford, R. J., "Determining the Dynamic Stress Intensity Factor with Strain Gages Using a Crack Tip Locating Algorithm", **Engineering Fracture Mechanics** (In Press).

[3.24] Shukla, A., Agarwal, R. K., and Nigam, H., "Dynamic Fracture Studies on 7075-T6 Aluminum and 4340 Steel Using Strain Gages and Photoelastic Coatings," **Engineering Fracture Mechanics** Vol. 31, No. 3, pp. 501-515 (1989).

Table 3.1

Results from a dynamic analysis of data from gages 2 and 3.

	Experimental				Computed	
Δt	$(\varepsilon_g)_2$	$(\varepsilon_g)_3$	K_{ID}	A_1/A_0	$(\varepsilon_g)_2$	$(\varepsilon_g)_3$
μs	$\mu m/m$	$\mu m/m$	MPa $\sqrt{m}$	m^{-1}	$\mu m/m$	$\mu m/m$
-20	2039	1171	123.9	-28.5	1926	1104
-22	1998	1087	123.9	-29.1	1883	1023
-24	1956	1045	123.8	-27.6	1817	969
-26	1872	962	123.8	-28.1	1734	895
-28	1747	920	123.5	-25.1	1654	874

Table 3.2

Average results from a dynamic analysis of data for all adjacent gage pairs.

Gage Pair	$\overline{K_{ID}}$	$\frac{S_{(K)}}{\overline{K_{ID}}}$	$\overline{A_1/A_0}$	$\frac{S_{(A1/A0)}}{\overline{A1/A0}}$
	MPa√m	%	m^{-1}	%
1 - 2	131.4	0.27	-26.2	-10.4
2 - 3	123.8	0.15	-27.7	-5.6
3 - 4	122.4	0.33	-27.5	-11.7
4 - 5	120.1	0.19	-27.5	-5.7
5 - 6	120.9	0.20	-30.9	-6.9

Table 3.3

Average results from a static analysis of data for all adjacent gage pairs.

Gage Pair	$\overline{K_{ID}}$	$\frac{S_{(K)}}{\overline{K_{ID}}}$	$\overline{A_1/A_0}$	$\frac{S_{(A1/A0)}}{\overline{A1/A0}}$
	MPa√m	%	m^{-1}	%
1 - 2	138.0	0.38	-26.9	-11.4
2 - 3	126.5	0.21	-28.7	-6.0
3 - 4	125.3	0.36	-28.4	-10.1
4 - 5	122.7	0.15	-28.8	-3.4
5 - 6	124.1	0.55	-32.2	-5.2

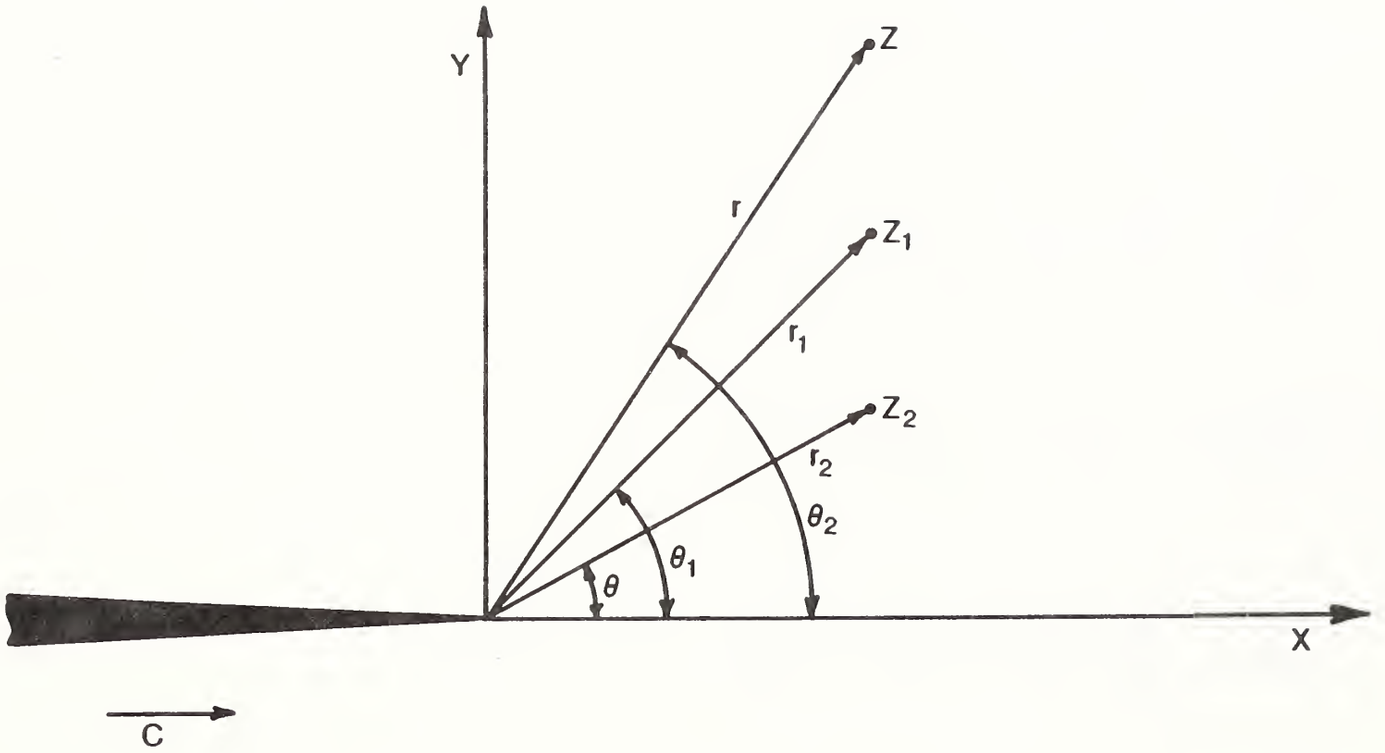

Fig. 3.1 Definition of the coordinate systems used for the development of the dynamic strain field equations.

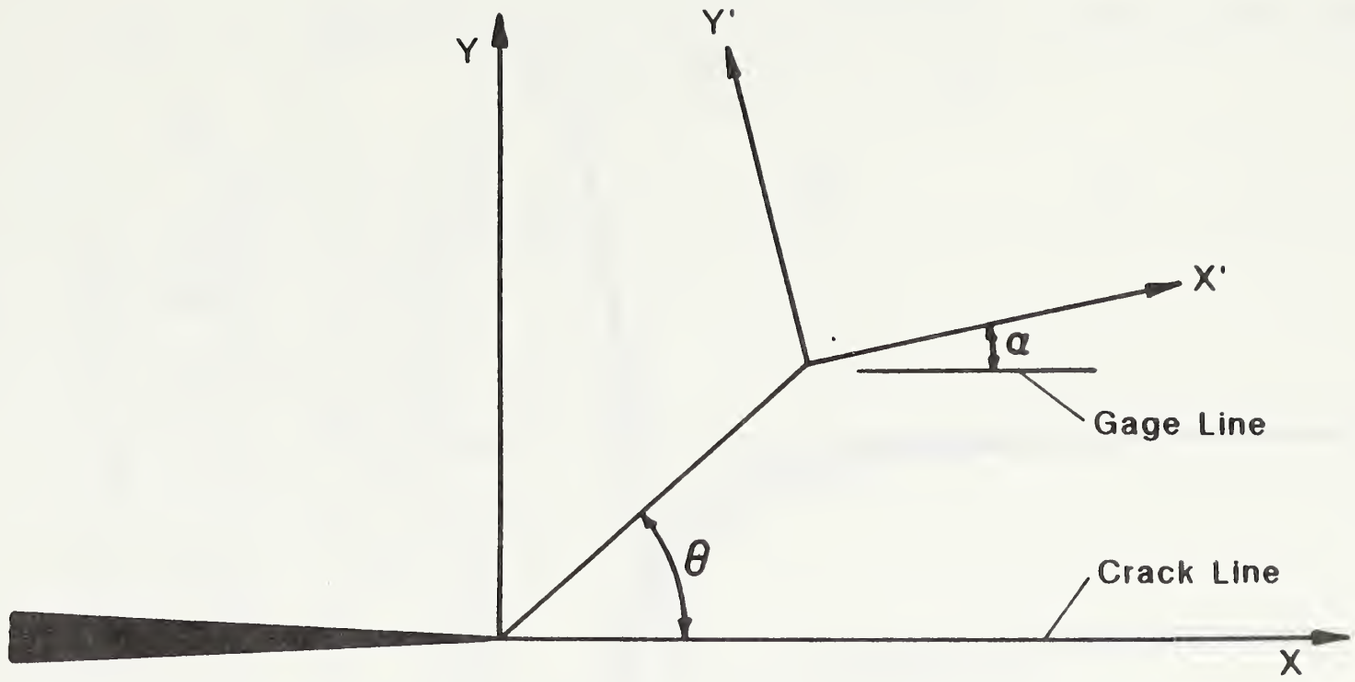

Fig. 3.2 Definition of the rotated coordinate system.

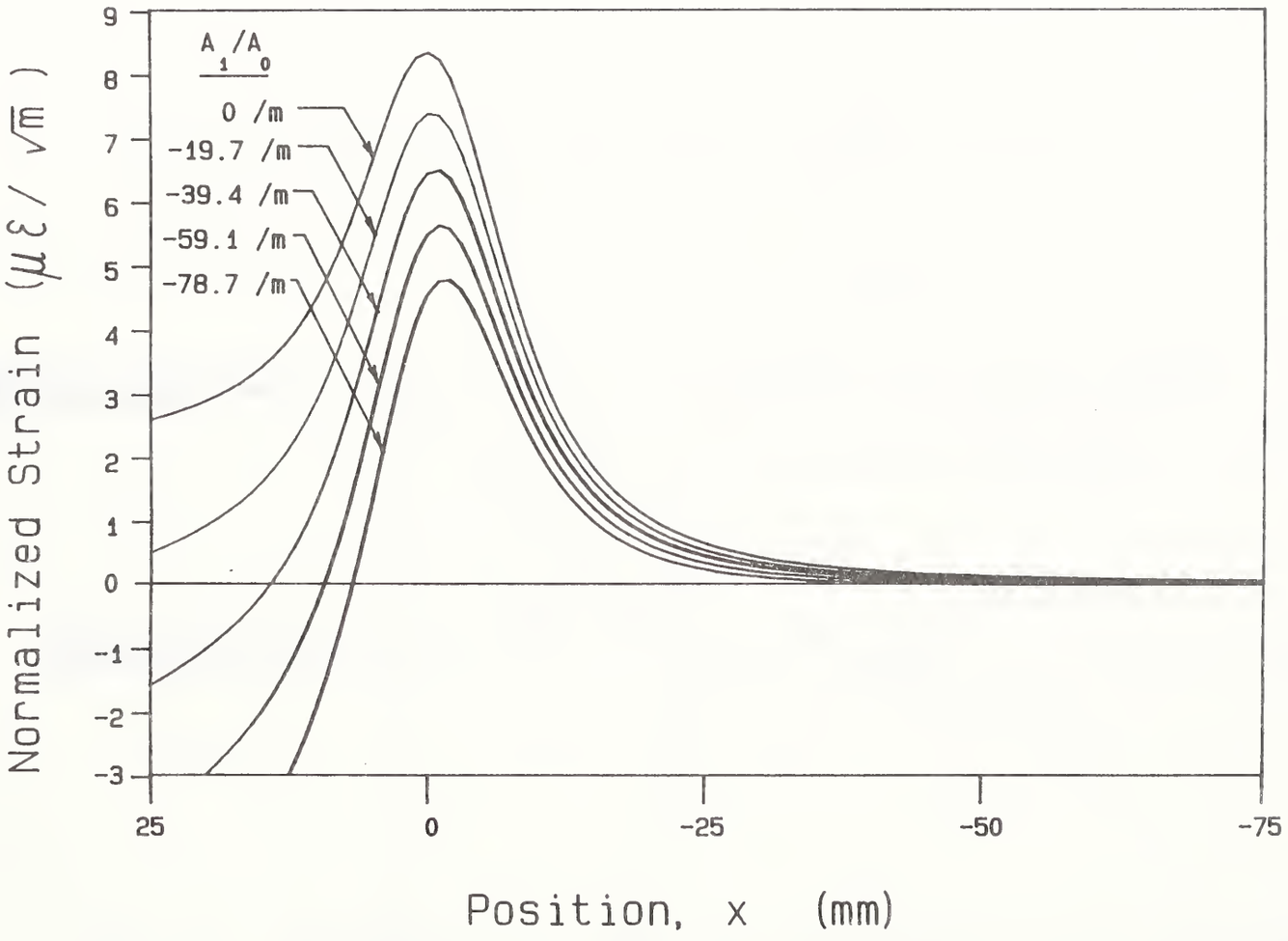

Fig. 3.3 Normalized strain response for a single element strain gage (α = 118.7, y_g = 10.5 mm, c = 656 m/s).

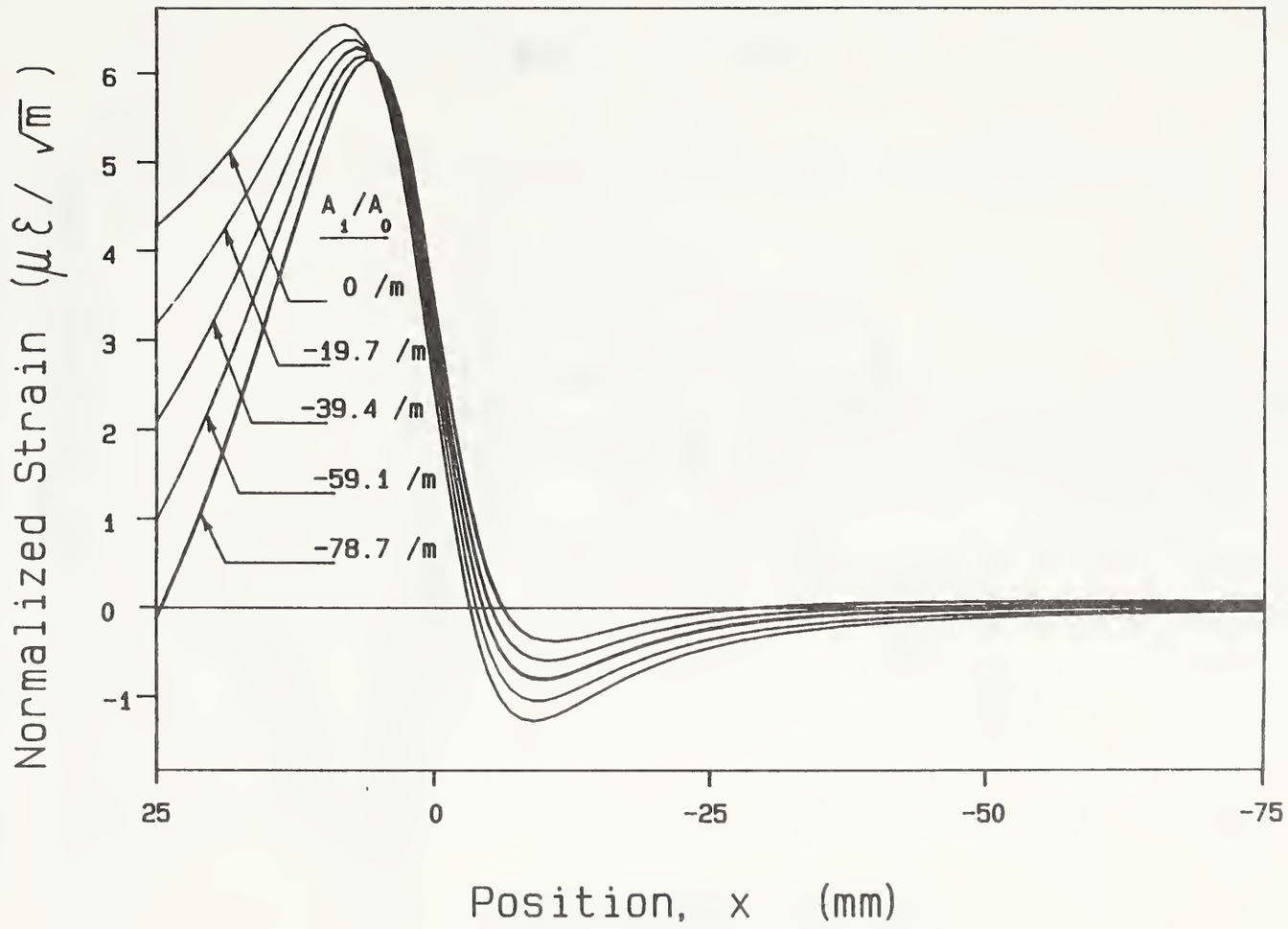

Fig. 3.4 Normalized strain response for a single element strain gage (α = 61.3, y_g = 10.5 mm, c = 656 m/s).

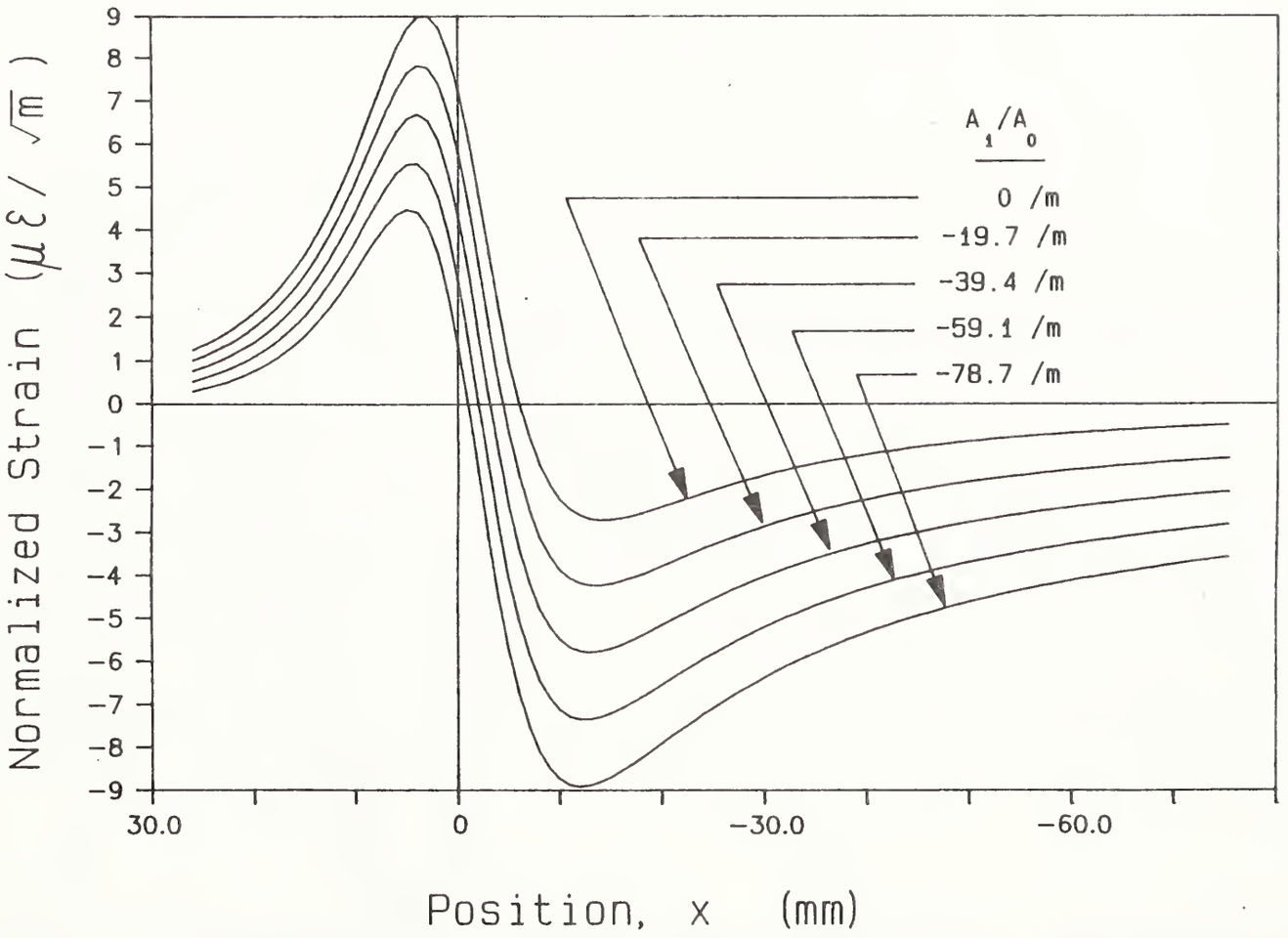

Fig. 3.5 Normalized strain response for a rosette strain gage (α = 45, y_g = 10.5 mm, c = 656 m/s).

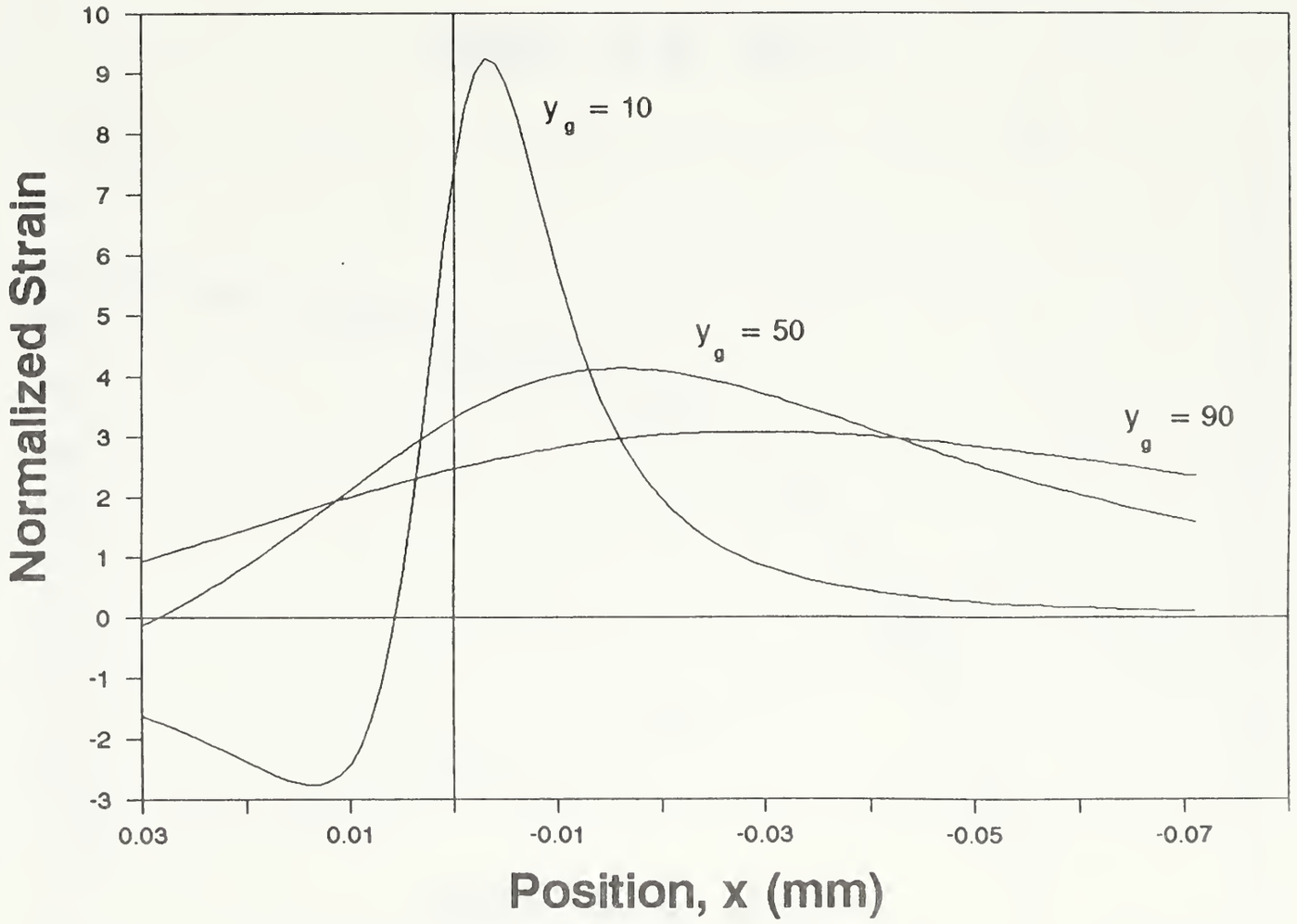

Fig. 3.6 Normalized strain response for a rosette strain gage for y_g = 10, 50, and 90 mm (α = 45, c = 656 m/s)

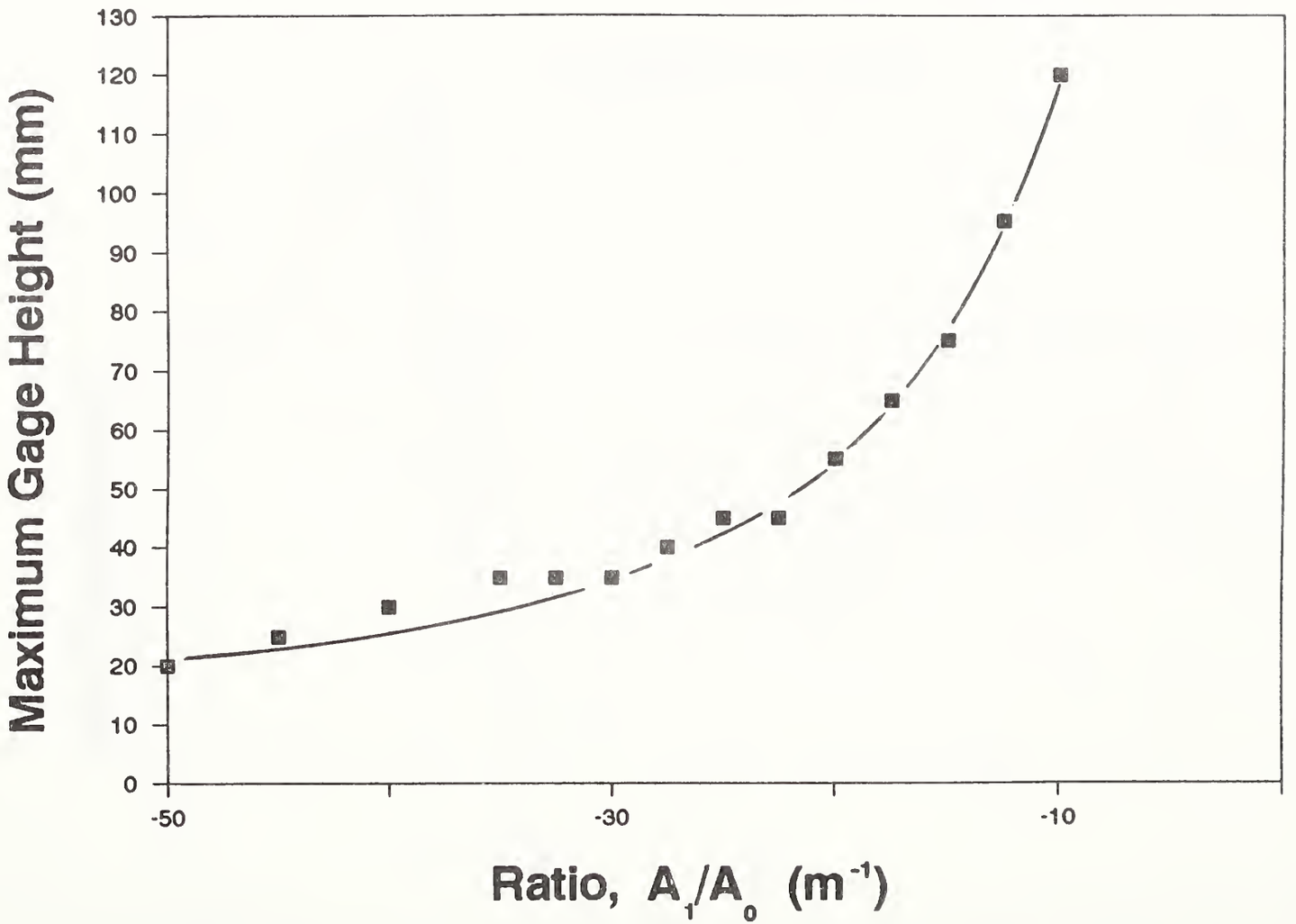

Fig. 3.7 Maximum gage height for existence of a zero crossing for a single element gage

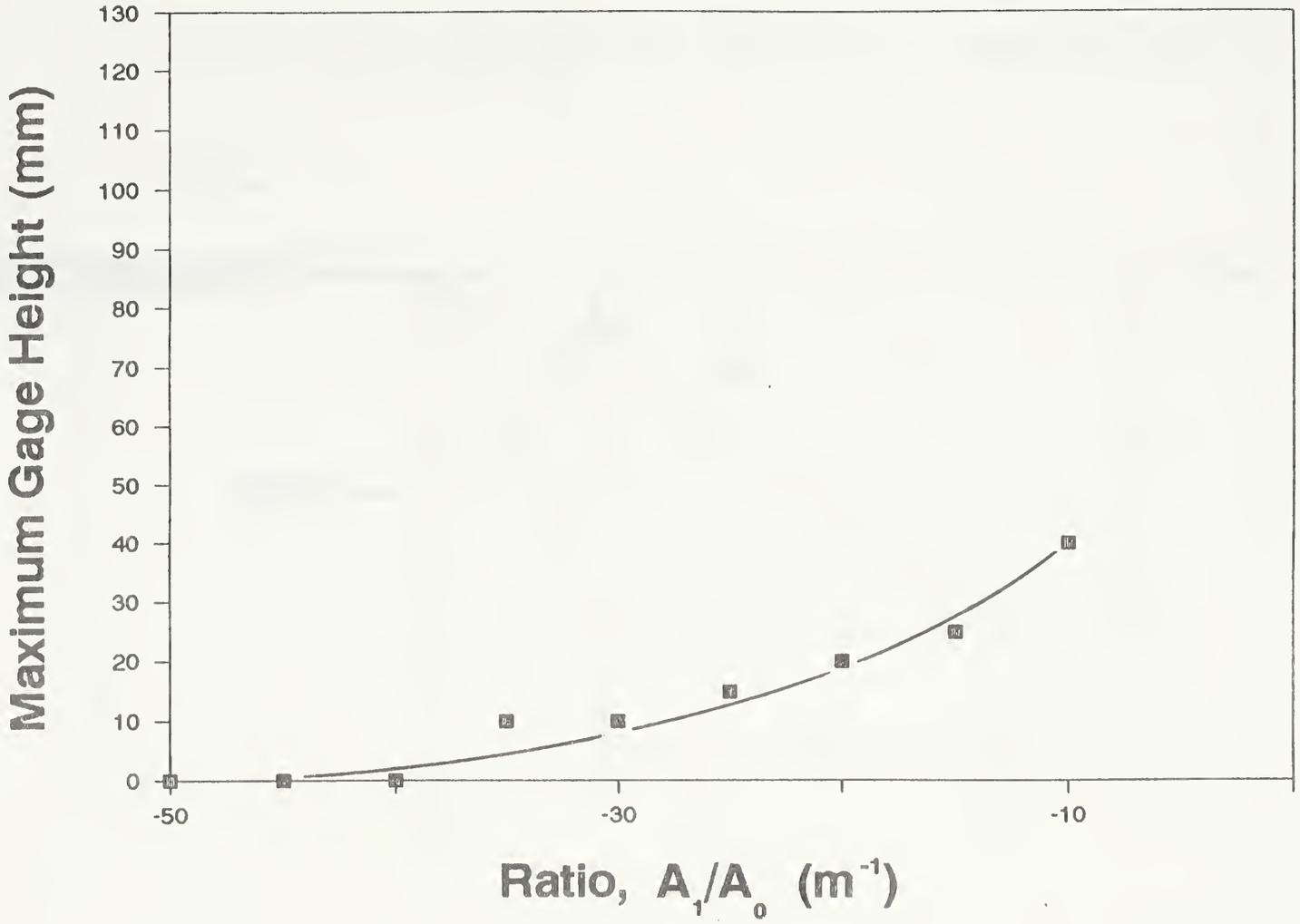

Fig. 3.8 Maximum gage height for existence of a zero crossing for a rosette

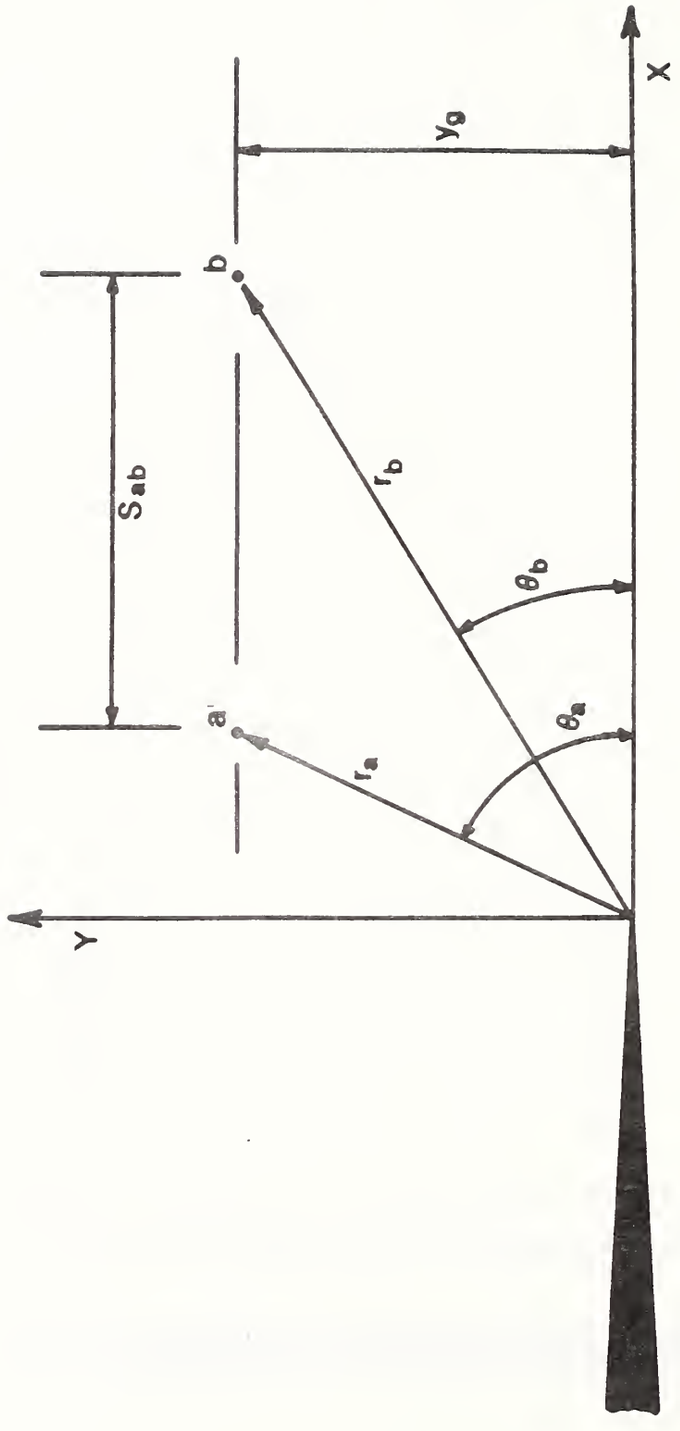

Fig. 3.9 Strain gage positions relative to a propagating crack.

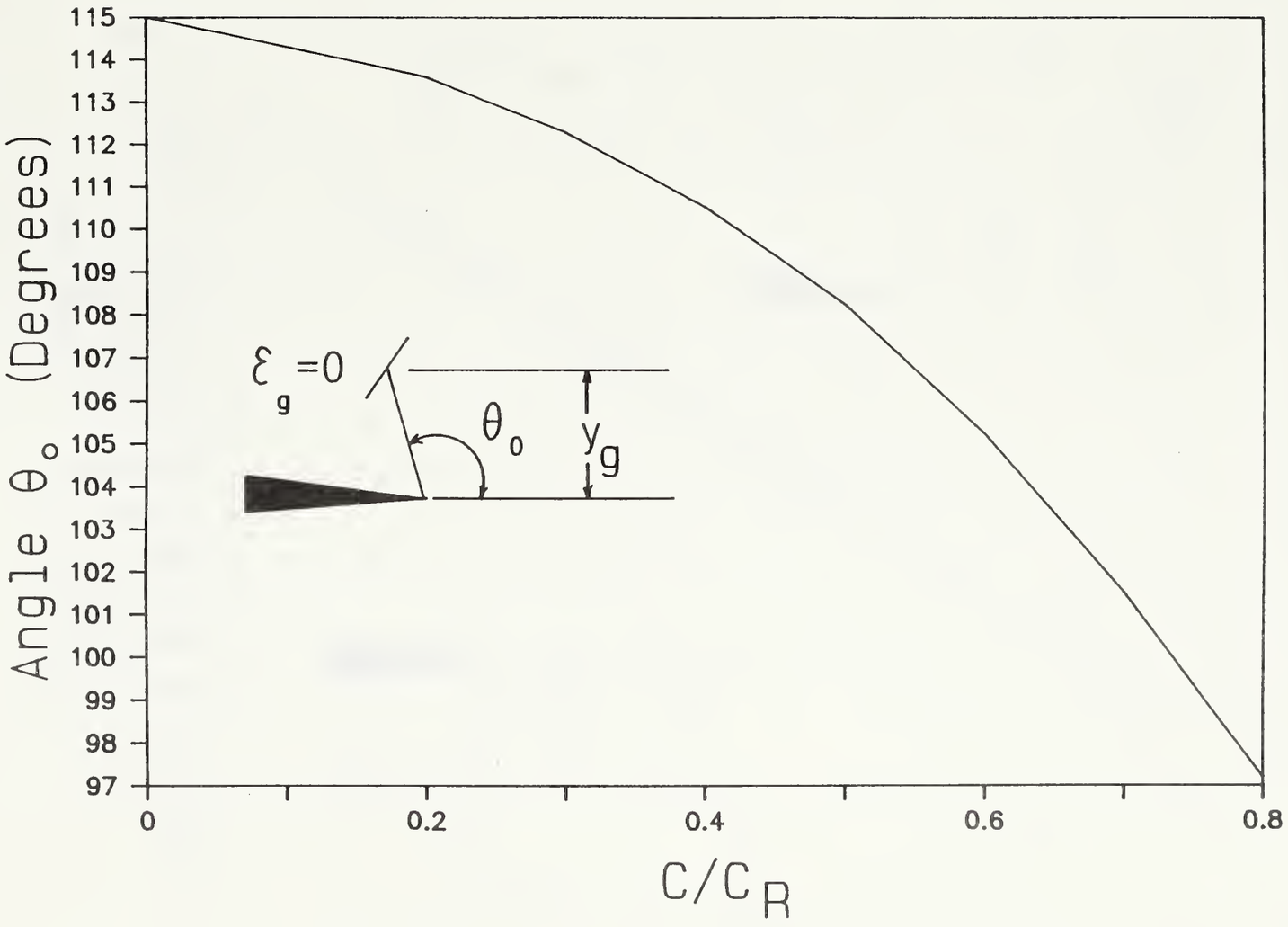

Fig. 3.10 Angle θ_o as a function of c/c_R.

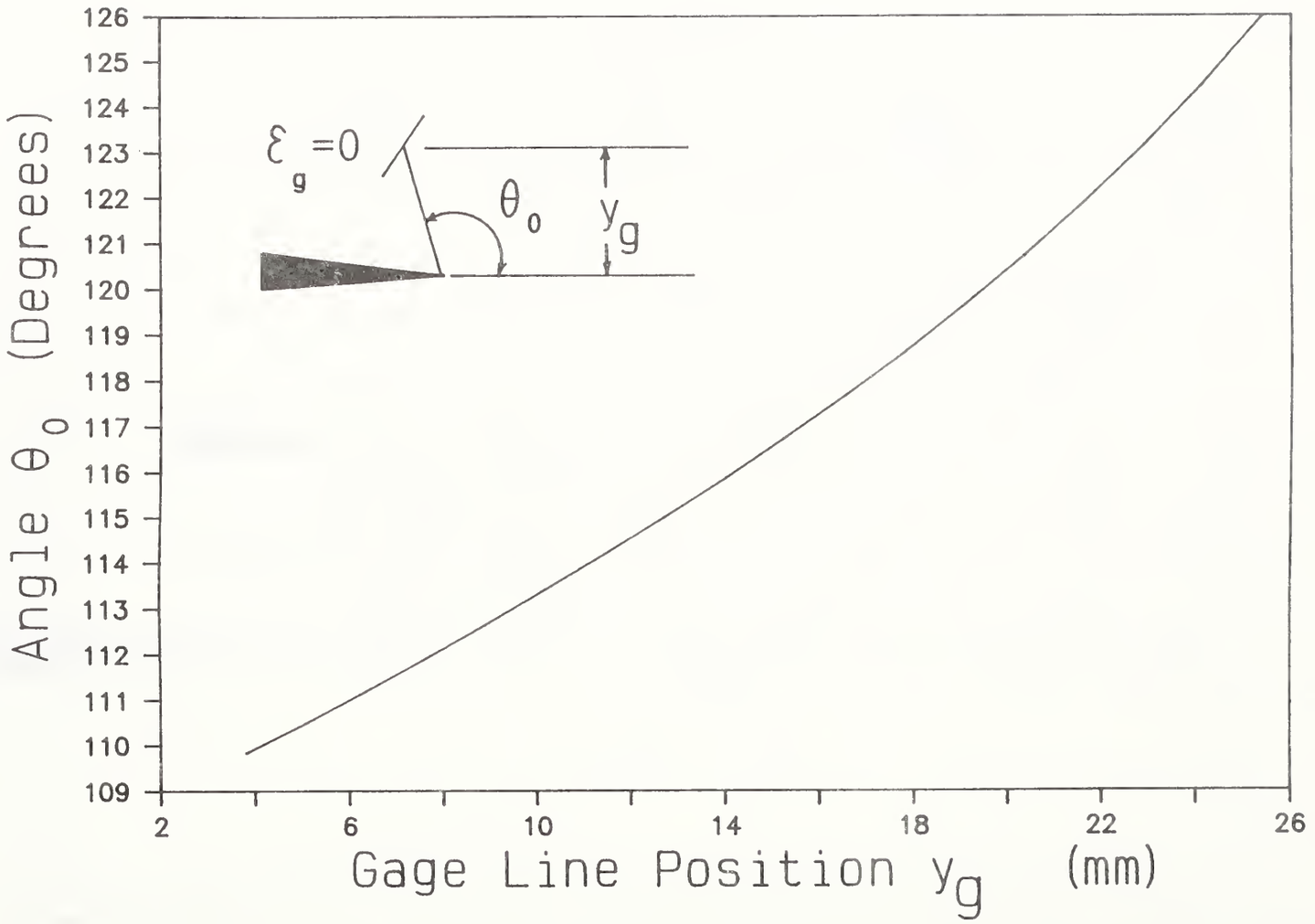

Fig. 3.11 Angle θ_0 as a function of y_g.

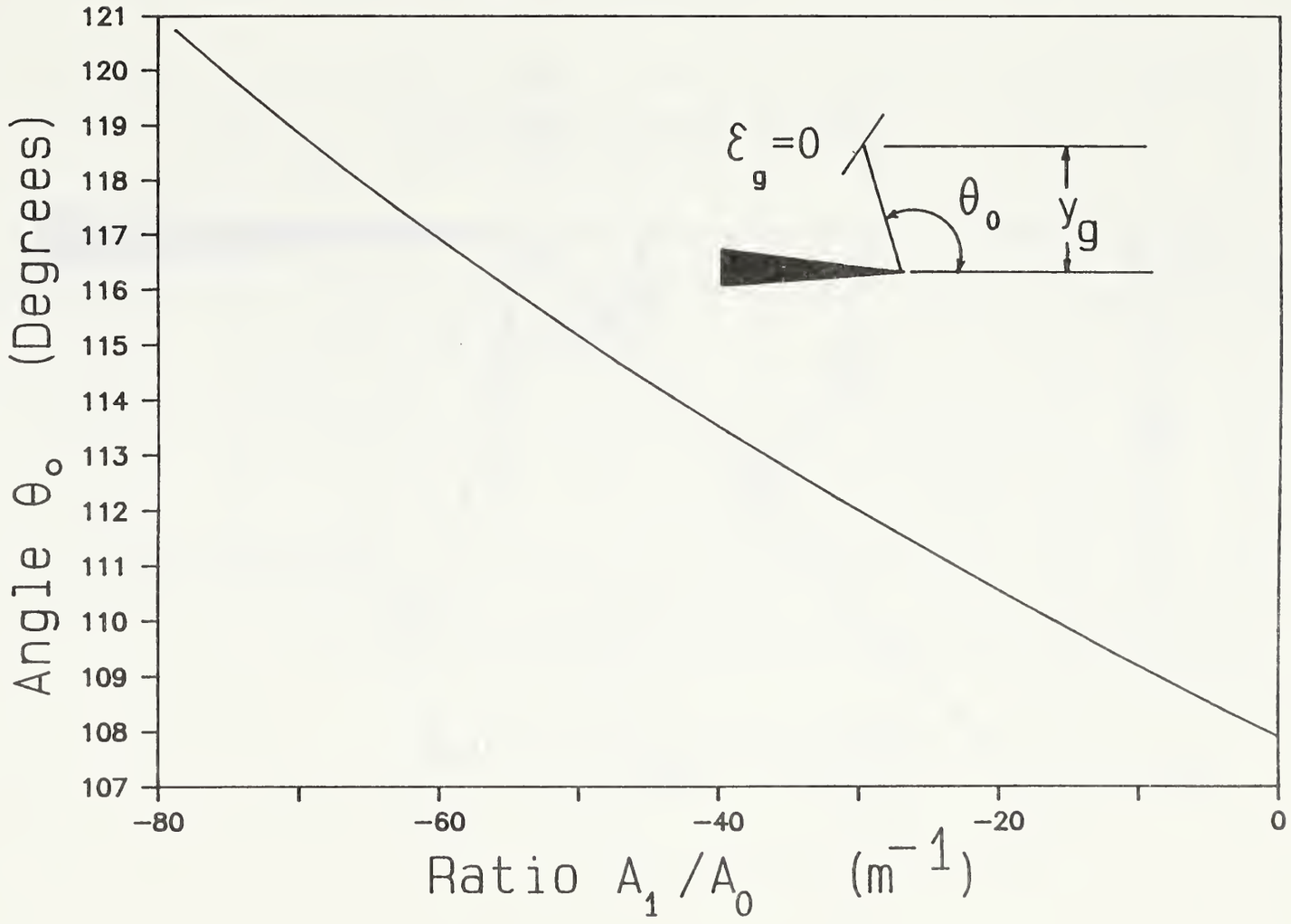

Fig. 3.12 Angle θ_0 as a function of A_1/A_0.

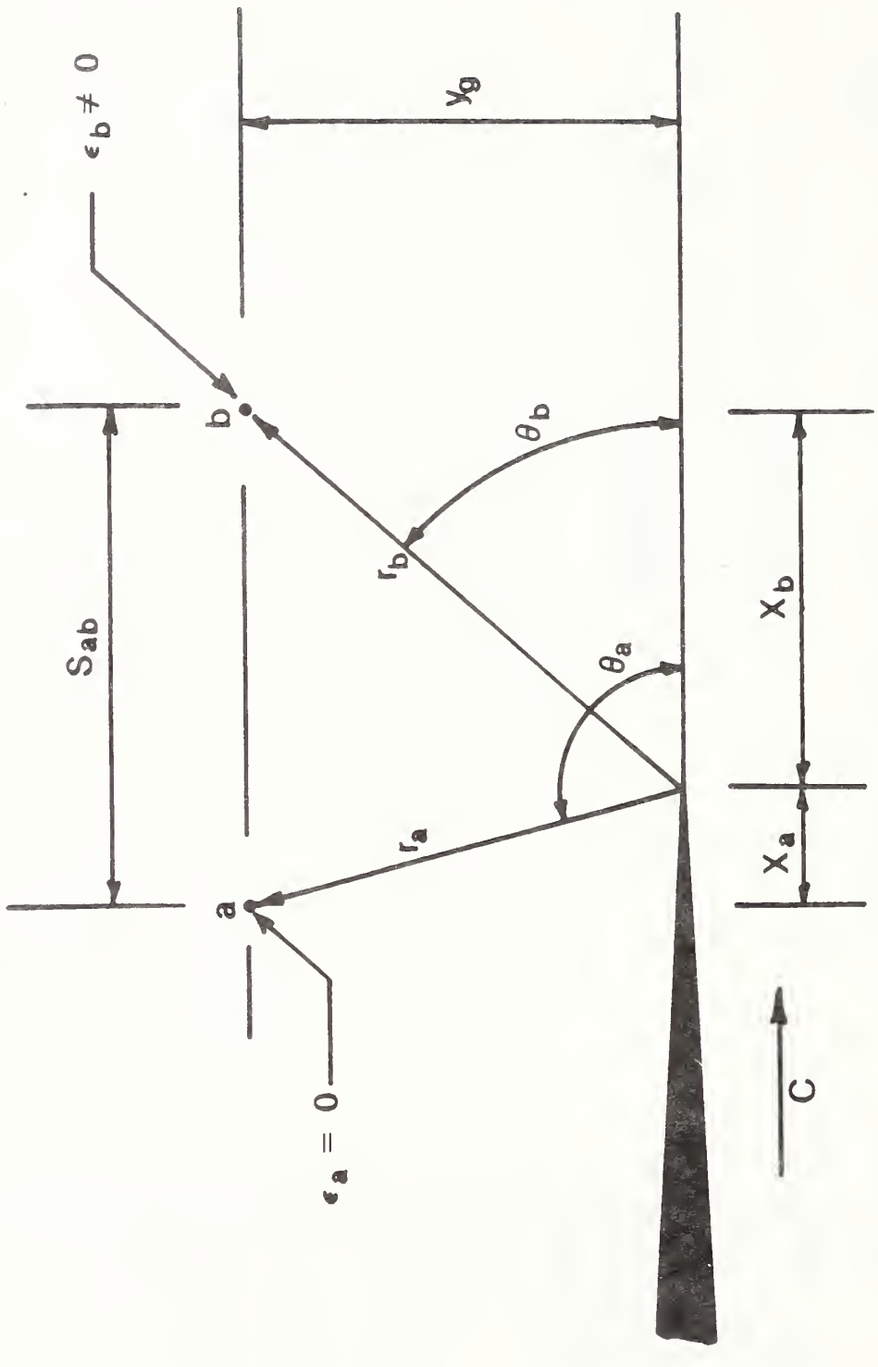

Fig. 3.13 Crack-tip position relative to a gage pair at $\epsilon_a = 0$.

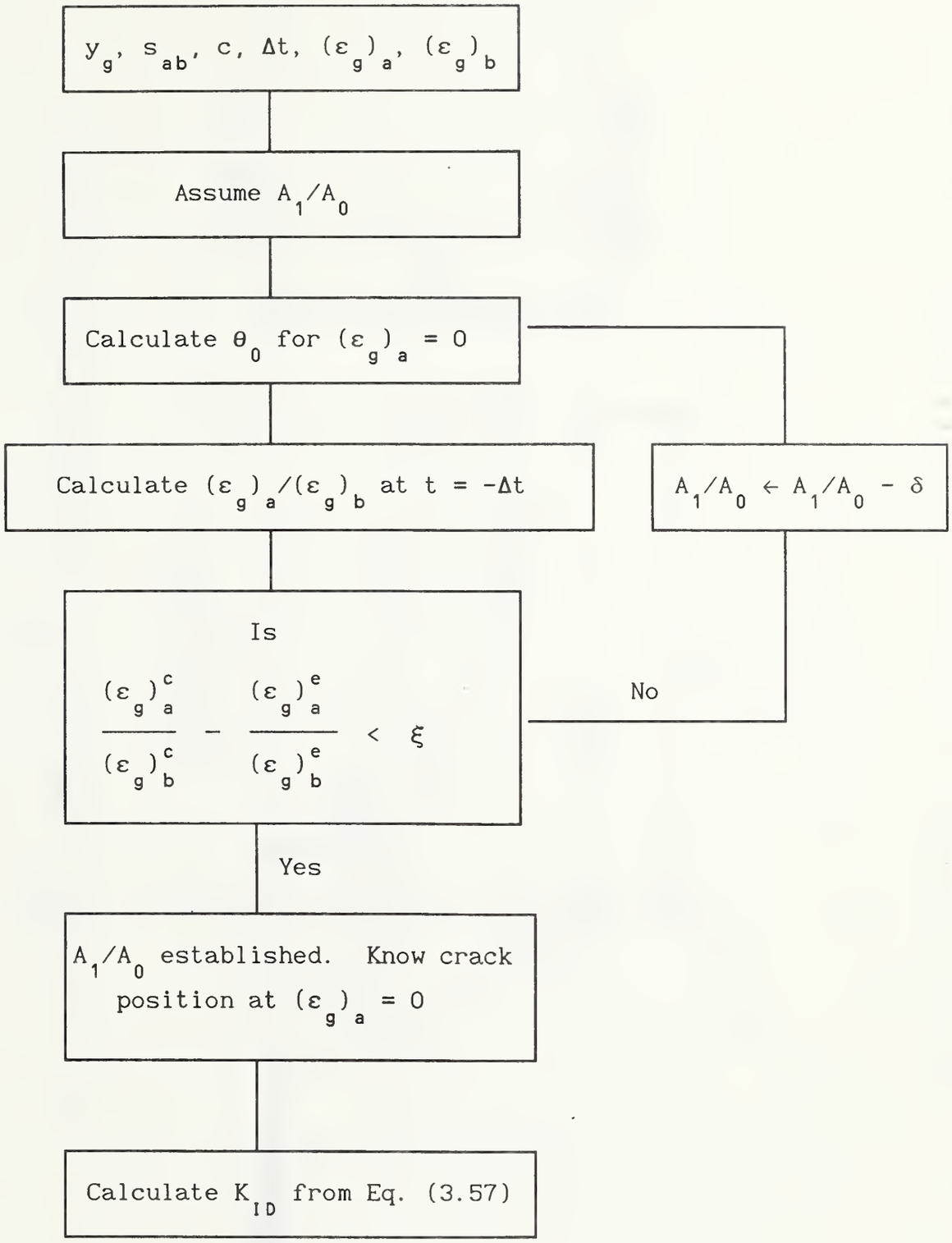

Fig. 3.14 Flowchart for the triangulation and iteration algorithm

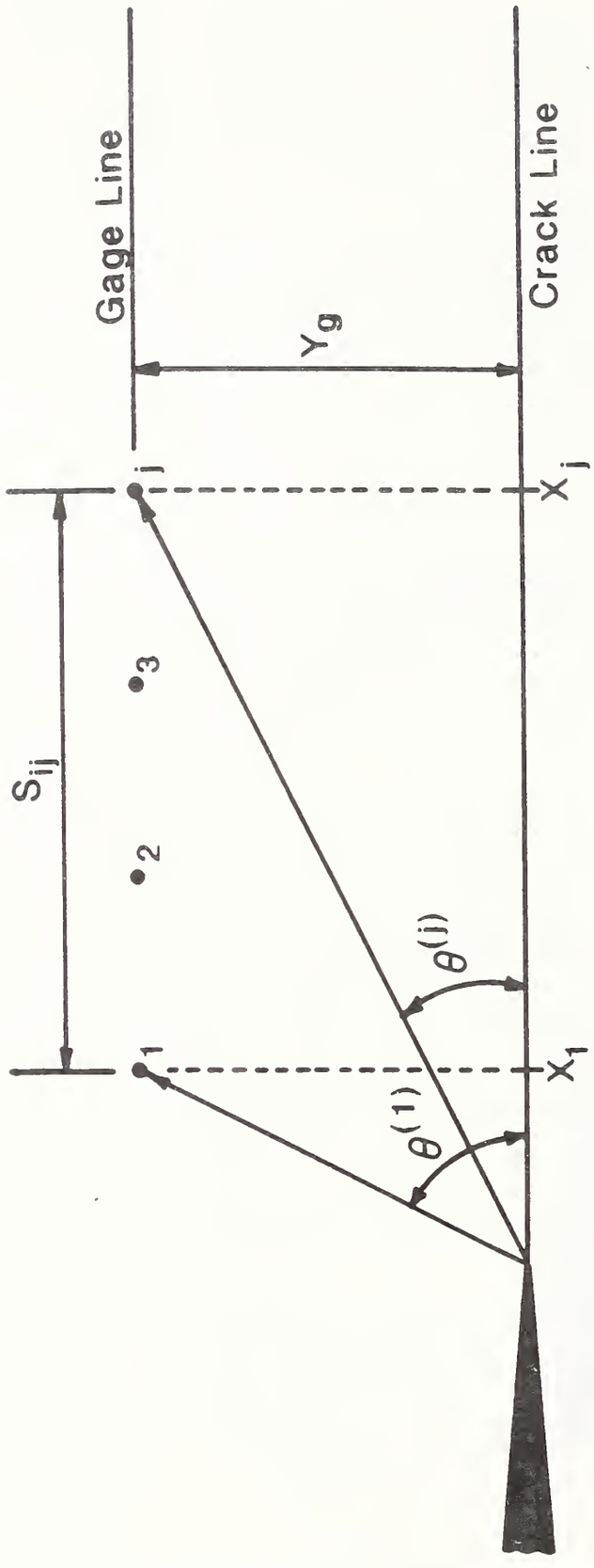

Fig. 3.15 Spatial distribution of strain gages above a propagating crack.

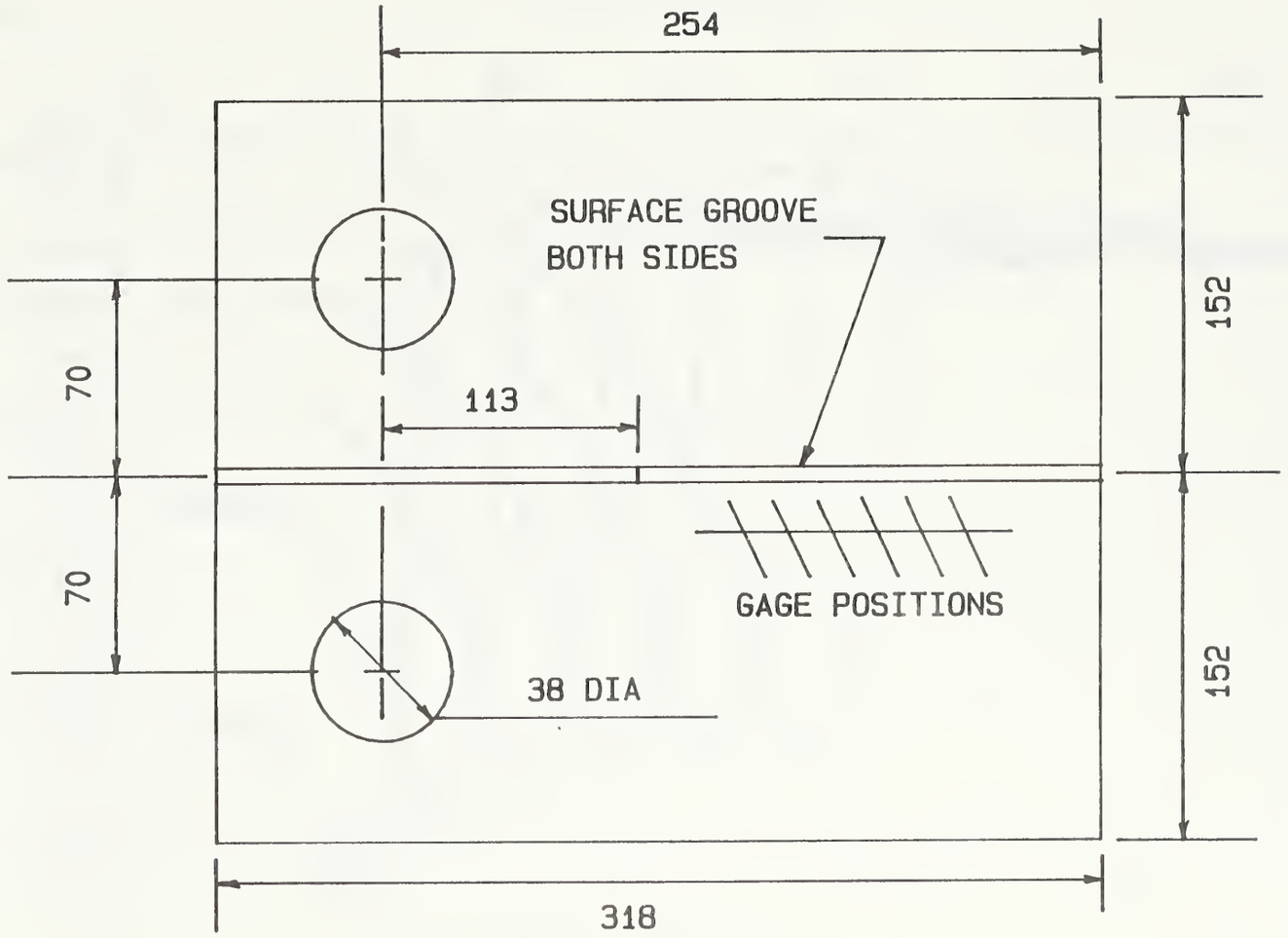

Fig. 3.16 Geometry of the 4340 steel compact specimen.

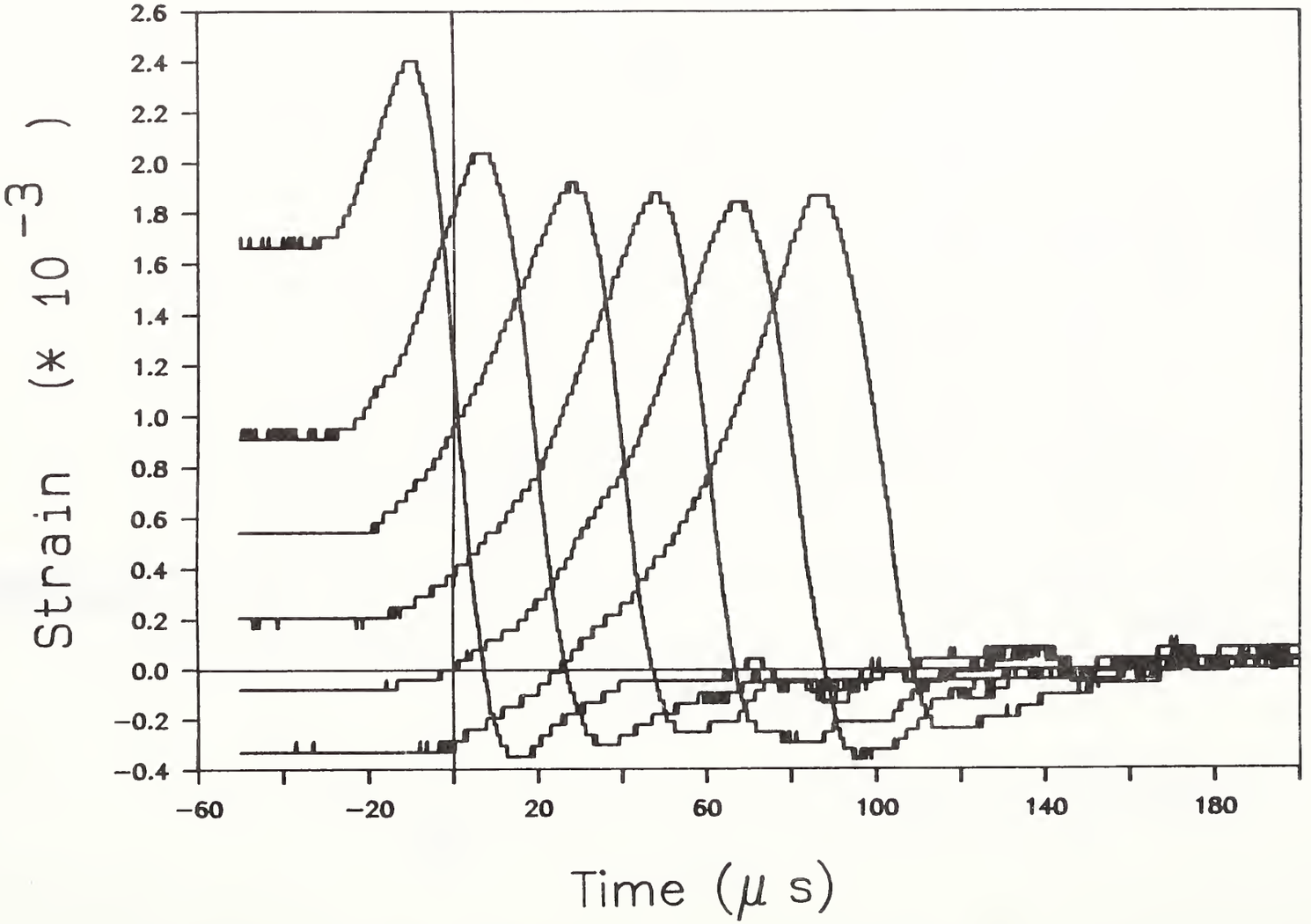

Fig. 3.17 Strain-time records for the compact specimen.

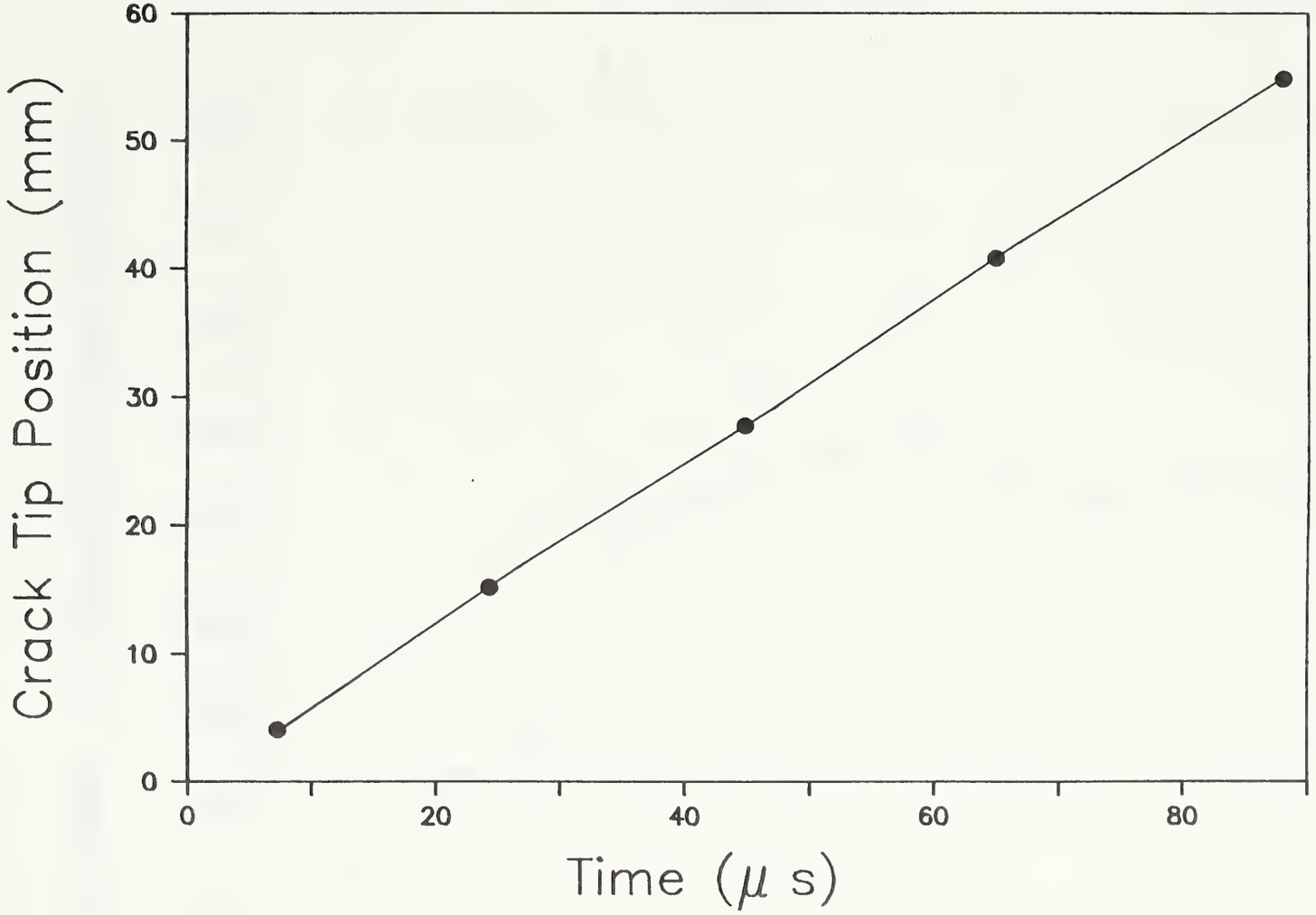

FIg. 3.18 Relative position of the crack as a function of time using the triangulation and iteration algorithm.

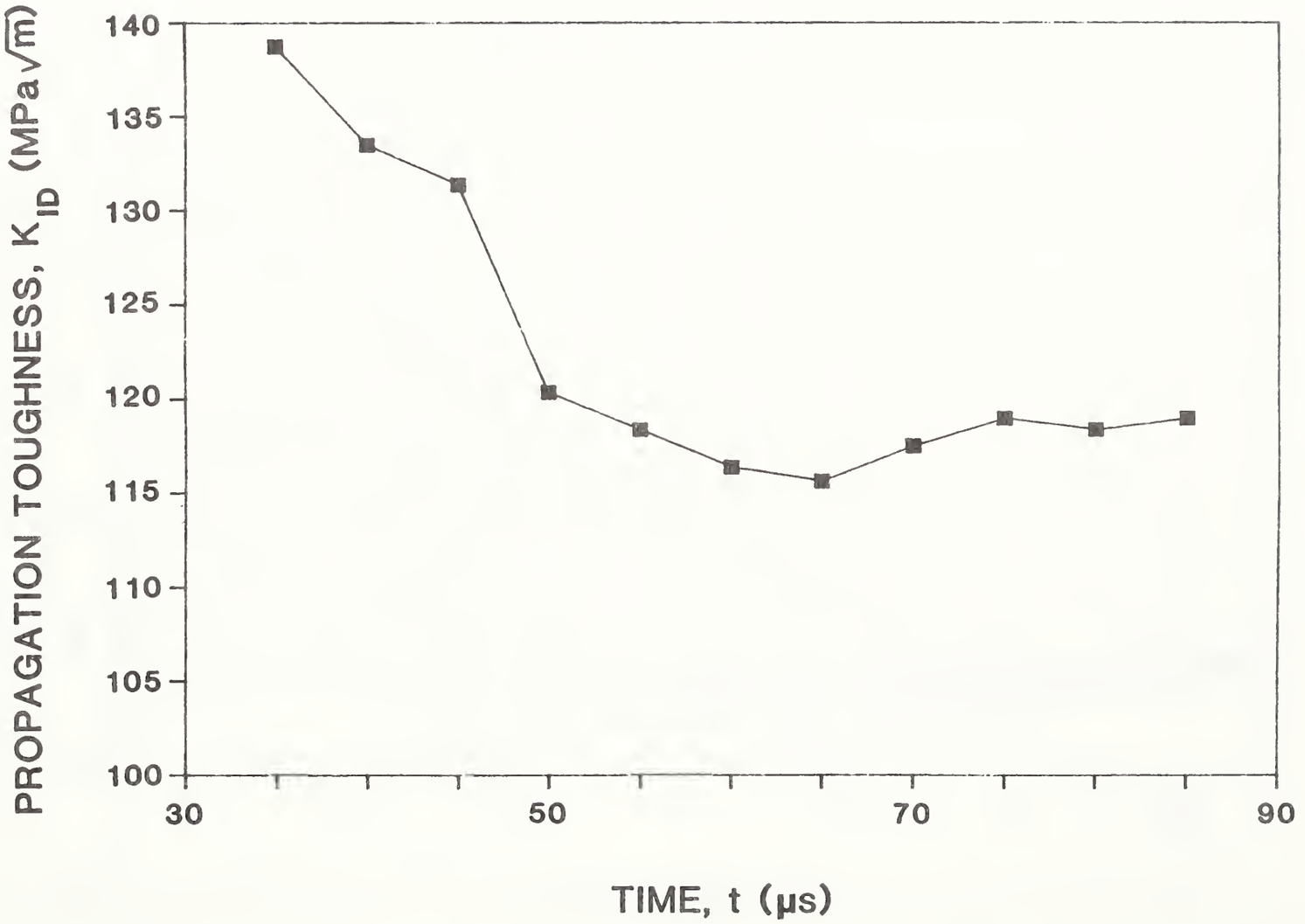

Fig. 3.19 Propagation toughness as a function of time from the spatially overdetermined analysis.

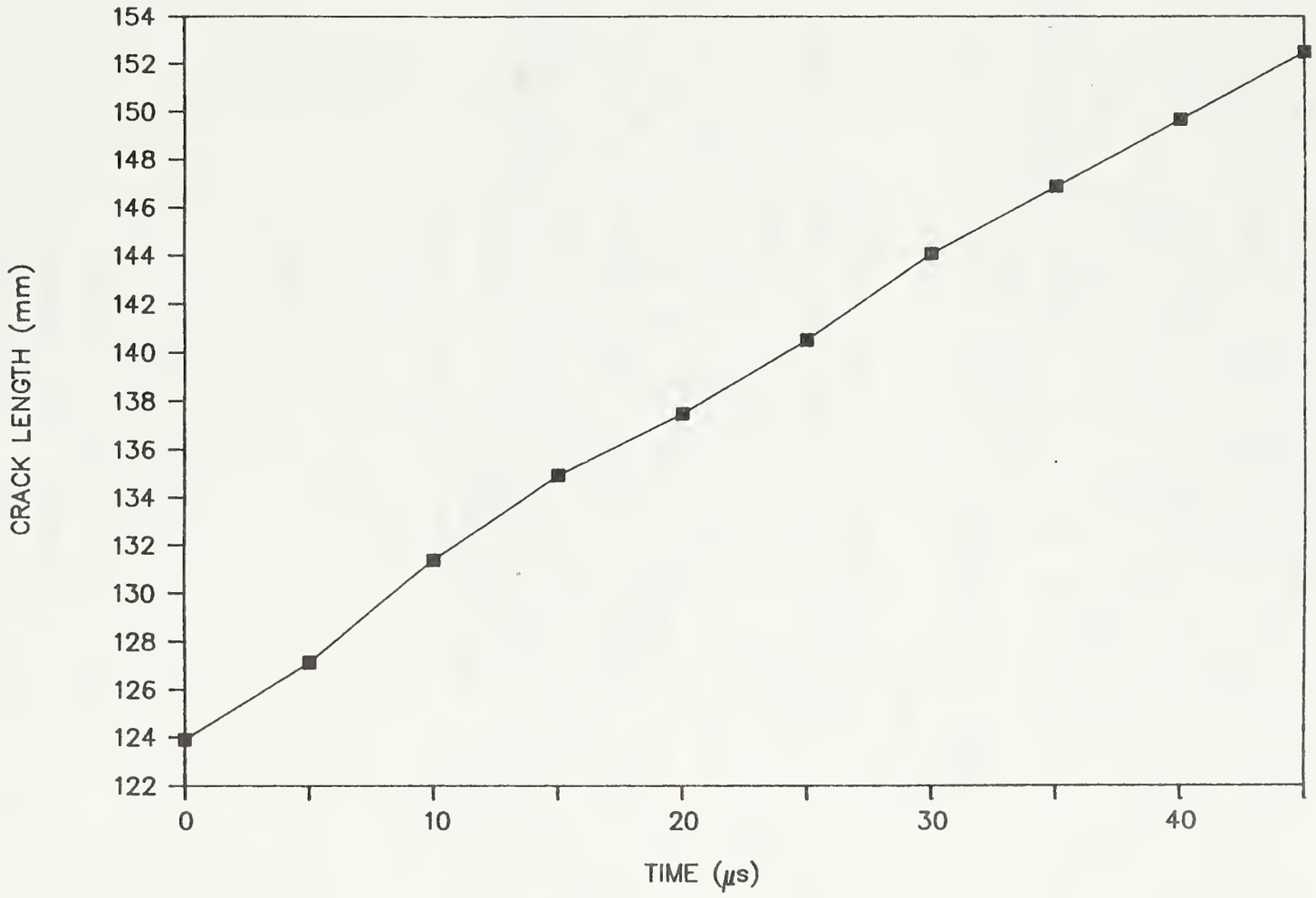

Fig. 3.20 Crack position as a function of time from the spatially overdetermined analysis.

CHAPTER 4

ACCURACY OF THE PARAMETER DETERMINATIONS

Before applying the methodologies developed in the previous two chapters, we examine several important aspects of strain field analysis. The first, and perhaps most important, concerns the extent of validity of the three-parameter expansions for the strain field. Knowledge of these valid zones is essential in determining which gages can be used in a spatially overdetermined analysis of the strains. Selecting gages that lie outside the region of validity of the three-parameter model will introduce errors into the analysis.

The second issue addressed in this chapter concerns the determination of crack tip position from the strain analysis when rosette gages are used. As demonstrated in Chapters 2 and 3, orienting the rosette at $\alpha = 45^{\circ}$ eliminates the contribution of B_0 (σ_{ox}) to the strain response. However, we will show that there are other, more important, reasons for prescribing this gage orientation in terms of the analysis for crack tip position. Finally, conclusions will be made concerning the anticipated error in determining the crack tip position.

4.1 LIMITS ON THE VALIDITY OF THE THREE-PARAMETER MODEL

In Section 3.3, an analysis method was presented which made use of the spatial variations in the recorded strains to determine both propagation toughness and crack tip position. However, information from gages remote from the current crack-tip position may introduce error into the analysis if they lie outside the region where the three-parameter model adequately describes the strain field. In this section we study the extent of validity of the three-parameter model to arrive at criteria for inclusion or exclusion of gages from the analysis.

To assess the strain field surrounding the crack, the static representation presented in Chapter 2 is used, since velocity effects are presumed to be small for this portion of the dissertation. Through knowledge of the higher order (nonsingular) terms, we will examine the error over a reasonably sized area between strain calculated from a three-parameter model and a strain calculated using a high-order model.

Although detailed studies of the nonsingular terms have been carried out for a variety of fracture test specimens [4.1, 4.2], no reliable data are available in the literature for nonsingular terms in the single-edge-notch (SEN) geometry. This particular geometry is of interest because the large-scale, crack-arrest test to be analyzed in Chapter 5 was an SEN specimen. Therefore, we first determine the nonsingular terms for this geometry.

In previous studies [4.1, 4.2], photoelasticity was used to determine the nonsingular terms. In [4.3], Sanford and Link demonstrated that the same information could be obtained by analyzing data from a finite element analysis using the same algorithms as were used for photoelastic analysis. Here, we follow [4.3] and determine the nonsingular coefficients from a finite element analysis (FEA). The FEA stresses local to the

crack tip are collocated in an overdetermined fashion to extract both the stress intensity factor and the nonsingular terms.

The finite element analysis was performed using the two-dimensional, elasto-static PC-based version of the ANSYS code [4.4]. An SEN specimen was modeled using a width of 1.0 m and a crack length-to-width ratio of 0.5. The specimen was modeled to a height of only 1.15 m after it was determined that the stresses were uniform beyond this height. The bottom edge of the specimen was constrained against motion in the vertical direction, and an applied pressure of 1000 MPa was imposed on the specimen's top edge. Finally, the node at the crack tip was constrained against motion in the horizontal direction.

Two-dimensional, isoparametric elements were used throughout the model. No attempt was made to include the singular behavior of the stresses near the crack tip. Using a sufficiently fine mesh and taking advantage of the local collocation procedure with higher order terms, modeling the exact singular behavior is not necessary. 1200 elements were used with the element mesh graded to become finer as the crack-tip was approached. The r.m.s. wavefront for the problem was 55.4 with 2140 degrees of freedom.

Several stages of mesh refinement were used until stress intensity values determined from the FEA agreed with values calculated from Tada [4.5]. For this geometry and loading, the exact value of $K_I = K_{TADA} = 354.0$ MPa $\sqrt{m}$. The final mesh is shown in figure 4.1. At this stage of the mesh refinement, $K_I = K_{FEA} = 350.0$ MPa $\sqrt{m}$ and $K_{FEA}/K_{TADA} = 1.01$. The modeling was therefore considered to be adequate. The distribution of the in-plane stresses determined from the finite elements (σ_{xx}, σ_{yy}, and σ_{xy}) along the crack line is shown in figure 4.2.

Stresses were collocated across a 0.50 m x 0.50 m area surrounding the crack tip. As suggested in [4.3], no data were used from a small region (0.05 m x 0.05 m) surrounding the crack

tip where the finite elements are incapable of modeling the singularity in stresses. Nodal stresses were used as data for the collocation procedure. This provided three equations (σ_{xx}, σ_{yy}, and σ_{xy}) for each of the 191 nodes in the collocation region. The numerical details of collocation methods can be found in [4.6] and [4.7].

The collocation was performed using the series expansions from the static representation of stresses presented in Chapter 2. Initially, one term from each of the Z(z) and Y(z) series was used. Additional terms were then added in pairs (one from each series) until the residual error converged. The residual used to determine convergence was

$$\bar{r} = \frac{1}{J\,\sigma_{\infty}} \left[\sum_{j=1}^{J} (\sigma_{ij}^{COLLC} - \sigma_{ij}^{FEM})^2 \right]^{1/2}, \qquad (4.1)$$

where

J = total number of data points,

σ_{∞} = remotely applied stress,

σ_{ij}^{COLLC} = stress component calculated from the collocation,

σ_{ij}^{FEM} = stress component from the finite elements.

As shown in figure 4.3, the residual decreased with increasing order of the model until it stabilized at 10 coefficients (5 terms in each of the Z(z) and Y(z) series). The value of the residual at 10 coefficients, $\bar{r}$ = 0.075 %, indicates good modeling of the stresses across the collocated area. For comparison, in the boundary collocation study of [4.7], the residual at convergence calculated in a similar manner was $\bar{r}$ = 0.20 %.

We will therefore assume that a twelve-parameter model more than adequately describes the stress field across the collocation region. The numerical values of the coefficients are given in table 4.1. Shown in figure 4.4 is a comparison of the finite

element stresses with the stresses calculated using the twelve-parameter model. The best agreement is with the σ_{yy} stress component due its large magnitude. The σ_{xx} and σ_{xy} components are matched well, considering their smaller magnitudes. The data plotted in figure 4.4 are across y = 0.123 m, roughly halfway between the crack plane and the top of the collocated region. Similar behavior for the comparison was found on other nodal lines as well.

Having an "exact" solution for the strain field around the crack tip now enables us to study the error in using a three-parameter strain field representation. We study this error by simply choosing a point in the field, calculating the strain at this point using both three- and twelve-parameter models, and comparing the two strain values. As we vary the position of the point throughout the field, we can begin to see where strain gages provide information usable in the spatially overdetermined analysis procedure developed in Chapter 3.

The first comparison is done for the strain gage rosette. figures 4.5 - 4.7 show areas in the field surrounding the crack tip where the difference between three- and twelve-parameter strain calculations are less than 2, 5, and 10%. Note the dramatic increase in the size of the valid zone when a 10% error is acceptable. In all cases the region extends at least twice as far ahead of the crack tip as behind it.

For the analysis of dynamic crack propagation, the 5% error plot provides an acceptable basis for establishing criterion for gage selection. The 1.0 m width of the modeled specimen allows for an easy conversion to a/W ratios for the criterion. We conclude that for the strain gage rosette, data from gages a distance x_g from the crack-tip may be included in an overdetermined analysis, provided $-0.15 \leq (x_g/W) \leq 0.30$ with $(y_g/W) \leq 0.1$. The value of y_g is usually constrained by thickness

considerations and is typically taken as $(y_g)_{MIN} = t/2$, where t is the specimen thickness [4.8]. For larger values of y_g the usable range for x_g decreases but may be obtained from figure 4.6.

Finally, for the single-element strain gage, error plots for 2, 5, and 10% are shown in figures 4.8 - 4.10. In comparison to the rosette, the region of validity is markedly smaller for the single element gage. Again using the 5% error plot for the case of dynamic crack propagation, we conclude that $-0.175 \leq (x_g/W) \leq 0.1$ with $(y_g/W) \leq 0.13$. Again, y_g must satisfy the thickness criterion mentioned in the previous paragraph.

4.2 DETERMINATION OF CRACK TIP POSITION USING STRAIN GAGE ROSETTES

Arguments have been presented for orienting strain gage rosettes at $\alpha = 45^\circ$ in order to eliminate the contribution of the B_0-term to the strain response. However, many crack propagation experiments have been performed using strain gage rosettes oriented at $\alpha = 0^\circ$. In the course of analyzing one of these tests with rosettes at $\alpha = 0^\circ$, we encountered problems in determining the crack tip position. These problems persisted even if the nonsingular coefficients used in the series representation were prescribed to their exact values. The study conducted to determine the reasons for the difficulty in determining the crack-tip position is presented in this section.

To examine the problem of locating the crack tip from the strain analysis when $\alpha = 0^\circ$, synthetic data were generated using the static representation of the strain field presented in Chapter 2. These synthetic data provided input free from experimental error for a spatially overdetermined analysis. Data were generated for both $\alpha = 0^\circ$ and $\alpha = 45^\circ$ under identical states of stress for a series of six strain gage rosettes spaced 40 mm apart and located 65 mm above the crack path, figure 4.11. Using coefficient values

for the SEN specimen analyzed in Section 4.1, the series coefficients were prescribed as A_0 = 139.0 Mpa $\sqrt{m}$, A_1 = -270.7 Mpa $m^{-1/2}$, and B_0 = -12.7 MPa. The strains for each of the six rosettes with orientation $\alpha = 0^0$ and $\alpha = 45^\circ$ are listed in table 4.2.

For the $\alpha = 0^\circ$ rosettes, there are four unknowns in the analysis: A_0, A_1, B_0, and the angle the crack tip makes with the first gage, $\theta^{(1)}$. The overdetermined analysis provided meaningful results for these variables only when the value of $\theta^{(1)}$ was initially estimated at nearly its exact value. Even if the initial estimate for $\theta^{(1)}$ was in error by as little as 10% from the exact value, the algorithm would converge to a false solution. That is, further iterations of the solution algorithm would not alter the values of the unknown variables. Convergence to a false solution would occur regardless of the accuracy of the estimates for the series coefficients. Furthermore, similar problems were encountered with the estimate for the B_0 term. If the initial estimate for B_0 was in error by only 10% and exact values were provided for the remaining variables, the algorithm would not converge to the exact solution.

In contrast with the analysis for $\alpha = 0^\circ$, the same analysis for the $\alpha = 45^\circ$ rosettes was numerically well behaved. Initial estimates for the three variables (A_0, A_1, and $\theta^{(1)}$) could be given any reasonable values and the algorithm quickly converged to the exact solution. Only when physically unreasonable values were specified for the initial estimate of $\theta^{(1)}$ would the algorithm diverge. For example, if $\theta^{(1)}$ was initially estimated to be 120° instead of the exact value of $\theta^{(1)} = 45^\circ$, the algorithm diverged. If $\theta^{(1)}$ was initially estimated to be within 40% of its exact value, the algorithm converged regardless of the estimates for A_0 and A_1. Since $\theta^{(1)}$ can easily be estimated to within 40%, this limitation does not present any difficulty. Most important, for

data from the rosettes with $\alpha = 45^{\circ}$, the algorithm would either converge to the exact solution or it would completely diverge. In no instance did the algorithm converge to a false solution.

Since the convergence of the solution for the $\alpha = 45^{0}$ rosettes is completely controlled by the nonlinear parameter, $\theta^{(1)}$, the implementation of the solution from a practical standpoint is much simpler. After making the initial estimates for A_0, A_1 and $\theta^{(1)}$, the algorithm will either converge to the exact solution or it will diverge. If it diverges, simply change the estimate for $\theta^{(1)}$ until the algorithm converges to the exact solution.

There are two reasons for the behavior of the numerical results for data taken from the $\alpha = 0^{\circ}$ rosettes. First, the B_0 term is spatially constant; that is, it is independent of the (r,θ) coordinates. Therefore, it contributes no information pertaining to the location of the crack tip. A parallel can be made to the general problem in instrumentation studies of measuring a small signal over a large dc voltage offset. The B_0 term acts as the dc level in the strain response and shifts the response, positively or negatively, depending on the sign of B_0. This shifting contains no information relating to the position of the crack tip.

Second, the behavior of the numerical results also suggests that the solution surface in least squares space for $\alpha = 0^{\circ}$ is either relatively flat or contains many local minima when compared to the surface for $\alpha = 45^{\circ}$. Since the number of variables precludes viewing the entire solution surface (a five-dimensional "surface"), a three-dimensional projection of the A_0, $\theta^{(1)}$ solution surface was constructed with A_1 and B_0 prescribed to their exact values. A contour plot of the surface for $\alpha = 0^{\circ}$ is shown in figure 4.12. The contours represent constant values for the normalized least squares residual defined as

$$\bar{r} = \left[\sum_{j=1}^{J} (\varepsilon_j^s - \varepsilon_j^c)^2 \right]^{1/2} / \left[J \sum_{j=1}^{J} \varepsilon_j^s \right], \qquad (4.2)$$

where

ε_j^s = synthetic strain at gage j,

ε_j^c = calculated strain at gage j using current values of A_0 and $\theta^{(1)}$,

J = total number of gages.

Typically, for analyzing actual strain records, the criterion for convergence is $\bar{r} \leq 0.5\%$.

The surface in figure 4.12 exhibits some rather interesting characteristics. First, the contours are highly elongated and most do not close on themselves over the large range of values for $(A_0, \theta^{(1)})$. Second, local minima occur in the long valley bracketed by the $\bar{r} = 1.5$ contour. We can therefore see that there are two problems with the $\alpha = 0^\circ$ analysis which are typical of problems in nonlinear least squares analysis; namely, the existence of many local minima as well as a long, flat valley. The Newton-Raphson technique used to solve the nonlinear system relies on derivatives with respect to the unknown variables to provide a direction for the solution. In the valley bracketed by the $\bar{r} = 1.5$ contours the derivatives cannot direct the solution to the correct, absolute minimum.

In [4.9], a thorough discussion is made on the shape of the contours in the residual space as they relate to "ill conditioning" or parameter identification. Elongated contours (banana shaped) indicate that the function of the variables can be estimated precisely; yet the individual parameters can not be obtained. Note in figure 4.12 the elongation of the contours which indicates exactly the type of problem described in [4.9].

For comparison, a contour plot of the three-dimensional projection for the least squares solution surface with $\alpha = 45^{\circ}$ is shown in figure 4.13. In contrast with the surface of figure 4.12, this surface contains a distinct minimum near the exact values of $A_0 = 139.0$ MPa $\sqrt{m}$ and $\theta^{(1)} = 45^{\circ}$. The topology of the surface allows the Newton-Raphson procedure to provide an accurate direction for the solution to follow. This explains the difference in the behavior of the numerical results for $\alpha = 0^{\circ}$ and $\alpha = 45^{\circ}$.

4.3 ACCURACY OF THE DETERMINATIONS

One final issue to discuss in terms of the strain analysis is the accuracy of the determination of the crack tip position and series coefficients using strain gage rosettes. The series coefficients determined in Section 4.1 provide an opportunity to address this question. The synthetic strain data which was generated in Section 4.2 for a series of rosettes oriented at $\alpha = 45^{0}$ was used for this study. The strains $(\varepsilon_{y'y'} - \varepsilon_{x'x'})$ at these gages were used for input into the spatially overdetermined analysis algorithm with crack tip position as an unknown. The calculated value for crack tip position was then compared to the actual value.

The spatially overdetermined analysis for these strains was made using inexact values for the initial estimates of the variables ($A_0 = 100.0$ MPa $\sqrt{m}$, $A_1 = -200.0$ MPa $m^{1/2}$, and $\theta^{(1)} = 65.0^{\circ}$). The algorithm converged rapidly, with a resulting value of $\theta^{(1)} = 45.1^{\circ}$ with a normalized residual error of 0.01%. This result for $\theta^{(1)}$ compares well (0.2%) with the exact value of $\theta^{(1)} = 45.0^{\circ}$ obtained from the rosette positions indicated in figure 4.11. In terms of crack length, $x_g = 64.8$ mm which compares well with the actual value of $x_g = 65$ mm. The difference of 0.3% in

locating the position of the crack tip is certainly acceptable. The values for A_0 and A_1 at convergence were 138.6 MPa $\sqrt{m}$ and -273.2 MPa $m^{1/2}$, which compare well (0.3% and -0.9%) with the actual values of A_0 = 139.0 MPa $\sqrt{m}$ and A_1 = -270.7 MPa $m^{-1/2}$.

To study the propagation of error due to perturbation of the strain field, the synthetic strain data were modified by errors of 2, 5, and 10%. Instead of uniformly applying the error across all of the gages, we introduced various combinations of the sign of the error. As shown in table 4.3, four cases were considered for each of the error levels. The perturbed strains were then reanalyzed with the spatially overdetermined algorithm, using the same initial estimates given above.

Summarized in table 4.4 are the results of the error propagation analysis. The range of values in the table represent the maximum and minimum errors over the four cases (table 4.3) at each error level (2, 5, and 10%). The last column of the table shows the average residual over all four cases for each error level. As expected, the residual at convergence increases as the error was increased. Note especially for the 5% and 10% errors the residual at convergence exceeds 0.5%, which was the value used in most portions of this dissertation as a convergence criterion.

The value of A_1 was influenced the most by the introduction of error into the strain field, as can be seen by the large errors for this term in table 4.4. This is not an unexpected result. Typically, in any collocation procedure such as the analysis used here, the highest-order term in the series expansion collects the "numerical noise" from the analysis. However, this enables us to determine the lower order parameters with greater precision. As a result, A_0 and $\theta^{(1)}$ show a lower error in table 4.4.

We conclude from this analysis that as the strain field is perturbed, the errors in the A_0 and $\theta^{(1)}$ determinations roughly scale with the error; that is, if the error in the strain field

measurement is on the order of 5%, we can expect a 5% error in A_0 and $\theta^{(1)}$. Finally, it is difficult to determine A_1 with any degree of accuracy if the strain field is perturbed. We noticed similar behavior in the static analysis of the compact specimen in Chapter 2.

REFERENCES

[4.1] Sanford, R. J., Chona, R., Fourney, W. L., and Irwin, G. R., **A Photoelastic Study of Non-Singular Stresses in Fracture Test Specimens**, NUREG/CR-2179 (ORNL/Sub.-7778/2), University of Maryland (1981).

[4.2] Chona, R., Irwin, G. R., and Sanford, R. J., "Influence of Specimen Size and Shape on the Singularity-Dominated Zone," **Fracture Mechanics: Fourteenth Symposium - Volume I: Theory and Analysis**, ASTM STP 791, J. C. Lewis and G. Sines, Eds., American Society for Testing and Materials, pp. I-3 - I-23 (1983).

[4.3] Sanford, R. J. and Link, R. E., "Local Collocation - A Hybrid Technique in Fracture Mechanics," **Proceedings - Southeast Conference on Theoretical an Applied Mechanics, SECTAM XII**, Auburn University (1984).

[4.4] ANSYS-PC/ED/LIN 4.3, Swanson Analysis Systems, Inc., Houston, Pennsylvania (1988).

[4.5] Tada, H., Paris, P., and Irwin, G. R., **The Stress Analysis of Cracks Handbook**, Del Research Corporation, Hellertown, Pennsylvania (1973).

[4.6] Hulbert, L. E., **The Numerical Solution of Two Dimensional Problems of the Theory of Elasticity**, Bulletin 198, Engineering Experiment Station, Ohio State University, Columbus, Ohio (1963).

[4.7] Berger, J. R., **An Improved Method of Boundary Collocation for the Analysis of Finite Body Opening Mode Fracture Problems**, M. S. Thesis, University of Maryland (1986).

[4.8] Rosakis, A. J., and Ravi-Chandar, K., "On Crack Tip Stress States: An Experimental Evaluation of Three-Dimensional Effects," **California Institute of Technology Technical Report FM-84-2** (1984).

[4.9] Seber, G. A. F. and Wild, C. J., **Nonlinear Regression**, Wiley and Sons, New York, NY (1989).

Table 4.1

Non-singular coefficients determined from the local collocation of the finite element data.

Coefficient	Value
A_0	139.0 MPa $m^{1/2}$
A_1	-270.7 MPa $m^{-1/2}$
A_2	-240.2 MPa $m^{-3/2}$
A_3	-334.5 MPa $m^{-5/2}$
A_4	-388.2 MPa $m^{-7/2}$
A_5	-226.1 MPa $m^{-9/2}$
B_0	-12.7 MPa
B_1	30.3 MPa m^{-1}
B_2	153.3 MPa m^{-2}
B_3	178.2 MPa m^{-3}
B_4	86.8 MPa m^{-4}
B_5	807.9 MPa m^{-5}

Table 4.2

Synthetic strain data generated for $\alpha = 0^{\circ}$ and $\alpha = 45^{\circ}$.

ε_g, $\alpha = 0^{\circ}$ ($\mu\varepsilon$)	ε_g, $\alpha = 45^{\circ}$ ($\mu\varepsilon$)
2254	-1155
1252	-1225
770	-1029
534	-846
408	-707
334	-603

Table 4.3

Sign of the errors applied to the synthetic data to study error propagation.

	Sign of the applied error					
	Gage Number					
Case	1	2	3	4	5	6
1	+	−	+	−	+	−
2	+	+	−	−	+	+
3	−	+	−	+	−	+
4	−	−	+	+	−	−

Table 4.4

Summary of the error propagation study.
All Values are in Percent.

$\mathcal{E}(\varepsilon_g)$	$\mathcal{E}(\theta)$	$\mathcal{E}(A_0)$	$\mathcal{E}(A_1)$	$\bar{r}$
2	+ 1.6 - 1.3	+ 2.2 - 2.5	+ 7.2 - 5.7	0.27
5	+ 3.9 - 3.2	+ 5.7 - 6.1	+ 20.2 - 13.4	0.65
10	+ 9.5 - 6.1	+ 10.1 - 12.3	+ 54.5 - 22.6	1.32

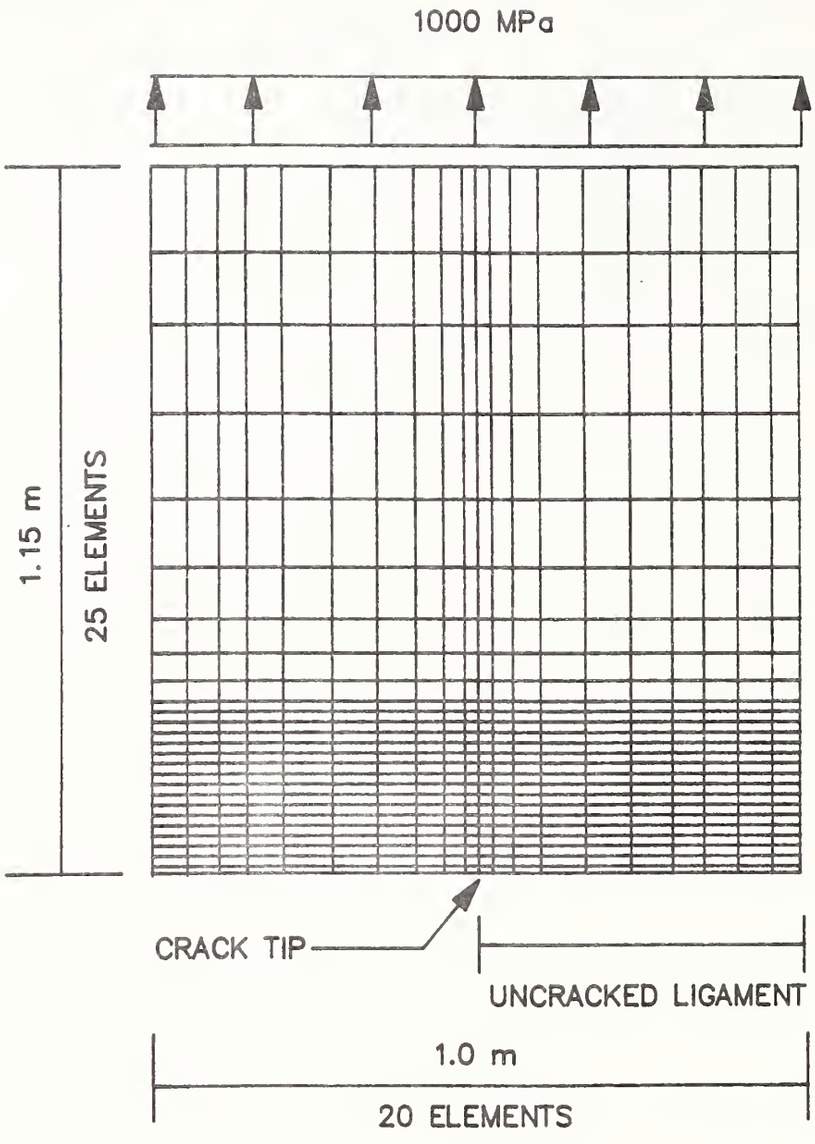

Fig. 4.1 Final geometry of the finite element mesh (only the top half of the specimen is shown).

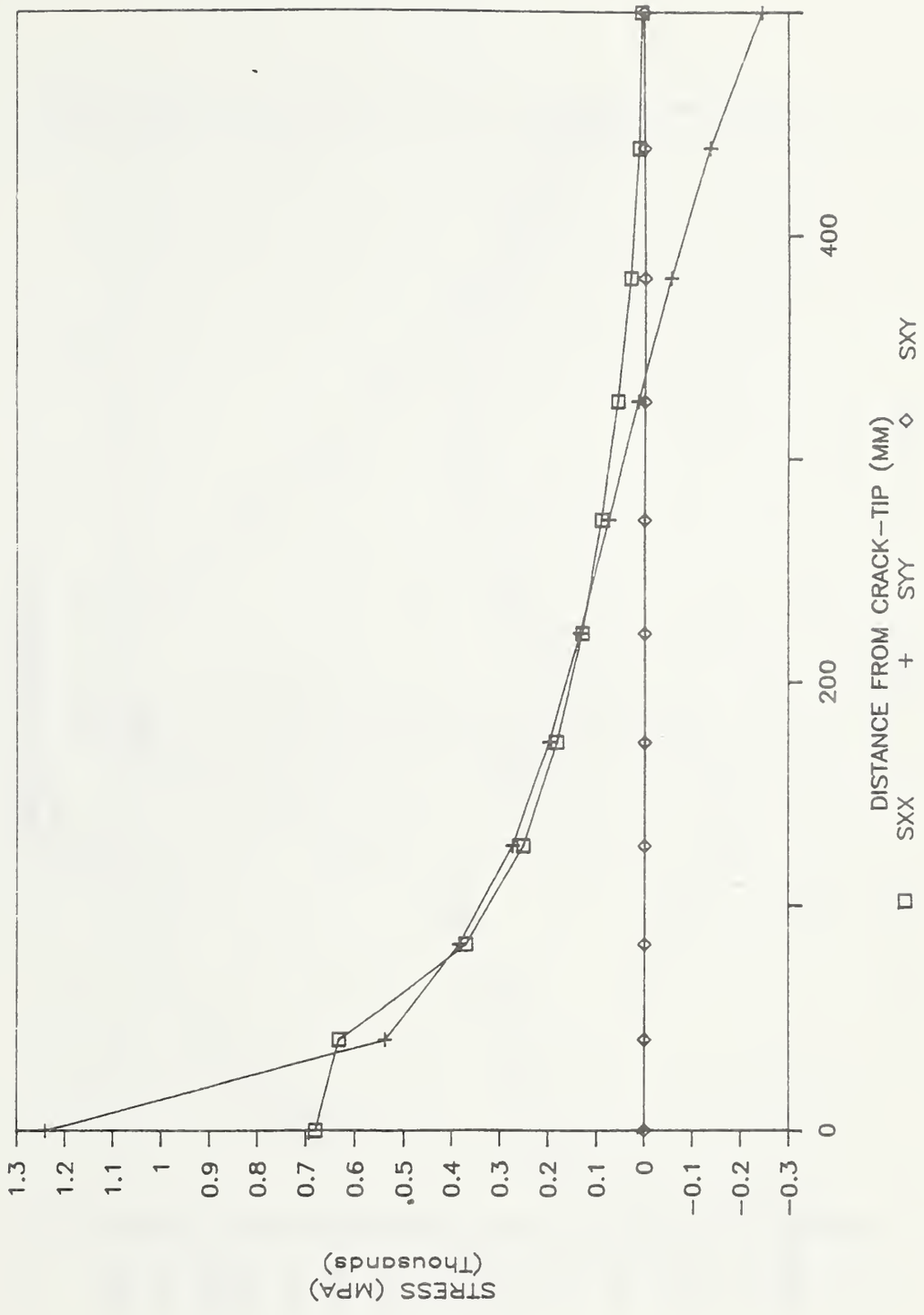

Fig. 4.2 Finite element stresses along the crack line.

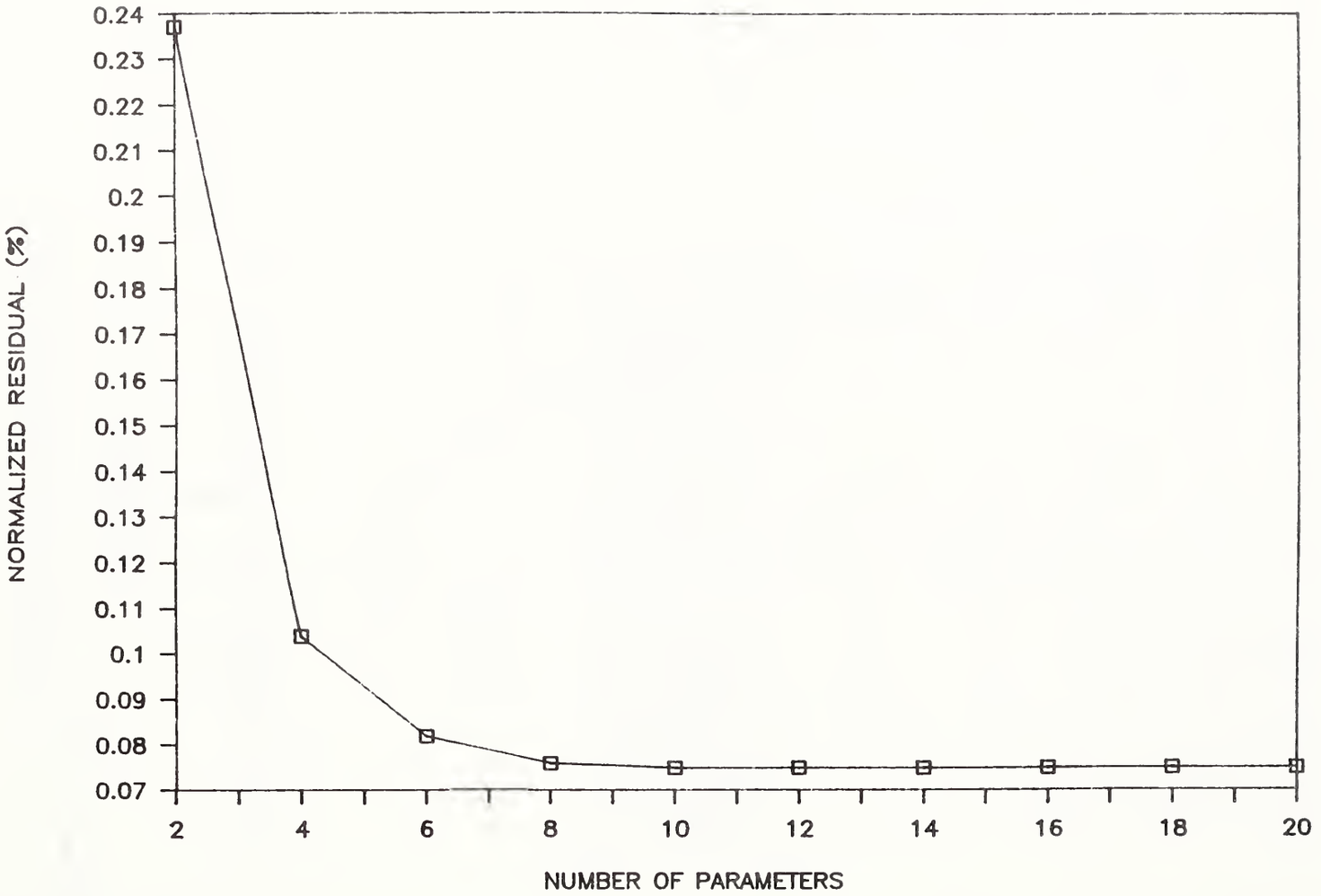

Fig. 4.3 Convergence of the local collocation of the finite element stresses.

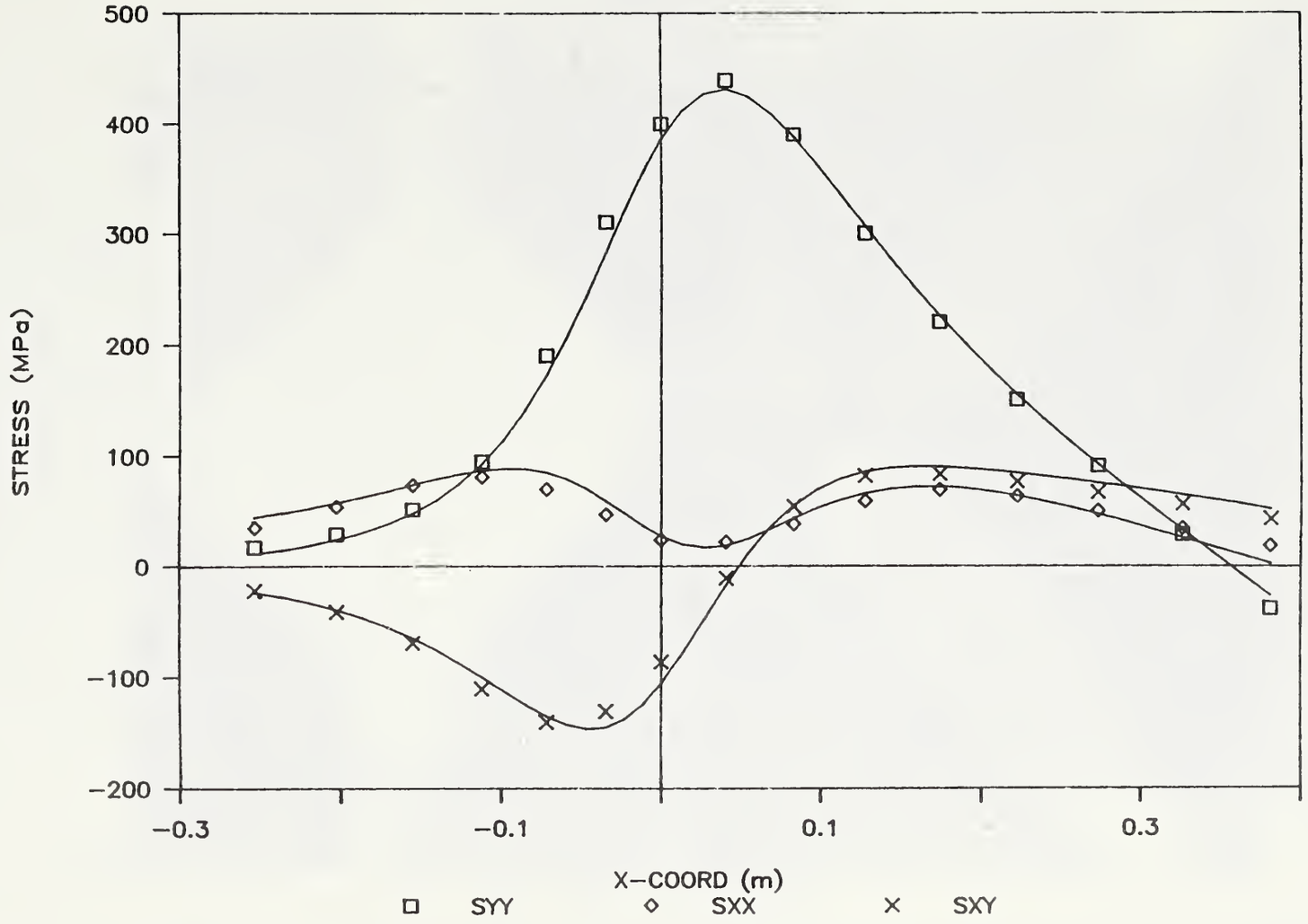

Fig. 4.4 Comparison of finite element stresses with stresses computed with a twelve parameter model. The data points are finite element values, the solid lines are the twelve parameter series values.

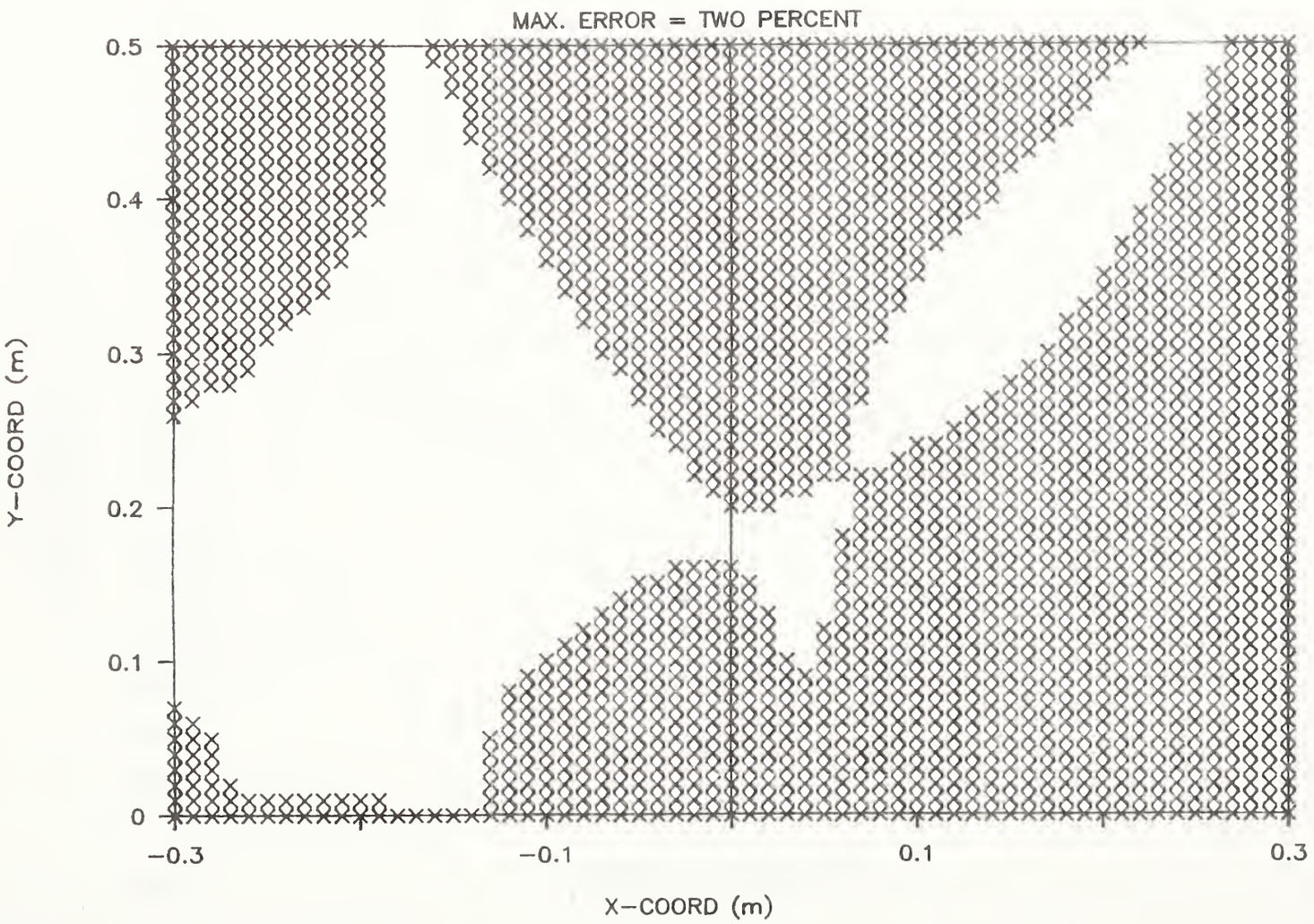

Fig. 4.5 Valid zones for the rosette strain gage using a two percent error.

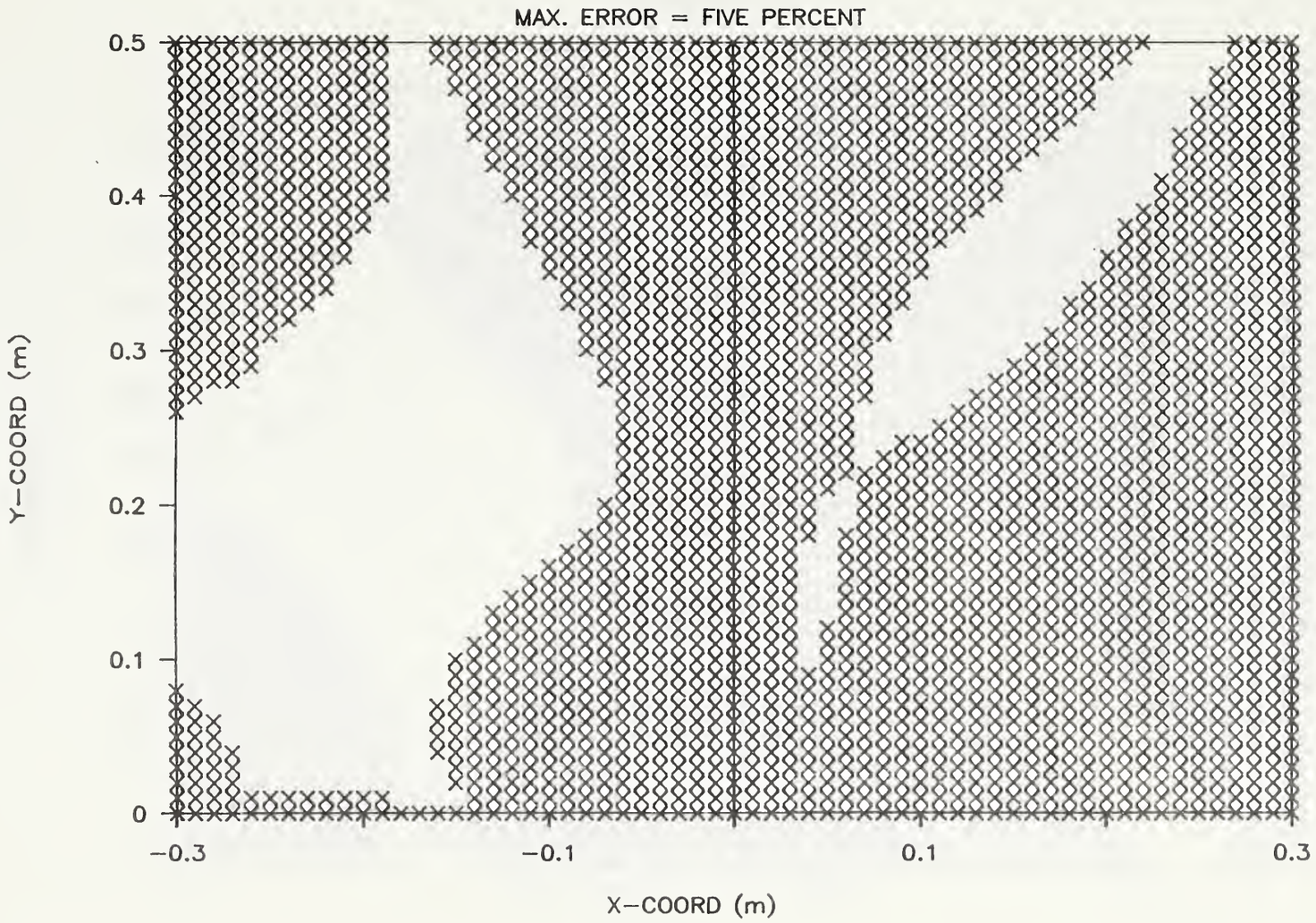

Fig. 4.6 Valid zones for the rosette strain gage using a five percent error.

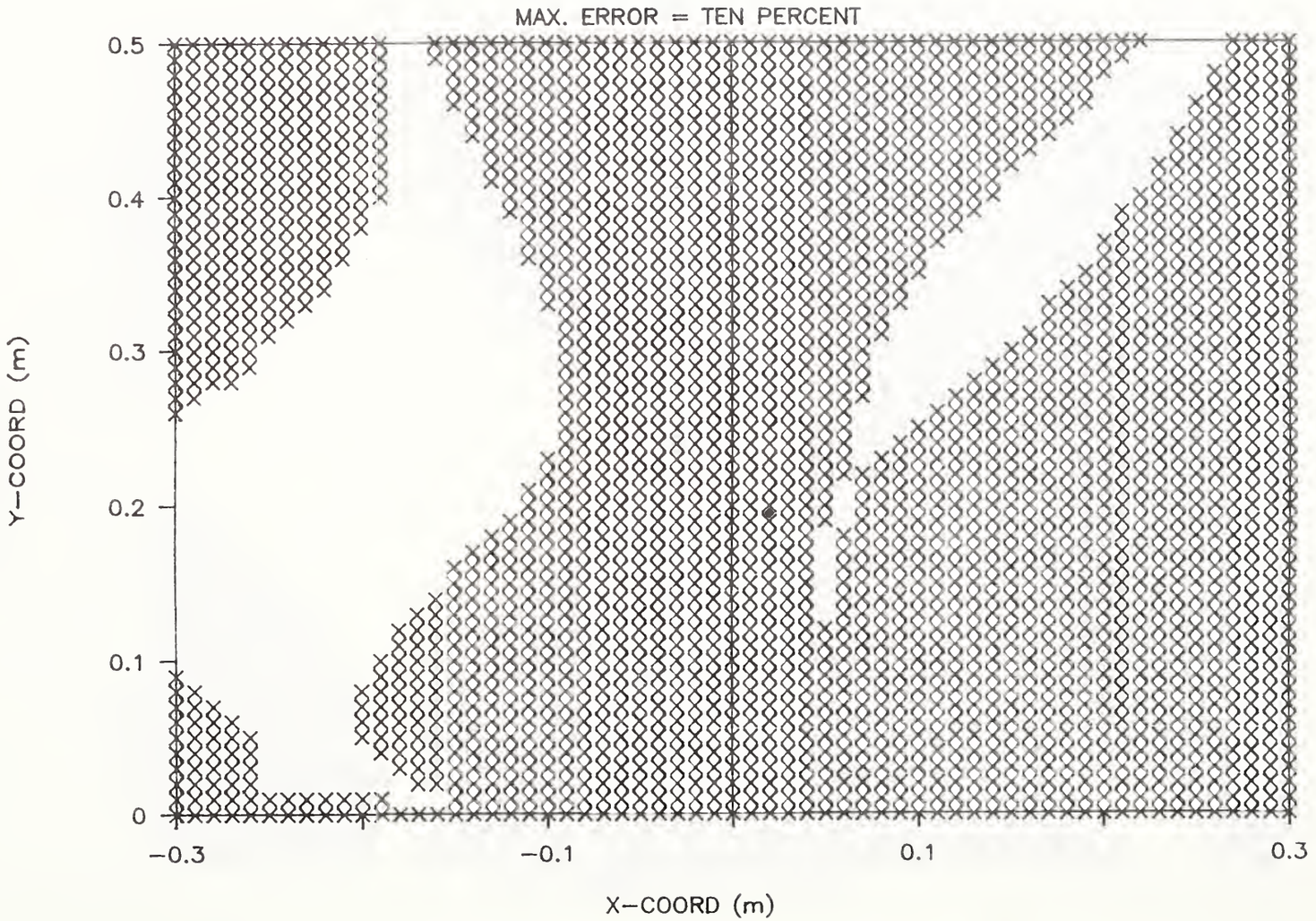

Fig. 4.7 Valid zones for the rosette strain gage using a ten percent error.

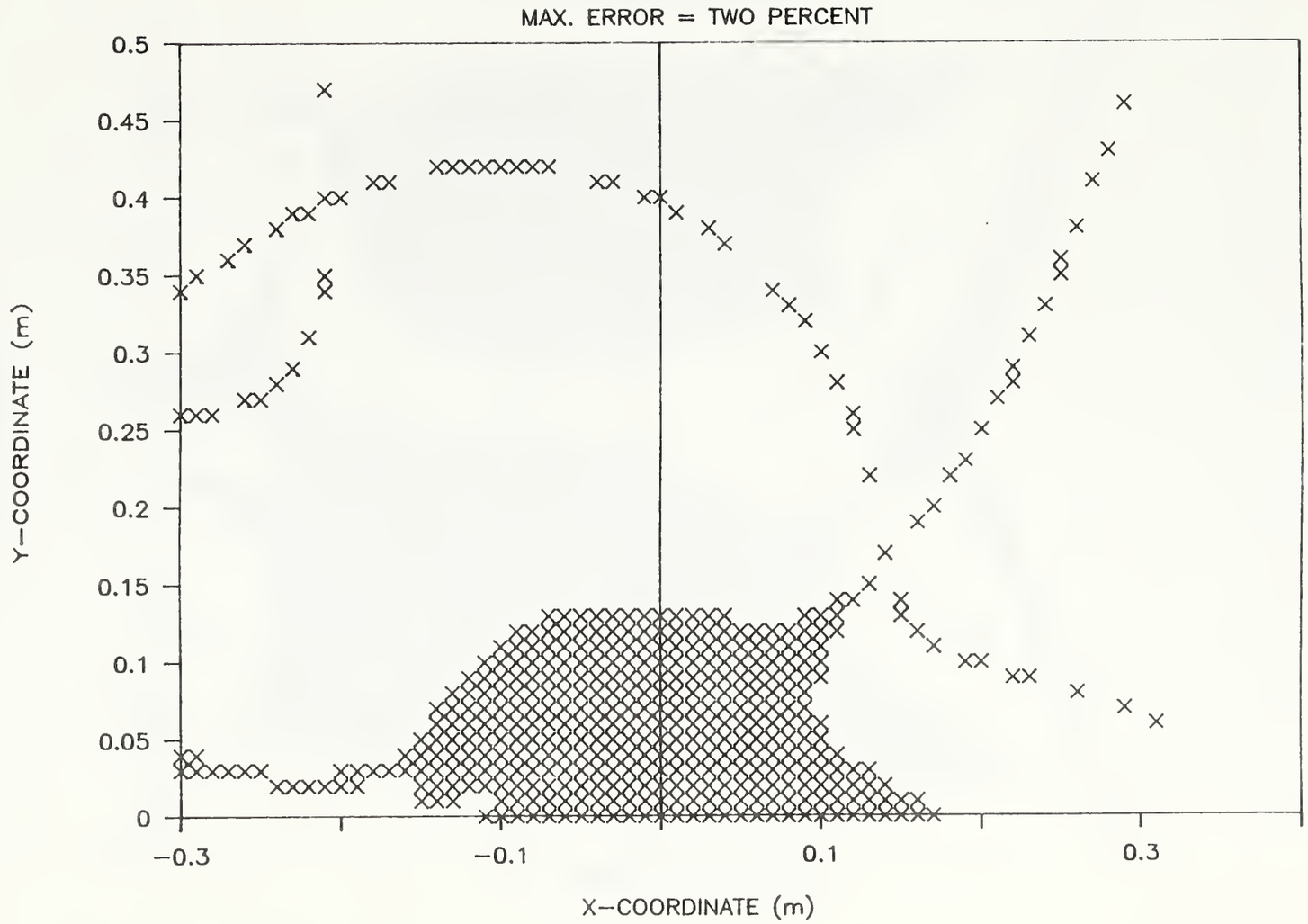

Fig. 4.8 Valid zones for the single element strain gage using a two percent error.

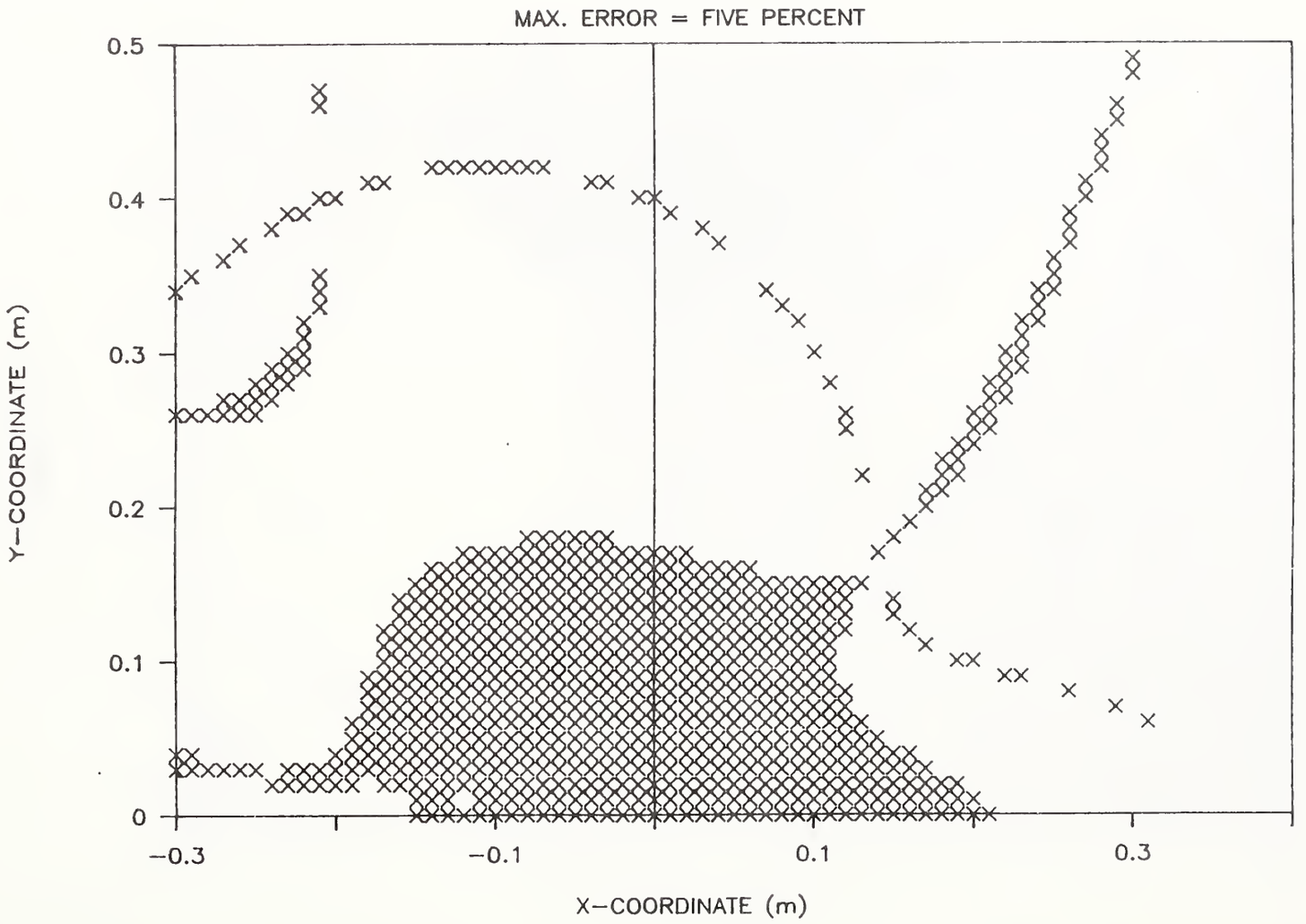

Fig. 4.9 Valid zones for the single element strain gage using a five percent error.

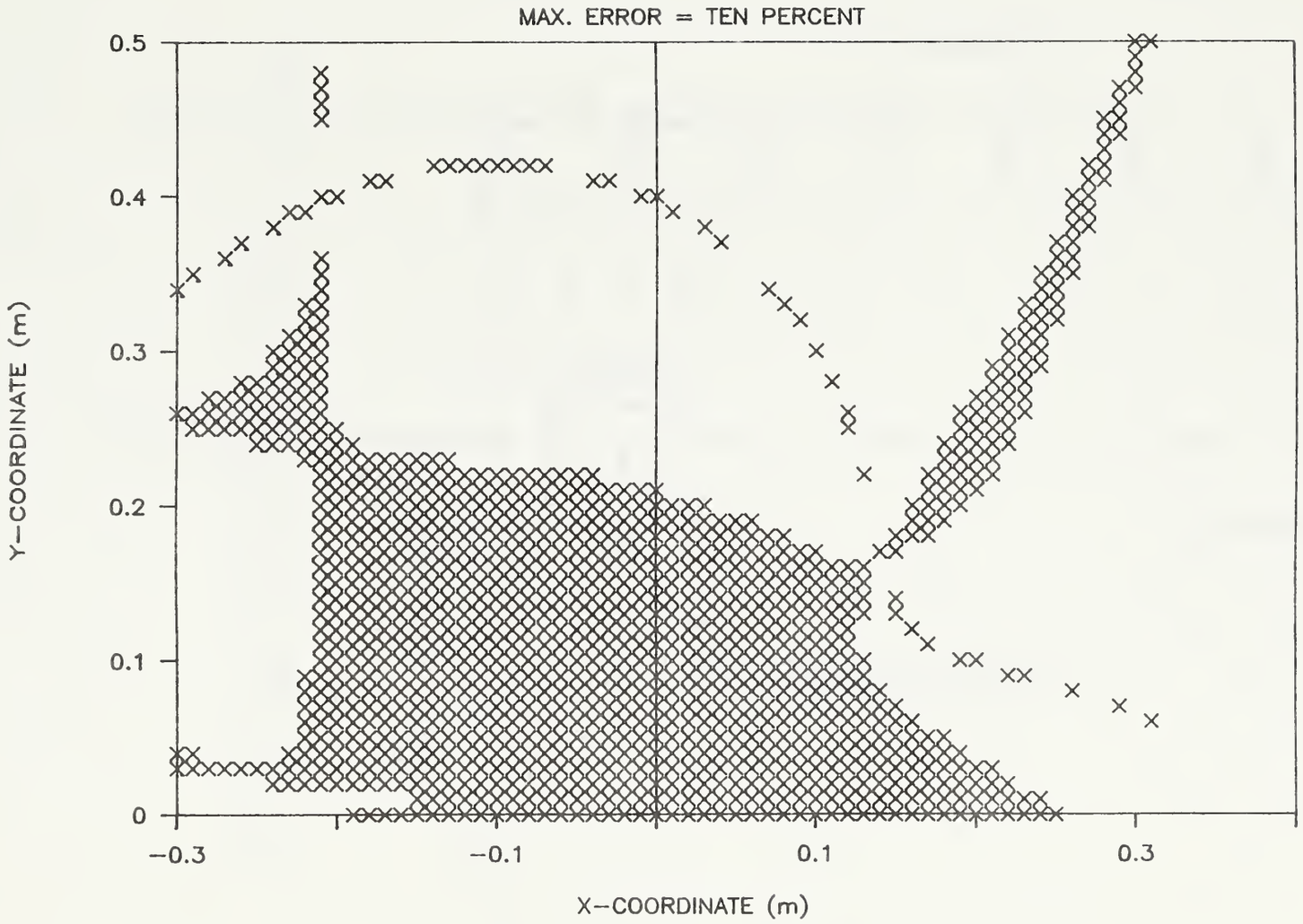

Fig. 4.10 Valid zones for the single element strain gage using a ten percent error.

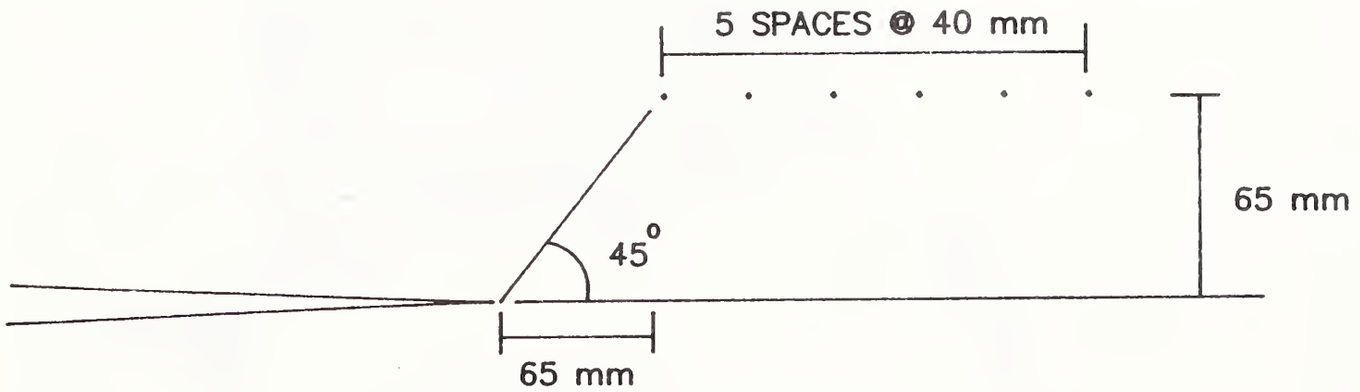

Fig. 4.11 Gage positions for generating synthetic strain data.

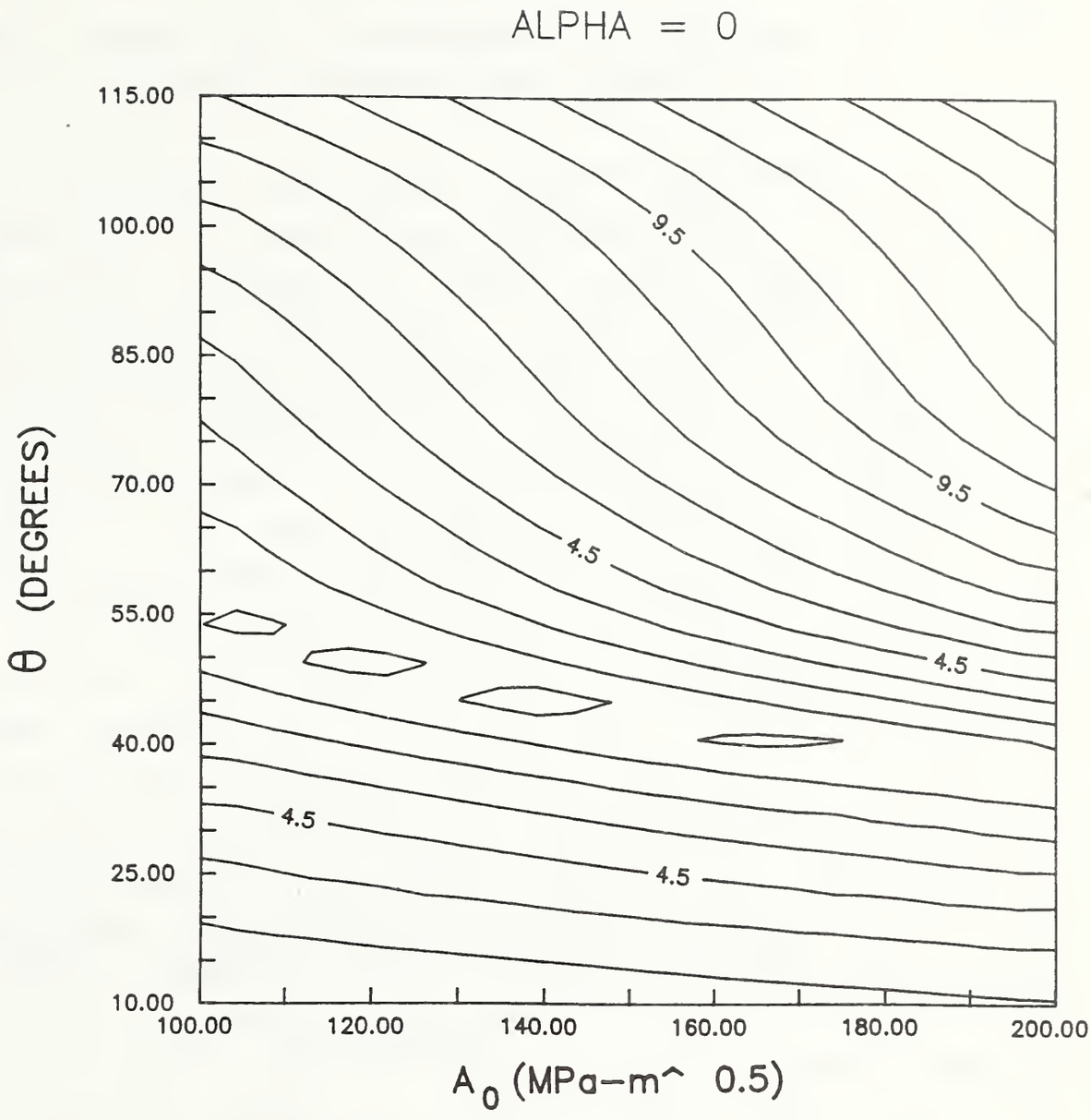

Fig. 4.12 Least squares solution space for the $\alpha = 0^{\circ}$ rosette. Contour labels are in percent.

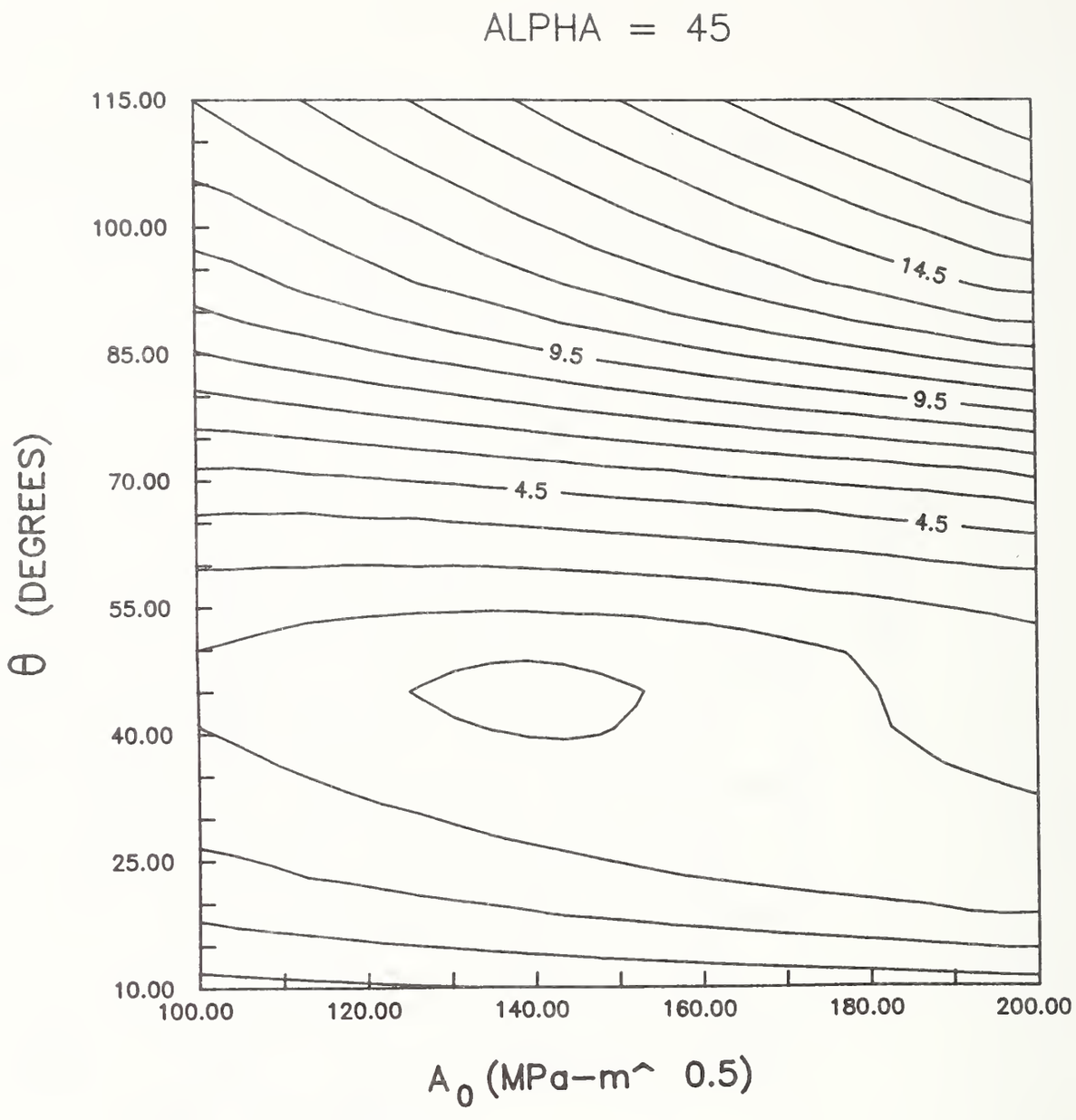

Fig. 4.13 Least squares solution space for the $\alpha = 45^{\circ}$ rosette. Contour labels are in percent.

CHAPTER 5

CRACK ARREST AND THE PROPAGATION TOUGHNESS - CRACK SPEED RELATION FOR A REACTOR-GRADE PRESSURE VESSEL STEEL

The Nuclear Regulatory Commission has conducted a test program at Oak Ridge National Laboratory (ORNL) to assess the crack-arrest behavior of reactor pressure vessel steels at relatively high temperatures. Using large-scale, wide-plate specimens in a single-edge-notch (SEN) geometry, the objective was to simulate propagation of a crack from a low-temperature, low-toughness region into an increasing temperature-toughness field. This test effectively simulates a pressurized thermal-shock scenario in a reactor pressure vessel.

The American Society of Mechanical Engineers' (ASME) Boiler and Pressure Vessel Code (BPVC) [5.1] contains provisions limiting arrest toughness, K_{Ia}, to 220 MPa $\sqrt{m}$ for light water reactor pressure-vessel steels as shown in figure 5.1. Although K_{Ia} increases with temperature for these steels, it was unknown whether or not an upper shelf occurred in K_{Ia} similar to that observed for energy absorbed in failures of Charpy specimens. The uncertainty pertaining to the existence of an upper shelf formed the basis for ASME's limiting value of K_{Ia}. The wide-plate test program was intended to provide arrest toughness data at temperatures exceeding the start of ASME's upper limit. The results were expected to verify or refute the validity of such a limit on K_{Ia}.

In this chapter the strains measured during the first crack run-arrest event in a wide-plate test of a low-upper-shelf reactor-grade steel will be analyzed using the methods developed in this dissertation. Results for the behavior of the propagation toughness with time, temperature, crack tip position and crack tip velocity will be presented. Finally, results of the strain

analysis will be compared with results from previous analyses to demonstrate the validity of the methods used here.

5.1 WIDE-PLATE SPECIMENS

The specimens used in the wide-plate test program were designed to minimize the possibility of reflected elastic stress waves from interacting with the dynamic crack propagation [5.3]. The single-edge-notch (SEN) geometry was selected to provide an increasing stress intensity with crack length. The dimensions of the wide-plate specimens are illustrated in figure 5.2.

To establish the increasing toughness field in the specimen, the left (crack opening) side of the specimen was cooled using liquid nitrogen, and the right side was heated using electrical-resistance strip heaters. The specimen was instrumented with strain gages and thermocouples using procedures developed over the duration of the testing program [5.2]. Two-element rectangular strain gage rosettes were placed on the front and back of the specimen along a line located 0.65B above the anticipated crack path, where B is the specimen thickness. Each element in the rosette was connected to an adjacent arm in a Wheatstone bridge circuit to cancel apparent strains induced by temperature changes during the loading period. The bridge amplifiers and recording instrumentation were estimated to have time resolution between 2 and 4 μs [5.5].

The specimens were loaded in tension using the 26 MN capacity testing machine at the National Institute of Standards and Technology (NIST) in Gaithersburg, Maryland. The desired temperature gradient was obtained by adjusting the power to the heaters and the flow of LN_2 to the specimen's sides. After the desired gradient was obtained, final shunt calibration of the strain gages was made, and the specimen was then loaded to failure

at a loading rate of 11 to 14 kN/s.

5.2 TEST RESULTS AND STRAIN ANALYSIS FOR A LOW-UPPER-SHELF STEEL

The second series of wide-plate tests (WP-2 series) examined a 2.25 Cr-1 Mo steel (ASTM type A387 grade 22) heat treated to produce a low-upper-shelf toughness and a high transition temperature. ORNL evaluated the mechanical properties of the material [5.4] and reported drop-weight nil-ductility transition (NDT) temperature, Charpy V-notch energy, tensile properties, initiation toughness, J-R behavior and arrest toughness. The averaged mechanical properties are given in table 5.1.

Small-specimen crack-arrest tests performed at ORNL followed the procedure in ASTM E 1221-88. The arrest data were then fit with regression analysis to an equation relating K_{Ia} to temperature,

$$K_{Ia} = 55 + 5\, e^{0.0287\ T} \ \text{MPa}\sqrt{\text{m}}, \tag{5.1}$$

where T is the temperature in °C. Equation (5.1) can also be written as

$$K_{Ia} = 34 + 36\, e^{0.02413(T\ -\ NDT)} \ \text{MPa}\sqrt{\text{m}}, \tag{5.2}$$

where NDT = 60 °C for this material.

The propagation toughness-crack speed relation was estimated to be [5.4]

$$K_{ID} = K_{Ia}(T) + A(T)\ c^2, \tag{5.3}$$

where c is the crack speed and, for $T - RT_{NDT} > -13.9$ K,

$$A(T) = (329.7 + 16.25\ (T - NDT)) \times 10^{-6}\ , \tag{5.4}$$

or, for $T - NDT \leq -13.9$ K,

$$A(T) = (121.7 + 1.296\ (T - NDT)) \times 10^{-6}. \tag{5.5}$$

Note especially the temperature dependence in eq (5.3). This changes the appearance of the K_{ID}-c curve from that shown in

figure 1.1 to the three-dimensional illustration of the K_{ID}-c-T surface that is shown in figure 5.3.

The geometry of the sixth specimen in the WP-2 series, WP-2.6, is shown in figure 5.4. The back of the specimen was instrumented with strain gage rosettes oriented at $\alpha = 45^{\circ}$ to the crack plane to eliminate the contribution of B_0 to the gage response as demonstrated in previous chapters and in [5.6]. The specimen was loaded until initiation occurred at 19.33 MN. The crack propagated in a series of eight run-arrest events followed by a final tearing fracture. Typical strain gage traces from the 45° rosettes recorded during the run-arrest events are shown in figure 5.5. Of the eight rosettes which were oriented at $\alpha = 45^{\circ}$ (gage numbers 13 to 20), only seven gages were useful for the analysis presented here, since one arm of gage 15 failed before providing meaningful output. Finally, the temperature gradient established from thermocouple data immediately before fracture of the specimen is shown in figure 5.6.

The strain records for this test were analyzed using the spatially overdetermined method presented in Section 3.3. Attention was focused on the period when the crack initiated in rapid fracture to the first arrest. The behavior of the crack following the first arrest was not studied.

Before beginning the analysis of the strain records, gages were identified which satisfied the requirements given in Chapter 4 for the extent of validity of the three-parameter model used. As the crack propagated into the specimen the "window" of gages usable in the overdetermined analysis changed. Table 5.2 lists which gages could be used as the crack extended.

The strain data were analyzed from $0 \leq t \leq 0.60$ ms in 0.01 ms increments. Since the crack velocity was not known *a priori*, as required to employ the dynamic strain field equations, the first analysis was performed with the static rosette expressions for $\varepsilon_{y'y'}-\varepsilon_{x'x'}$ given in Section 2.1.2. Results obtained from the

static analysis yield the crack tip position as a function of time as shown in figure 5.7. The continuous curve through the data points was obtained using a combination of smoothing techniques and least squares analysis.

The smoothed data for a(t) were used as input for an overdetermined analysis with the crack position prescribed. Although this did not drastically change the values for A_0 and A_1 determined in the initial analysis (with crack position unknown), it did smooth out the behavior of A_0 and A_1 as functions of time. Results from this static strain field analysis for the variation of propagation toughness, K_{ID}, with time and position are shown in figures 5.8 and 5.9. The toughness values appearing in these figures and those reported later have been modified to account for the presence of side grooves. The correction factor for the side grooves is defined as

$$C_g = \sqrt{B/B_n}\ , \qquad (5.6)$$

where B is the gross section thickness and B_n is the reduced section thickness at the side-grooved region. For the WP-2.6 plate, B = 152.4 mm, B_n = 113.9 mm, and C_g = 1.16.

The results of the overdetermined analysis at t = 0 with the static representation of the strain field provide an opportunity to evaluate the initiation toughness, K_{Iq}. The initiation toughness determined from the strain analysis with the side groove correction was K_{Iq} = 202.5 MPa $\sqrt{m}$. It is interesting to compare this value with K_{Iq} determined from the load at initiation (19.33 MN). Following [5.7],

$$K = \sigma \sqrt{\pi\, a_{eff}}\ F(a_{eff}/w) + K_B, \qquad (5.7)$$

where σ is the remote applied stress, a_{eff} is the plasticity-corrected crack length, F(a/w) is a geometric shape function, and K_B is the stress intensity generated by the temperature-induced bending. For the WP-2.6 plate geometry, the initiation toughness value is then K_{Iq} = 196.6 MPa $\sqrt{m}$. This

result agrees to within three percent of the K_{Iq} determined from the strain analysis.

Using the smoothed data for a(t), we calculated the velocities, c(t), shown in figure 5.10. Although these results can be considered preliminary until the analysis using the dynamic equations is presented, there are several features worth noting on figure 5.10. The maximum velocity of 729 m/s is attained at 0.11 ms. It is likely that the crack propagated at an even greater velocity immediately following initiation. However, we have no reliable velocity data for this period for the reasons discussed below. The crack speed then drops as the arrest is approached. After 0.37 ms, the velocity maintains a near constant value of approximately 50 m/s. The final interpretation of the time of arrest and a discussion of the apparent crack velocity after arrest are deferred until after the presentation of the analysis using the dynamic representation of the strain field.

Reviewing the curves for a(t), figure 5.7, and c(t), figure 5.10, the behavior of the crack before $t < 0.1$ ms deserves attention. First, there is an apparent discrepancy for the crack length at initiation determined from figure 5.7 and the fracture surface shown in figure 5.11. Second, the motion of the crack after initiation is not rapid; that is, rapid propagation is not occurring until approximately 0.1 ms after initiation, when this behavior is expected almost immediately. Each of these apparent discrepancies are addressed in turn.

To examine the crack length discrepancy, it is useful to recall the Irwin approximation to the plastic zone and its effect on the apparent position of the crack tip [5.8]. The radius of the plastic zone in plane strain is

$$r_y = \frac{1}{6\pi} (K_I / \sigma_{ys})^2, \qquad (5.8)$$

where σ_{ys} is the yield stress. Under the influence of such a plastic zone the effective position of the crack tip is shifted by

r_y for the elastic stress distributions of linear elastic fracture mechanics,

$$a_{eff} = a_{phys} + r_y , \tag{5.10}$$

where a_{eff} is the effective crack tip position and a_{phys} is the physical crack tip position.

Now, in the strain analysis we are determining crack tip position through the use of linear elastic fracture mechanics expressions for the strain field. Therefore, if a plastic zone is present in the specimen the crack tip position determined from the analysis is actually the effective crack tip position and not the physical crack tip position. Therefore, crack tip positions determined at initiation where the plastic zone was large will show significant differences with the physical crack tip position until the crack is propagating in cleavage with the associated shrinkage of the plastic zone.

To quantify the above discussion, we can calculate a plastic zone diameter at initiation using K_{Iq} = 202.5 MPa $\sqrt{m}$ and an appropriate value of the yield stress. From the NIST thermocouple data, the crack tip temperature at initiation was 65 °C. The ORNL data on tensile properties gives $\sigma_{ys} \cong$ 270 MPa at this temperature. The value of r_y is then 29.8 mm. The effective crack tip position determined from the strain analysis was 243.2 mm. Therefore, the physical crack length is a_{phys} = 213.4 mm, which is within five percent of the measured crack length of 224 mm before initiation.

The second issue concerning the "lag" in when rapid propagation occurs can be examined by considering two physical phenomena that occur simultaneously: (1) propagation of the crack across the plastic zone generated before initiation and (2) the generation of elastic waves at initiation and their transit times to the gages. Calculating the time for the crack to propagate across the plastic zone requires velocity values immediately

following initiation. Although precise values for the velocity are not available from figure 5.10 for this period, a reasonable estimate is from 100 to 500 m/s. Using the plastic zone radius at initiation calculated above, 29.8 mm, the time required to propagate across the plastic zone diameter ranges from 0.30 ms for c = 100 m/s to 0.06 ms for c = 500 m/s. Until the crack has propagated through the plastic zone, reliable calculations of the physical crack tip position cannot be made.

To evaluate the delay due to elastic wave propagation, consider the distance to the most remote gage used in the analysis for $t < 0.10$ ms, gage 18, as 218.0 mm. Since the shear wave generated at initiation carries the most significant information about the dynamic crack growth, we calculate the transit time to gage 18 of this wave. For steels, c_s = 3220 m/s, and the transit time is 0.068 ms. Since at least two transit times are probably required before the gage is truly responding to the dynamic crack growth, the data for $t < 0.10$ ms are not representative of the dynamic crack propagation. Based on both of these considerations, the data analysis using the dynamic representation of the strain field will only be performed for $t \geq 0.10$ ms.

Using the velocity data shown in figure 5.10 as input, the strain analysis in $0.10 \leq t \leq 0.60$ ms was repeated using the dynamic equations presented in Section 3.1.2. It was anticipated that the crack tip position determined using the dynamic representation would not differ significantly from the position determined using the static representation, since the spatial distribution of strain predicted by the two equations is similar. However, a change in the value of the propagation toughness (the scalar multiplier for the strain field) was anticipated. As indicated on the a(t) curve in figure 5.12, the data points are essentially identical when using either of the two formulations. Consequently the velocity data did not need to be readjusted.

Data for $t > 0.40$ ms are not shown on figure 5.12 because of

the low crack velocity associated with crack growth during this time interval ($c < 50$ m/s). The dynamic strain field representation does approach the corresponding static representation in the limit as $c \rightarrow 0$ is approached. However, examining the dynamic field equations for strain, the limit must be taken carefully, since both the β_j functions and the velocity-transformed coordinates r_j, θ_j are functions of the crack speed. As a result, these equations produce numerical instabilities at low crack speeds when using finite precision arithmetic. To avoid these instabilities, for velocities below 50 m/s the static representation should be used. The absolute value of this "cutoff" velocity is not too critical, since, as discussed below, the difference in K_{ID} values computed using either formulation at low velocities is small.

The smoothed curve for a(t) was used to prescribe the crack tip position for the next analysis, following the same procedure developed previously with the static strain field representation. Results for propagation toughness with time, temperature and position are shown in figures 5.13-5.15. A comparison of these figures with figures 5.8 and 5.9 shows that predictions based on the static representation are the same as those determined with the dynamic representation. However, the magnitude of K_{ID} changes depending on the instantaneous value of the crack velocity. As shown in figure 5.16, for crack speeds less than 300 m/s, the difference in calculating K_{ID} by the dynamic or static equations is negligible (less than 1% difference). The difference then becomes larger as velocity increases. For this analysis of WP-2.6, the maximum difference was 5.5% at $c = 729$ m/s.

In [5.3], an approximate correction factor is used to facilitate scaling K values obtained from a static analysis to K values for running cracks. The correction factor is

$$K_{DYNAMIC} = K_{STATIC} \sqrt{1 - (c/c_R)} , \qquad (5.11)$$

where c_R is the Rayleigh wave speed (c_R = 2980 m/s in steels). The ratio, $K_{DYNAMIC}/K_{STATIC}$, is presented in figure 5.16 as a function of c/c_R and is compared with the results from the strain analysis of WP-2.6. Figure 5.16 indicates some difference in actual values predicted by eq (5.11) when compared to the strain analysis. However, the overall trend with increasing velocity is similar.

To ascertain when arrest occurred, it is useful to calculate crack tip accelerations from the c(t) data in figure 5.10. As shown in figure 5.17, the accelerations are largest after initiation and then gradually decrease as the crack arrests. Since a necessary condition for crack arrest is for the acceleration to be zero, figure 5.17 indicates arrest occurring near t = 0.38 ms. However, the behavior of a(t) and c(t) near t = 0.38 ms must be reviewed to determine if arrest did indeed occur.

Examining figure 5.10 at t = 0.38 ms, we note that the velocity is constant at c ≅ 50 m/s. This behavior is consistent with an argument that the physical crack has arrested and that the "effective" crack is extending due to the expansion of the plastic zone at arrest. We can estimate this growth rate through a simple differentiation of eq (5.8). For a first approximation we assume that the time rate of change of the yield stress and shear modulus is small during the time of interest at arrest (distinctly different than if we were looking at cleavage-crack propagation where such approximations would be dubious). After making these assumptions and substituting $K = A_0\sqrt{2\pi}$, we obtain

$$6 \dot{r}_y = \left[\frac{2\mu}{\pi f_0 \sigma_{YS}} \right]^2 \dot{\varepsilon}_g \dot{\varepsilon}_g . \qquad (5.12)$$

Using values for gage 16 obtained at the time of arrest, t = 0.38

ms, $\dot{r}_y$ = 47.8 m/s. This is in good agreement with the results of the strain analysis and is equivalent to an extension of the effective crack tip at the same velocity. Slightly higher values for the growth of the elastic-plastic boundary at arrest were found in [5.5]. However, our result is within the estimated error reported in [5.5].

Examination of the velocity data suggests that the crack arrested at t = 0.38 ms followed by growth of the plastic zone. It is unlikely that the plastic zone ever reaches its full static equilibrium size, since a second initiation was estimated to occur at t = 1.0 ms [5.4], and in [5.5] it was estimated that 4 to 5 ms are required to fully develop the equilibrium plastic zone in a transition from a running to an arrested crack.

One further comment should be made here concerning plasticity effects for a running crack. In [5.5], the authors found that the velocity of the elastic-plastic boundary was weakly dependent on the applied stress intensity. Furthermore, an upper limit for the plastic zone velocity was found to be approximately 250 m/s. This fact implies that there is insufficient time for the plastic zone to develop for a propagating cleavage crack running in excess of 250 m/s. Similar conclusions were obtained in [5.10] following a dislocation model of fracture.

As a final check on the hypothesis that arrest occurred at t = 0.38 ms, we note in figure 5.12 at t = 0.38 ms that the crack length is a = 360.4 mm. An examination of the fracture surface characteristics presented in figure 5.11 indicates that the crack front at the first arrest is curved significantly. The crack front intersects the front surface at 320 mm, the back surface (location of the $\alpha = 45^{\circ}$ gages) at 300 mm, and has a maximum extension of 390 mm. The result for the arrest position a_a = 360 mm obtained from the strain analysis represents an apparent crack tip position for a two-dimensional analysis. Although significant

progress has been made in formulating an approach to the three-dimensional problem [5.11, 5.12], a full three-dimensional treatment will not be considered here.

Based on the above observations and discussion, we conclude that arrest occurred at t_a = 0.38 ms with a crack length at arrest of a_a = 360.4 mm. From the temperature-position data given in figure 5.6, the temperature at arrest was determined as T_a = 103.6 °C. From the results of $K_{ID}(t)$ shown in figure 5.14, the arrest toughness was $K_{Ia} = K_{ID}(0.38 \text{ ms})$ = 230.0 MPa $\sqrt{m}$. For purposes of comparison, in [5.4] the arrest was determined to occur at t_a = 0.31 ms, a_a = 340.0 mm, K_{Ia} = 253.0 MPa $\sqrt{m}$, and T_a = 97.6 °C. These results are summarized in table 5.3.

The arrest toughness determined from the strain analysis can also be compared with the ASME curve and ORNL's small specimen data. The ASME limits arrest toughness at T_a = 103.6°C to 85 MPa $\sqrt{m}$, clearly an extremely conservative value based on the arrest toughness obtained here. From eq (5.1), an estimate of the arrest toughness from ORNL's small specimen data is K_{Ia} = 184 MPa $\sqrt{m}$. This lower value of the arrest toughness can be attributed to both the difficulty in translating small-scale test data to large structures as well as the inherent problems with the ASTM crack-arrest standard discussed in the introduction to this report.

Having evaluated the arrest conditions (toughness, time, temperature, and position), we can now focus on the relationship between propagation toughness and crack velocity. Shown in figure 5.18, the characteristic shape of this curve is not of the gamma (Γ) shape described in Chapter 1. However, by plotting the propagation toughness-crack velocity relation in this manner we have ignored the temperature dependence in the constitutive relation. We know that arrest toughnesses increase with increasing temperature from the data in the wide-plate test series. This behavior is indicated in the schematic K_{ID}-c-T

surface shown in figure 5.3. Since we are following a contour on this surface for this test, the effect is to produce additional curvature for the lower segment of the K_{ID} - c curve when we ignore the temperature dependence. The imposition of a temperature gradient forces us to use the three-dimensional constitutive surface shown in figure 5.19 to properly interpret the crack propagation.

REFERENCES

[5.1] **Boiler and Pressure Vessel Code**, Section XI, American Society of Mechanical Engineers.

[5.2] deWit, R., Low, S. R. III, and Fields, R. J., "Wide Plate Crack Arrest Testing: Evolution of Experimental Procedures," **Fracture Mechanics: Nineteenth Symposium**, ASTM STP 969, T. A. Cruse, Ed., American Society for Testing and Materials, Philadelphia, pp. 679-690 (1988).

[5.3] Naus, D. J., et al., **Crack-Arrest Behavior in SEN Wide Plates of Quenched and Tempered a 533 Grade B Steel Tested Under Nonisothermal Conditions**, NUREG/CR-4930 (ORNL 6388), Martin Marietta Energy Systems, Inc., Oak Ridge National Laboratory, August, 1987.

[5.4] Naus, D. J., et al., **Crack-Arrest Behavior in SEN Wide Plates of Low-Upper-Shelf Base Metal Tested Under Nonisothermal Conditions: WP-2 Series**, NUREG/CR-5451, Martin Marietta Energy Systems, Inc., Oak Ridge National Laboratory (Preliminary Draft).

[5.5] Fields, R. J., and deWit, R., "Plastic Zone Formation Around an Arresting Crack," **International Journal of Fracture**, Vol. 42, pp. 231-238 (1990).

[5.6] Dally, J. W., and Sanford, R. J., "Strain Gage Methods for Measuring the Opening Mode Stress Intensity Factor, K_I," **Experimental Mechanics**, Vol. 27, No. 4, pp. 381-388 (1987).

[5.7] deWit, R., et al., **Wide Plate Crack Arrest Testing: A Description and Discussion of the First Two Wide Plate Tests and the Results of Six, Full Thickness, Bend Bar Tests**, NBSIR 87-3629,

National Institute of Standards and Technology, Gaithersburg, Maryland (1987).

[5.8] Irwin, G. R., "Plastic Zone Near a Crack and Fracture Toughness," **Proceedings of the Seventh Sagamore Ordinance Material Research Conference**, Report No. MeTE 661-611/F, Syracuse University Research Institute, pp. IV-63 (1960).

[5.9] Freund, L. B., "Crack Propagation in an Elastic Solid Subjected to General Loading - III. Stress Wave Loading," **Journal of the Mechanics and Physics of Solids**, Vol. 21, pp. 47-61 (1973).

[5.10] Lin, I.-H., and Thompson, R. M., "Relatavistic BCS-OHR Model," **International Conference on Fracture Mechanics VII**, Houston, Texas (1988).

[5.11] Solecki, J. S., and Swedlow, J. L., "On the Three-Dimensional Implications of LEFM: Finite Element Analysis of Straight and Curved Through-Cracks in a Plate," **Fracture Mechanics: Sixteenth Symposium**, ASTM STP 868, M. F. Kanninen and A. T. Hopper, Eds., American Society for Testing and Materials, Philadelphia, Pennsylvania, pp. 535-553 (1985).

[5.12] Swedlow, J. L., "Three-Dimensions Versus Two-Dimensions in Fracture Mechanics," **Fracture Mechanics: Nineteenth Symposium**, ASTM STP 969, T. A. Cruse, Ed., American Society for Testing and Materials, Philadelphia, Pennsylvania, pp. 88-98 (1988).

[5.13] Irwin, G. R., Kobayashi, T., Fourney, W.L., Metcalf, J. T., and Dally, J. W., "Photoelastic Studies of Crack Propagation and Arrest in Polymers and 4340 Steel," **U.S. NRC Report**, NUREG/CR-0542, University of Maryland (1978).

[5.14] Schwartz, C. W. and Bass, B. R., "Crack Speed Relations Inferred from Large SEN Specimens of A533B Steel," **Engineering Fracture Mechanics**, Vol. 34, No. 5/6, pp. 1209-1223 (1989).

Table 5.1
Summary of the mechanical properties of the WP-2 material at room temperature.

Charpy V-Notch Energy at the Nil-Ductility Temperature	18.3 J
Ultimate Tensile Strength	596 MPa
Yield Strength	315 MPa
Reduction in Area	50 %
Elongation	25 %

Table 5.2
Gages available for use in the strain analysis of WP-2.6 with changing crack length.

Crack Length, a (mm)	Usable Gages*
$a_0 \leq a \leq 249$	13 - 17
$250 \leq a \leq 289$	13 - 18
$290 \leq a \leq 329$	13 - 19
$330 \leq a \leq a_a$	13 - 20

*Gage 15 not used

Table 5.3
Comparison of the arrest conditions for WP-2.6.

	This Analysis	Ref. [5.4]
K_{Ia} (Mpa $\sqrt{m}$)	230.0	253.0
a_a (mm)	360.4	340.0
T_a (^{o}C)	103.6	97.6
t_a (ms)	0.38	0.31

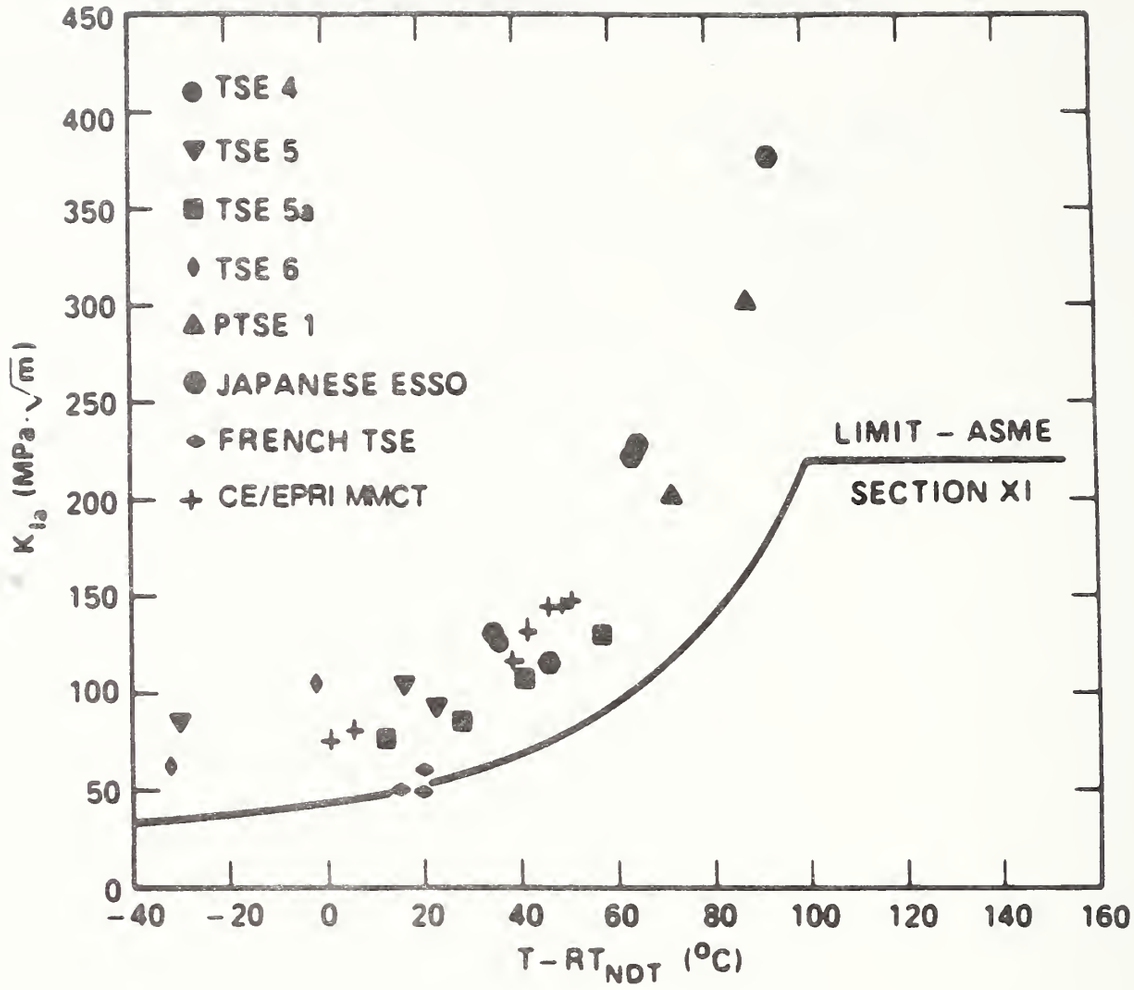

Fig. 5.1 Crack arrest toughness as a function of temperature for a nuclear pressure vessel steel (from [5.3]).

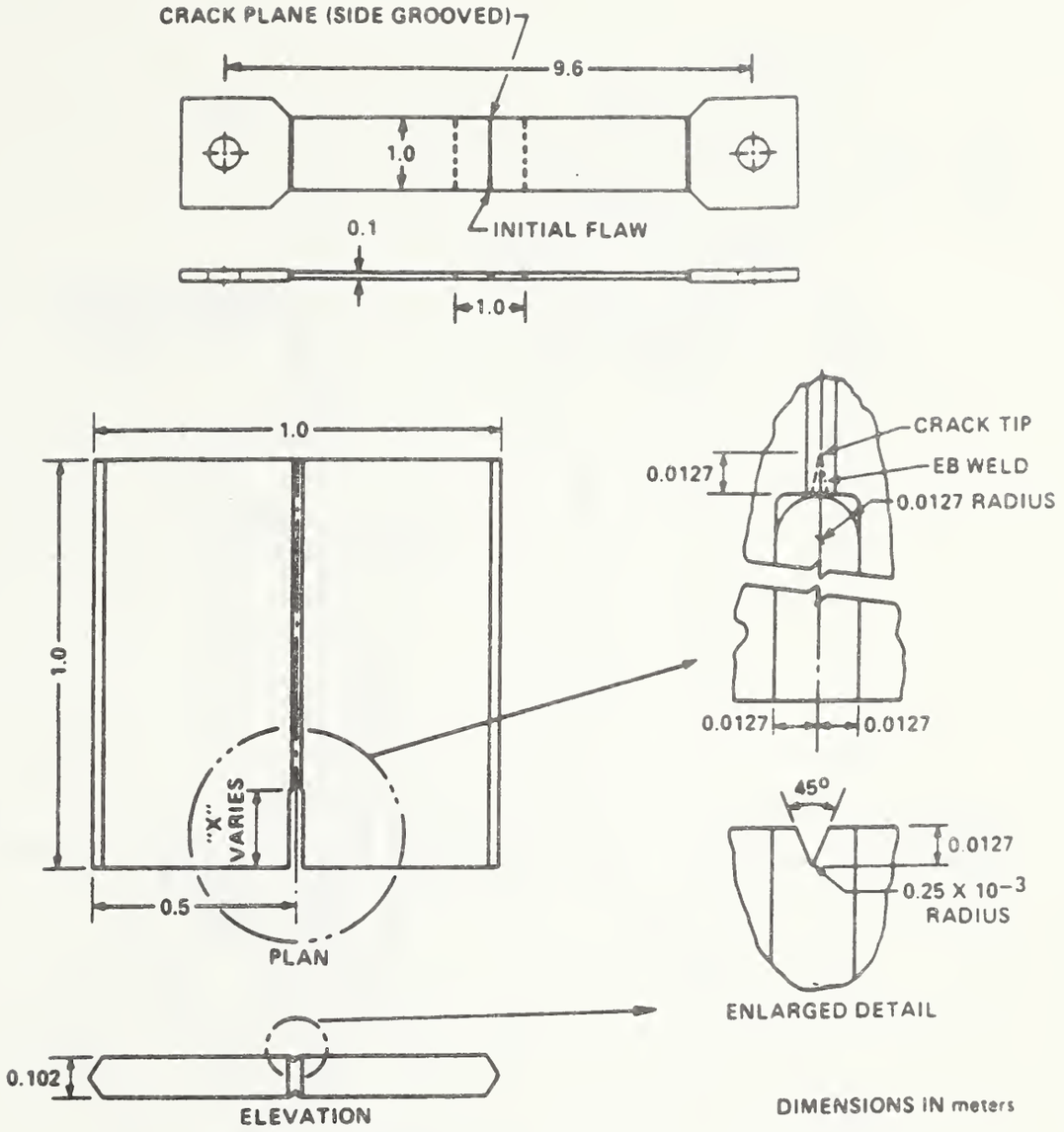

Fig. 5.2 Geometry of the wide plate specimen (from [5.3]).

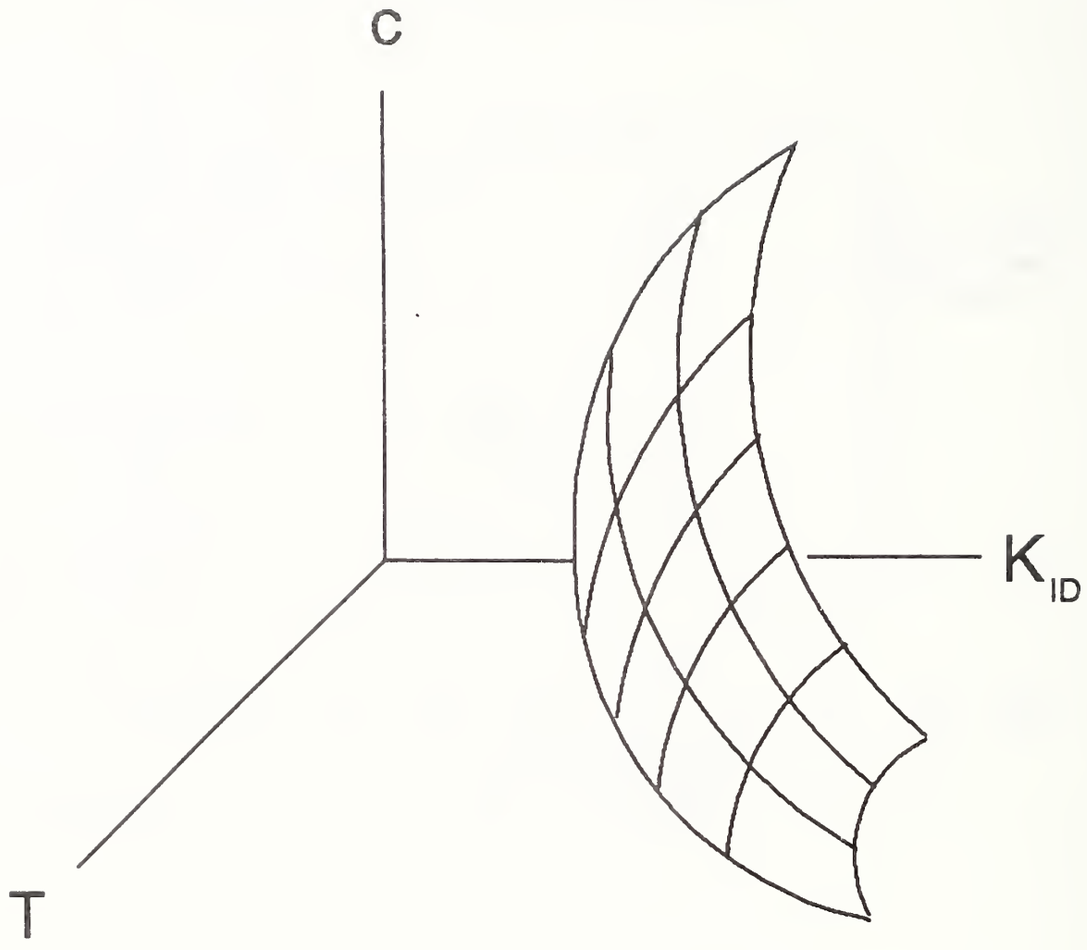

Fig. 5.3 Schematic representation of the propagation toughness, crack velocity, temperature surface.

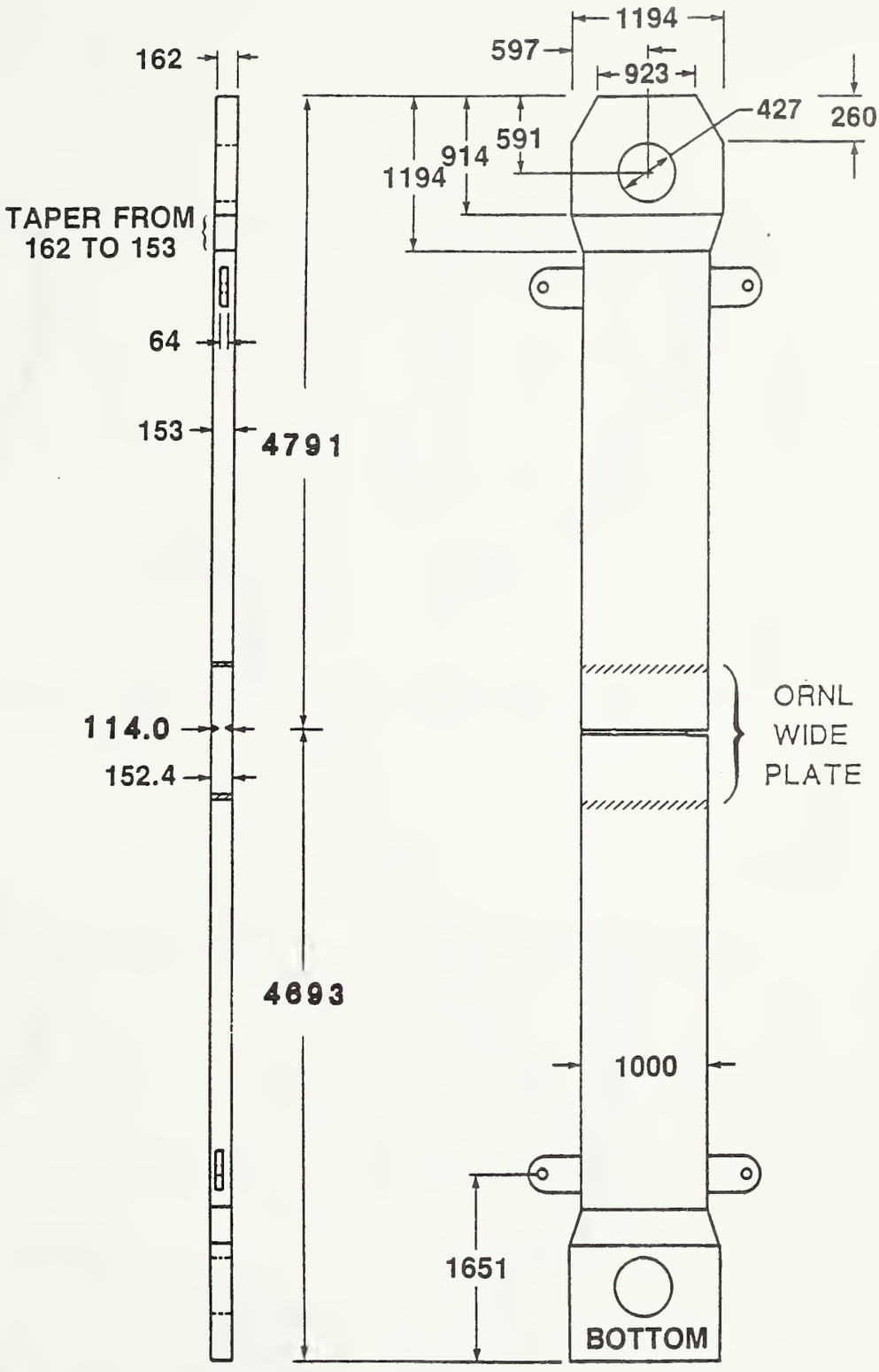

Fig. 5.4 Geometry of the WP-2.6 specimen (from [5.4]).

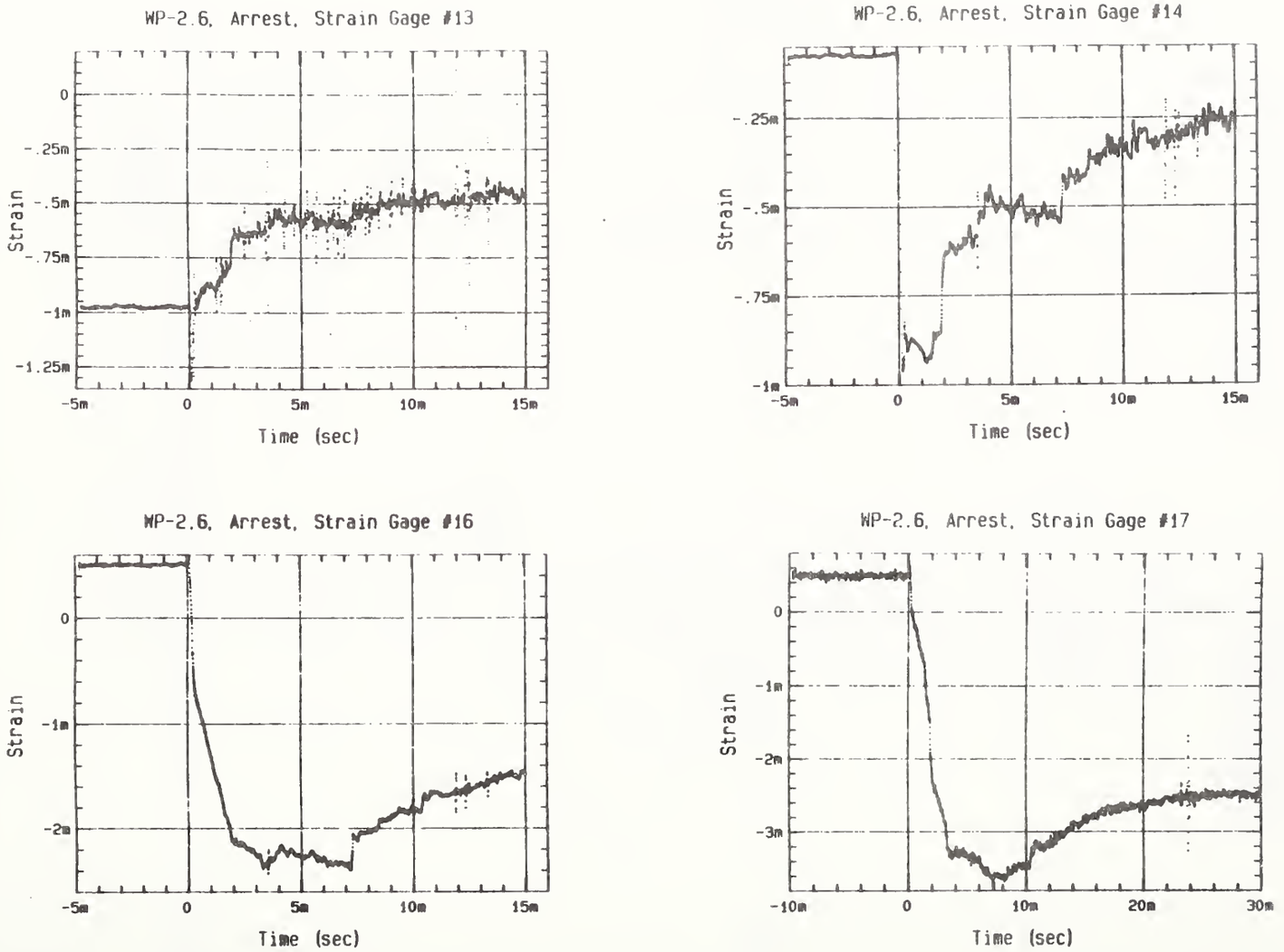

Fig. 5.5 Typical strain-time records from WP-2.6.

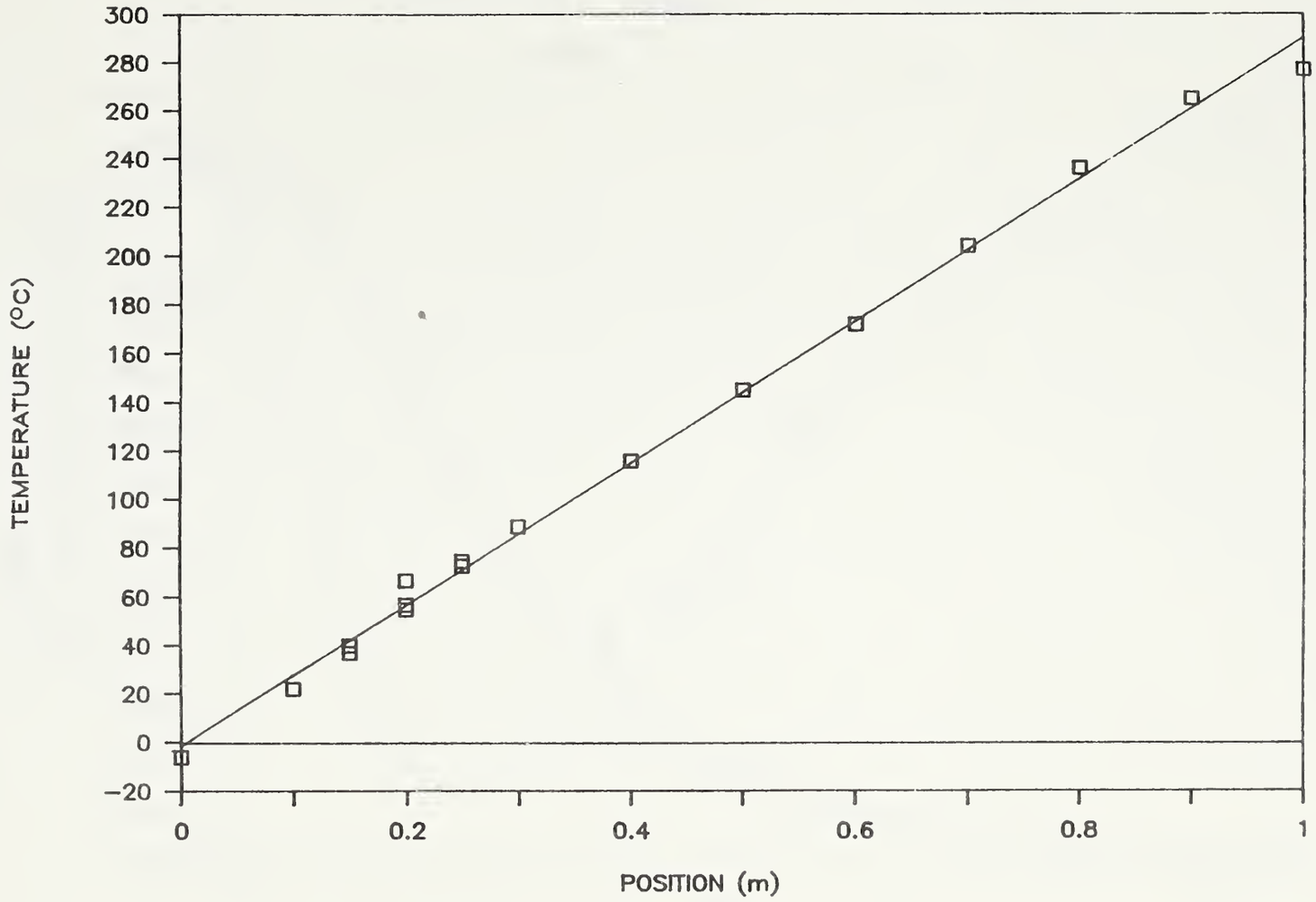

Fig. 5.6 Temperature gradient for WP-2.6.

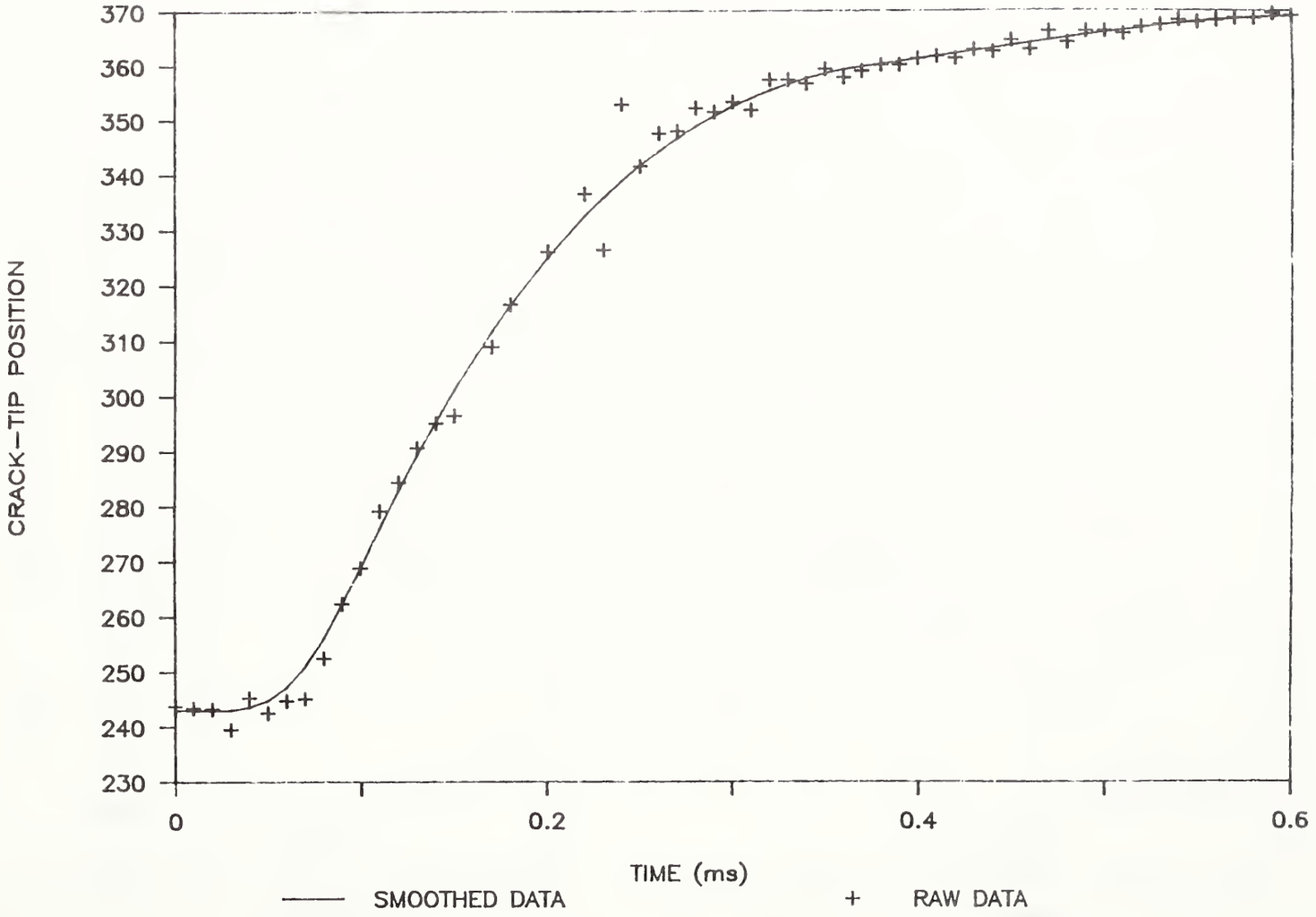

Fig. 5.7 Crack position as a function of time for WP-2.6 using the static representation of the strain field.

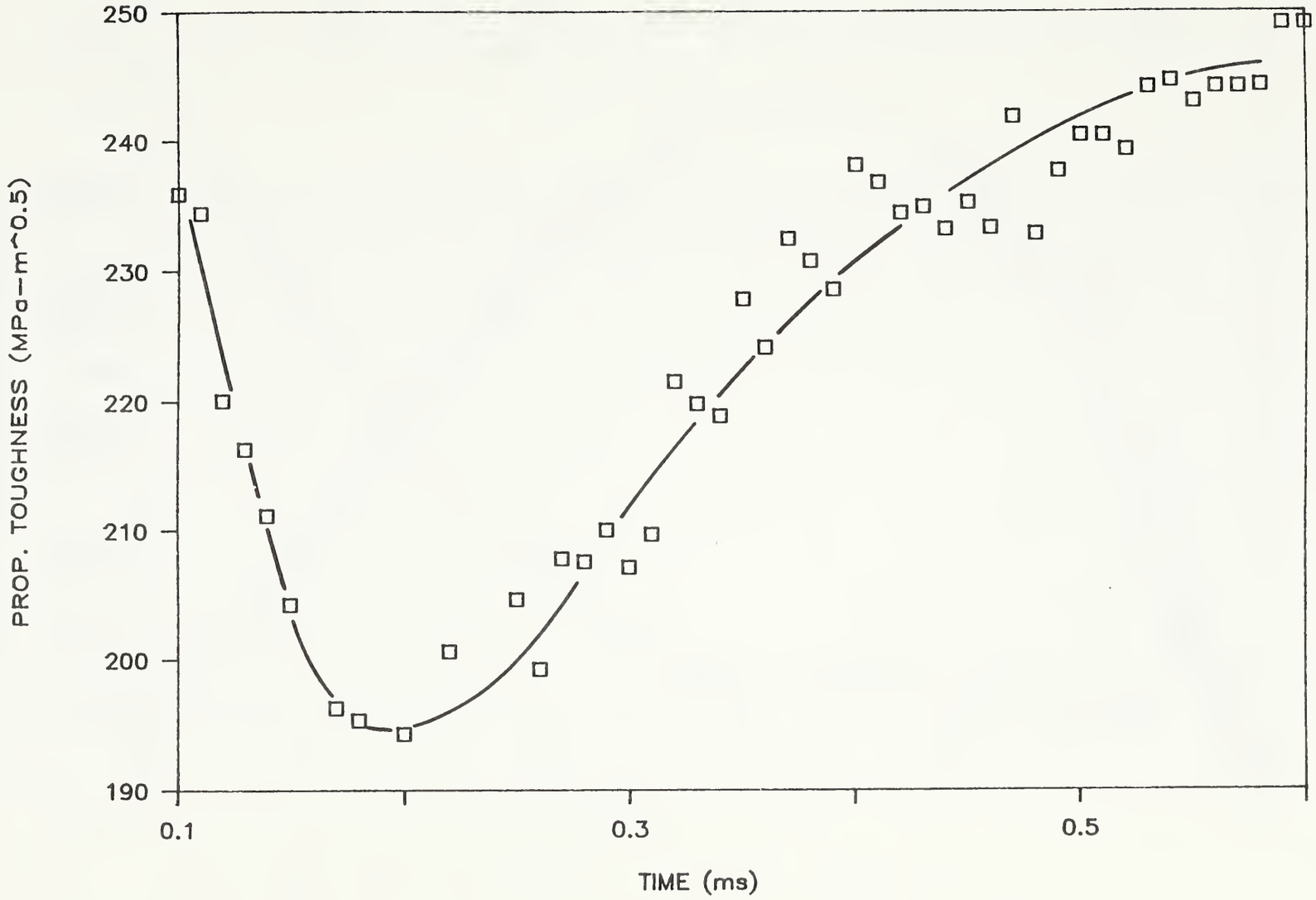

Fig. 5.8 Propagation toughness as a function of time for WP-2.6 using the static representation of the strain field.

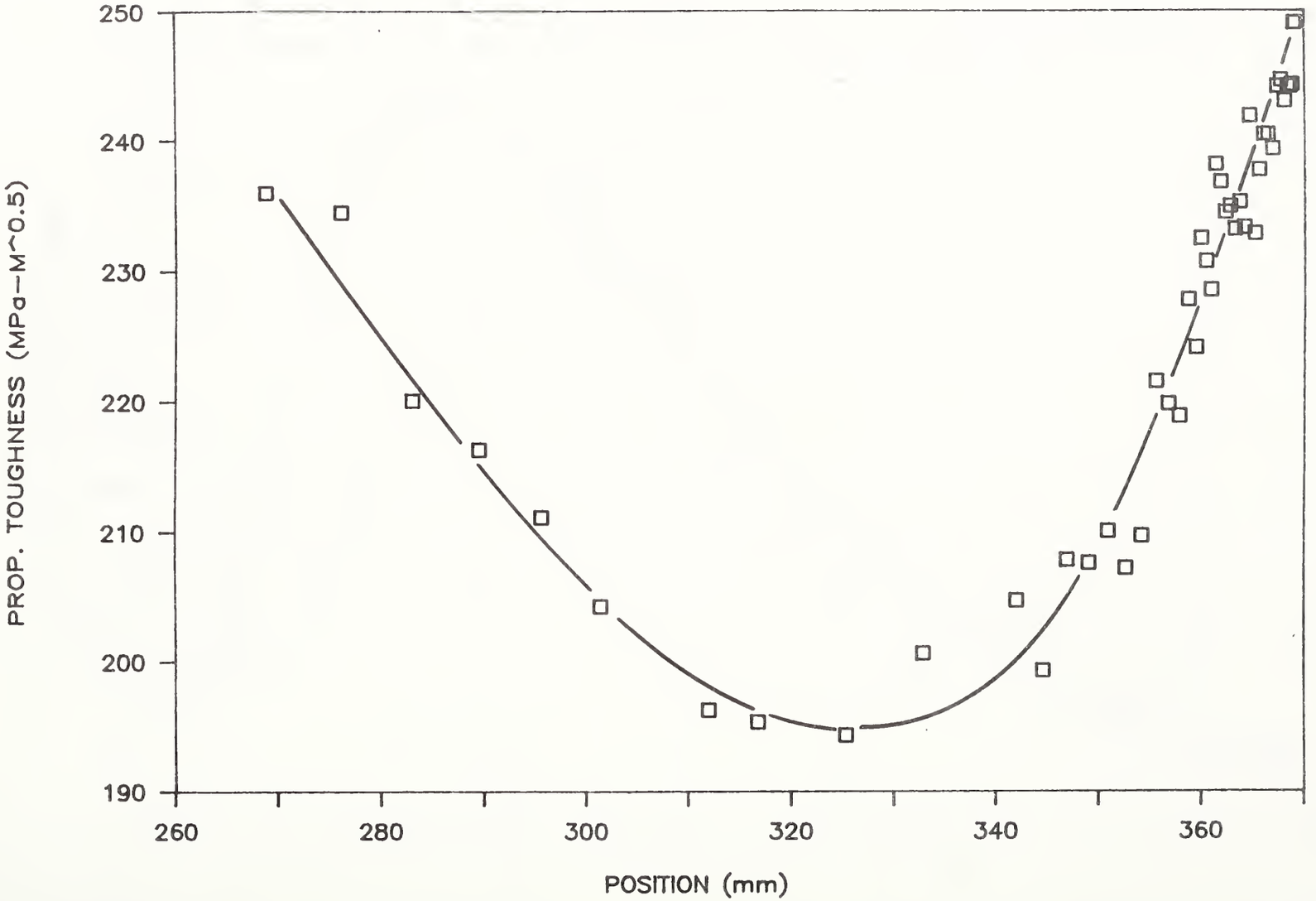

Fig. 5.9 Propagation toughness as a function of position for WP-2.6 using the static representation of the strain field.

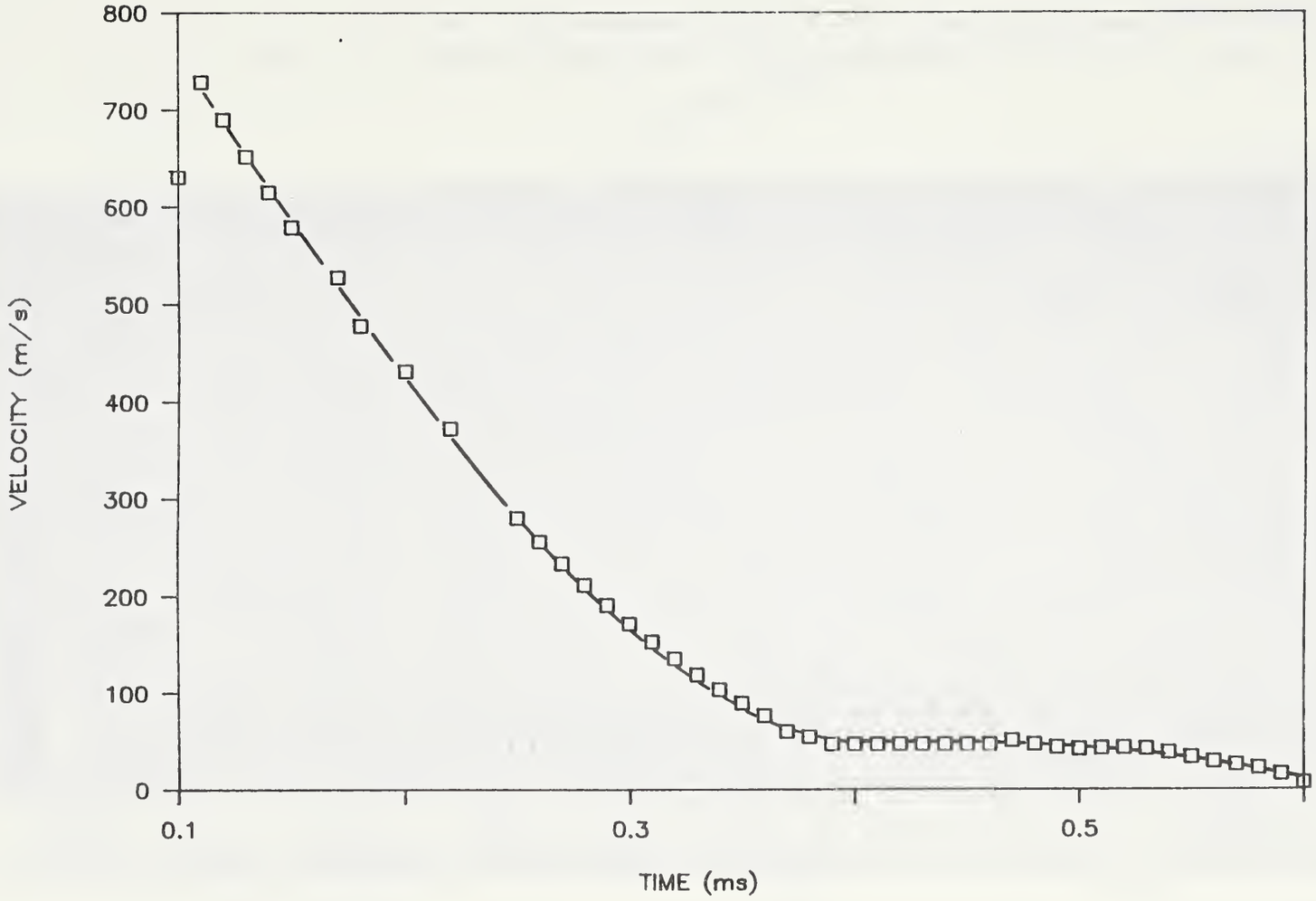

Fig. 5.10 Crack velocity as a function of time for WP-2.6.

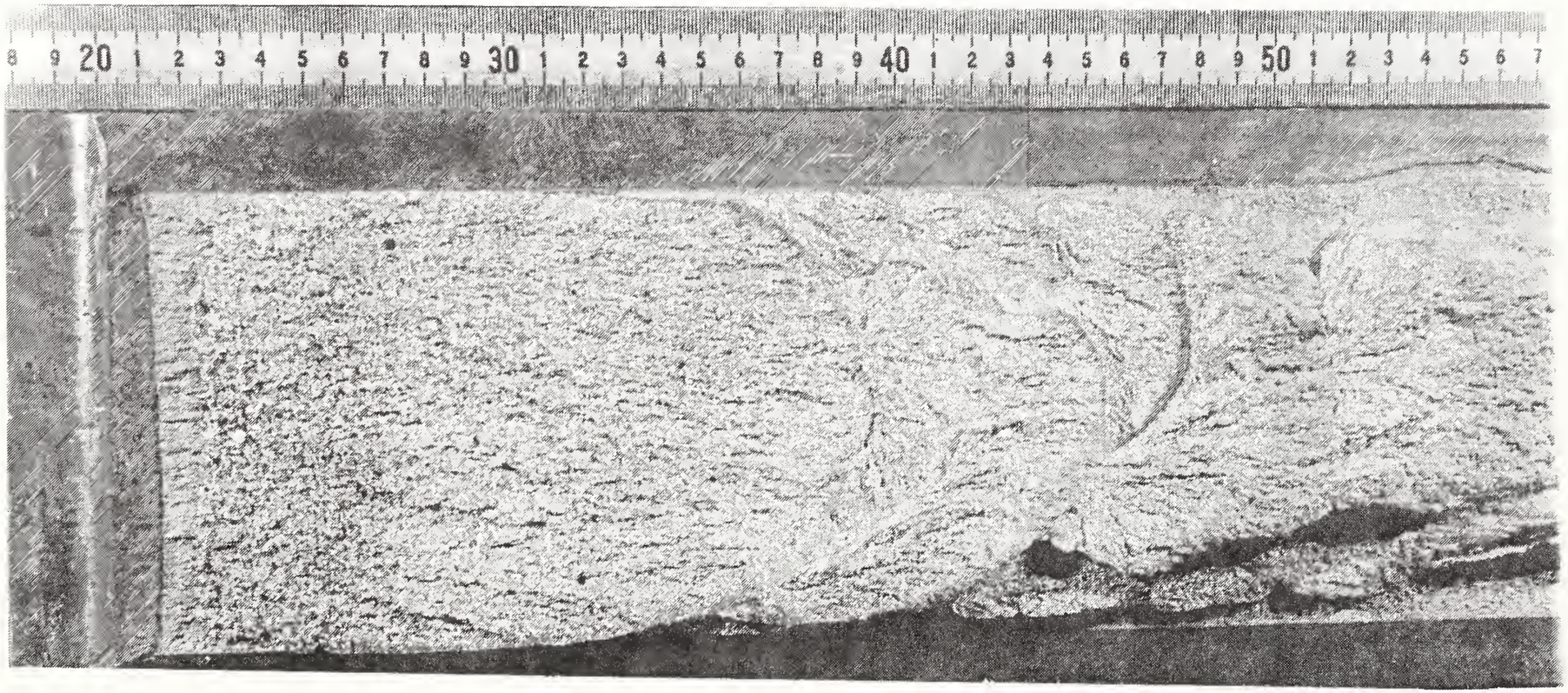

Fig. 5.11 Fracture surface of WP-2.6 showing the first arrest location (α = 45° rosettes are on the lower side of the specimen).

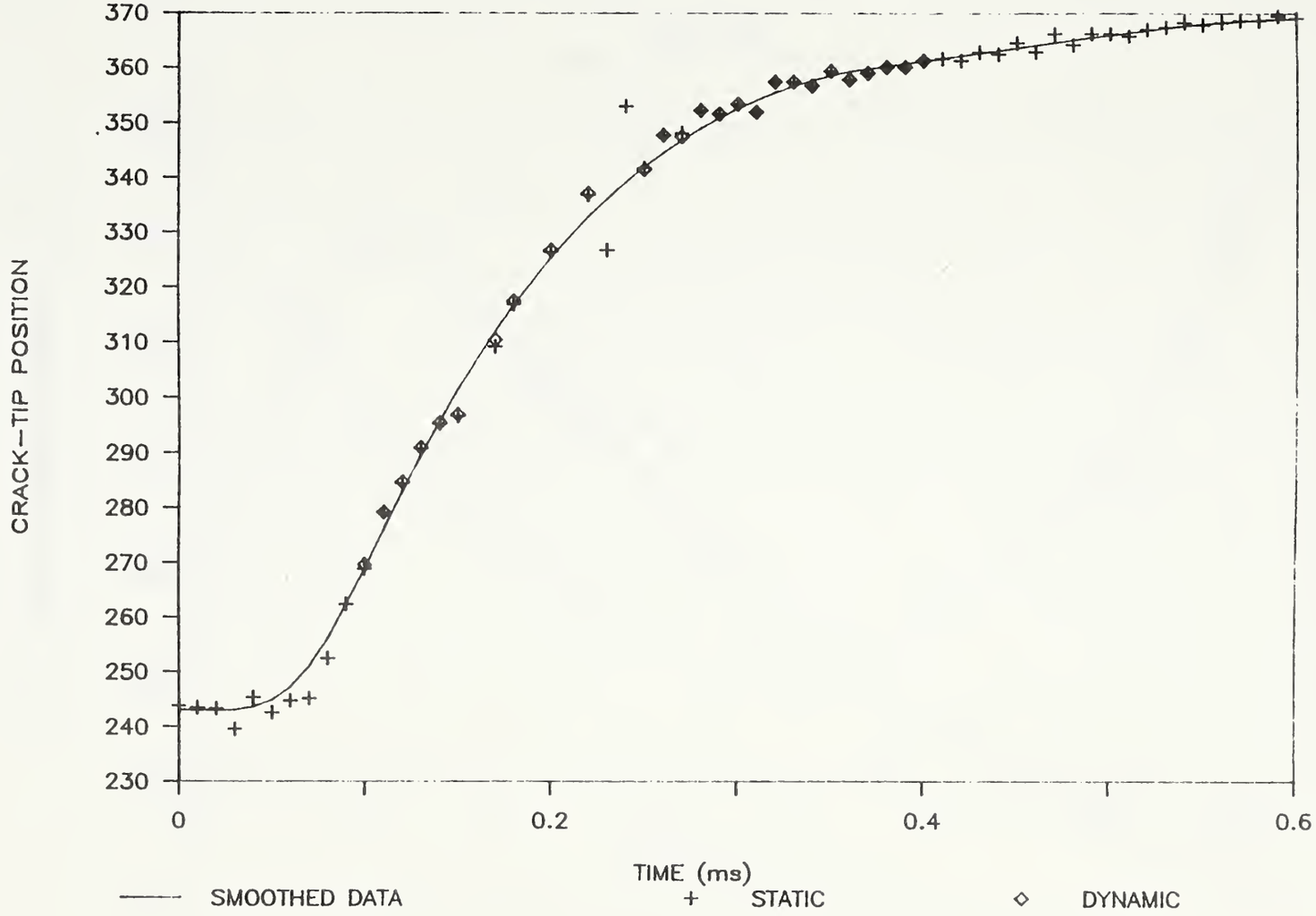

Fig. 5.12 Crack position as a function of time for WP-2.6 using both static and dynamic representations of the strain field.

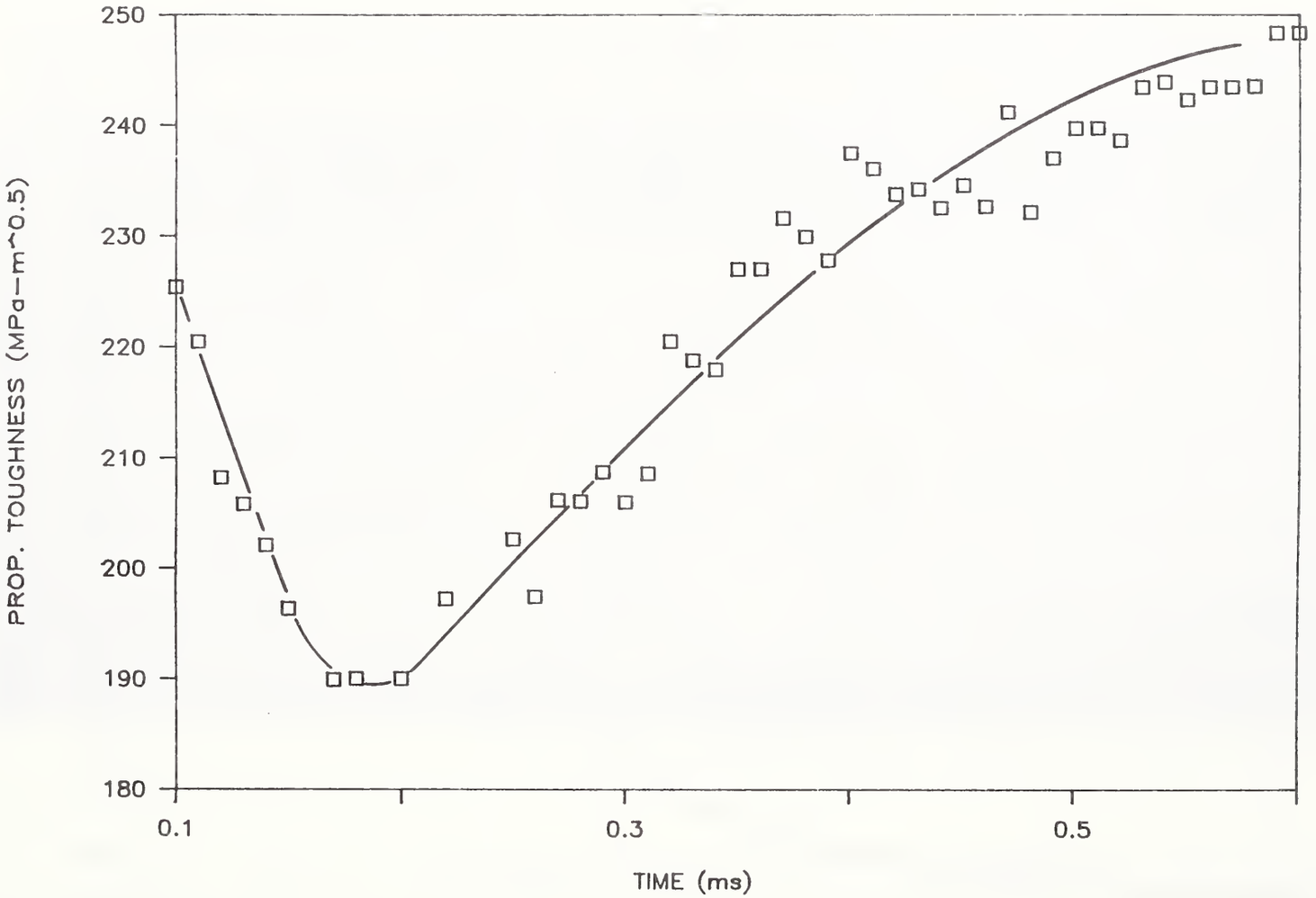

Fig. 5.13 Propagation toughness as a function of time for WP-2.6 using the dynamic representation of the strain field.

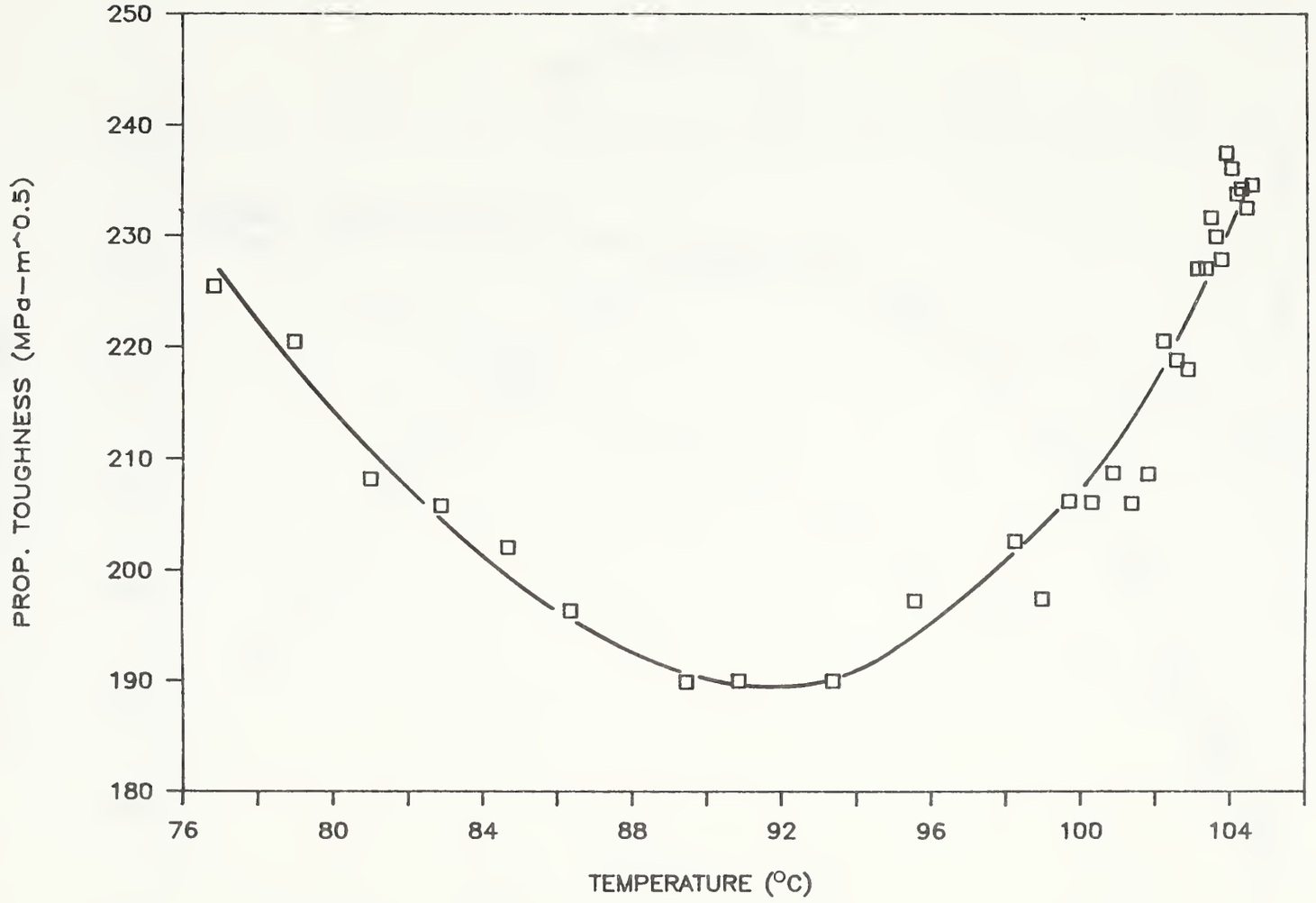

Fig. 5.14 Propagation toughness as a function of temperature for WP-2.6 using the dynamic representation of the strain field.

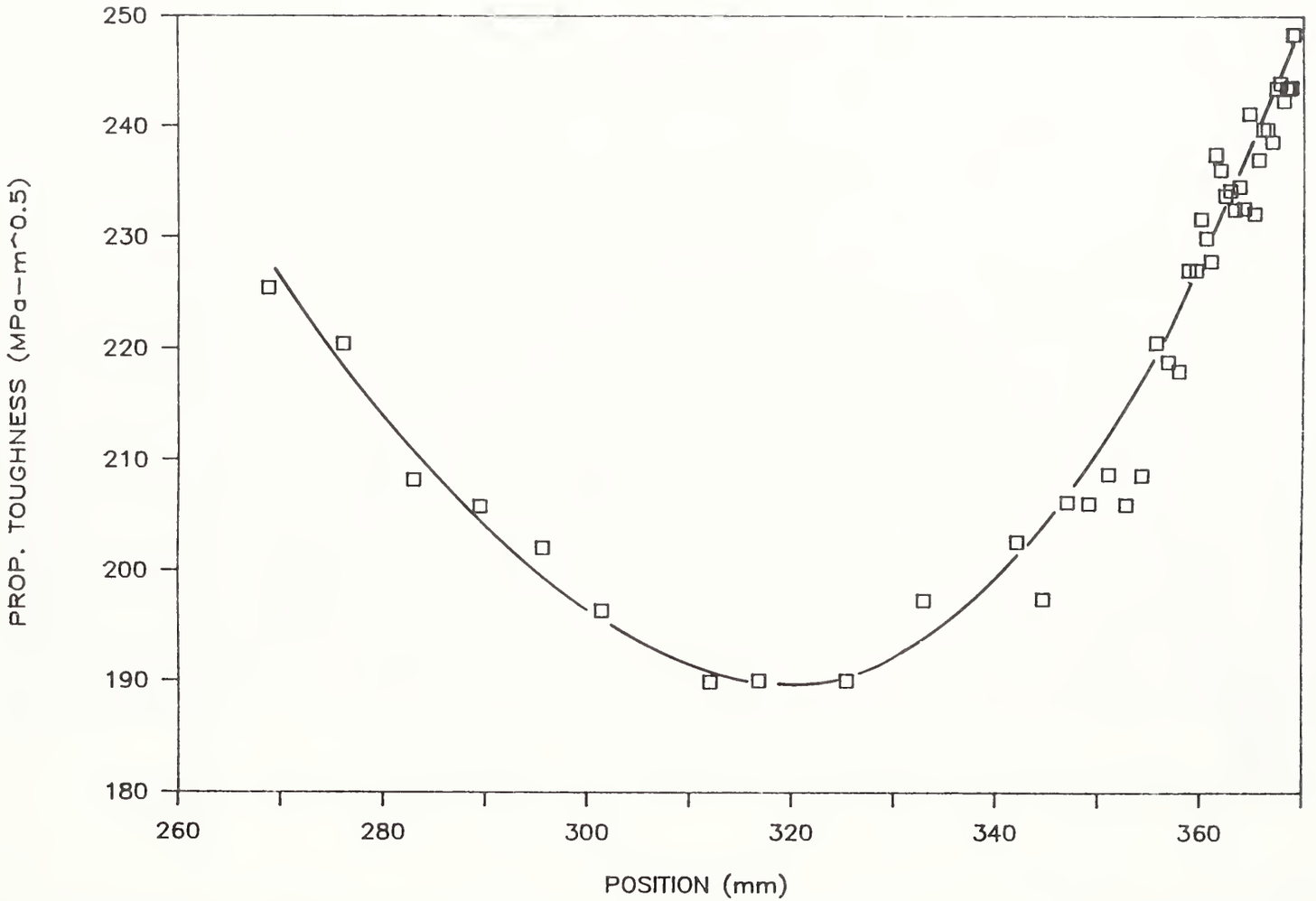

Fig. 5.15 Propagation toughness as a function of position for WP-2.6 using the dynamic representation of the strain field.

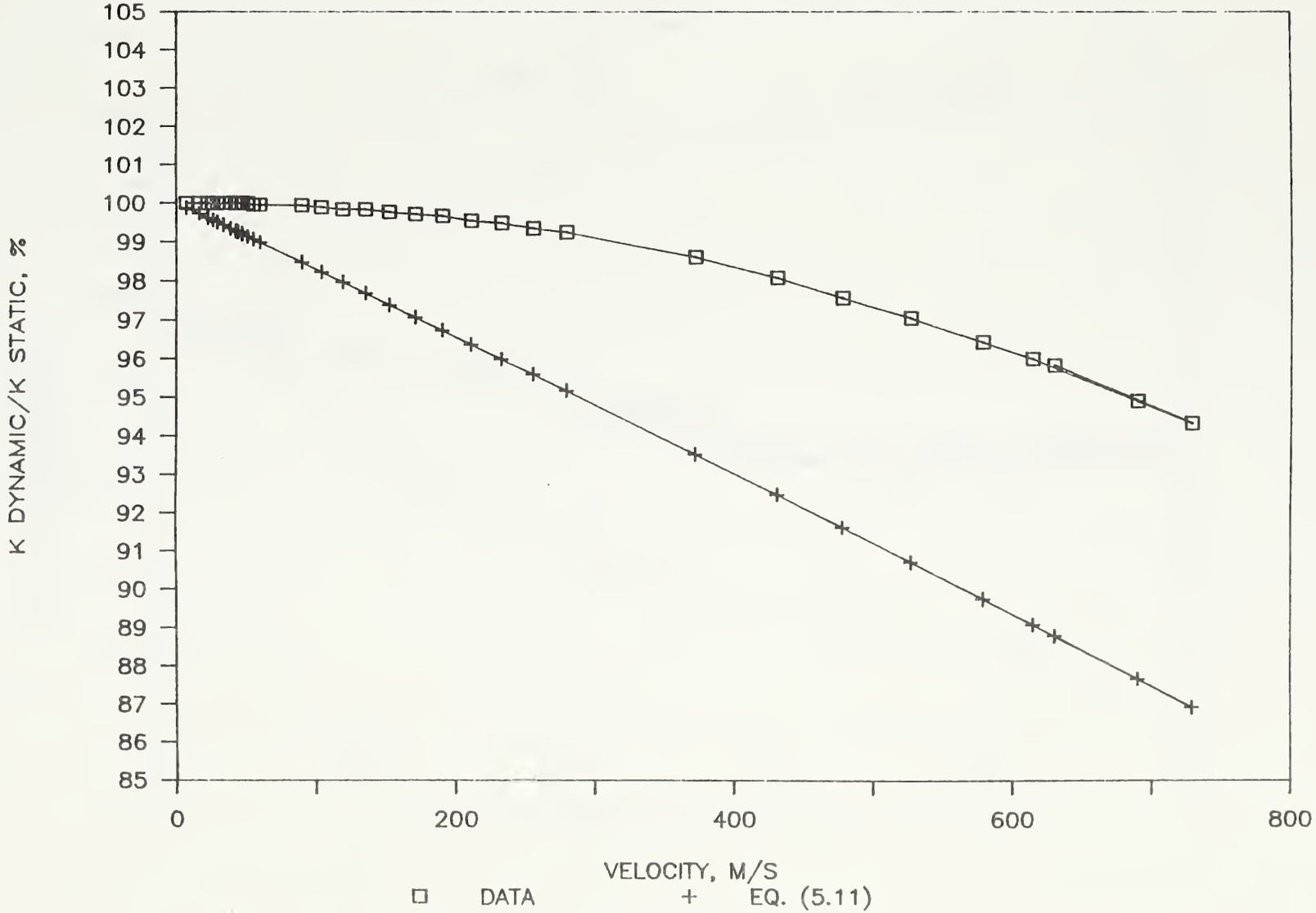

Fig. 5.16 Propagation toughness computed from both the static and dynamic strain field representations as a function of crack velocity.

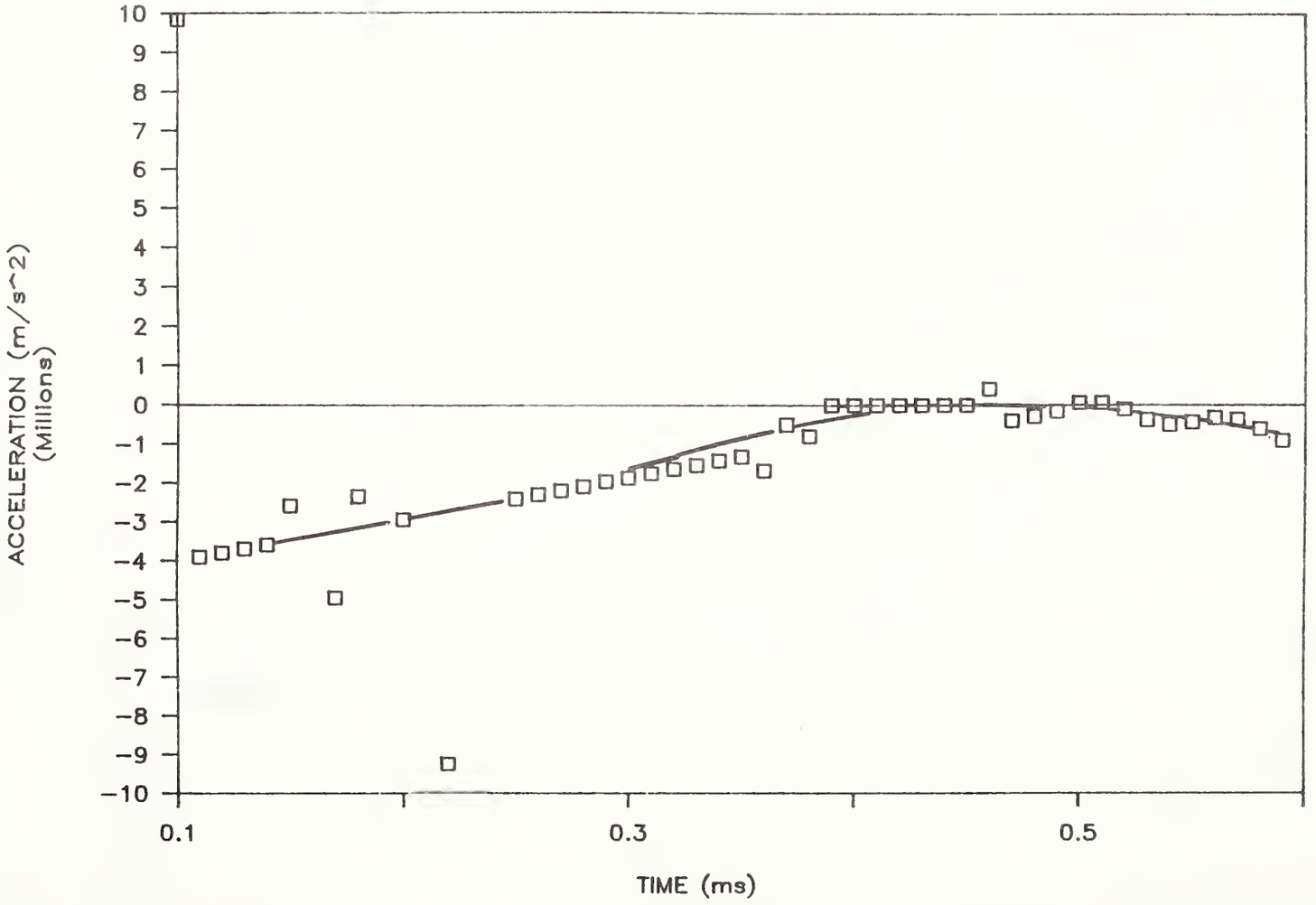

Fig. 5.17 Crack acceleration as a function of time.

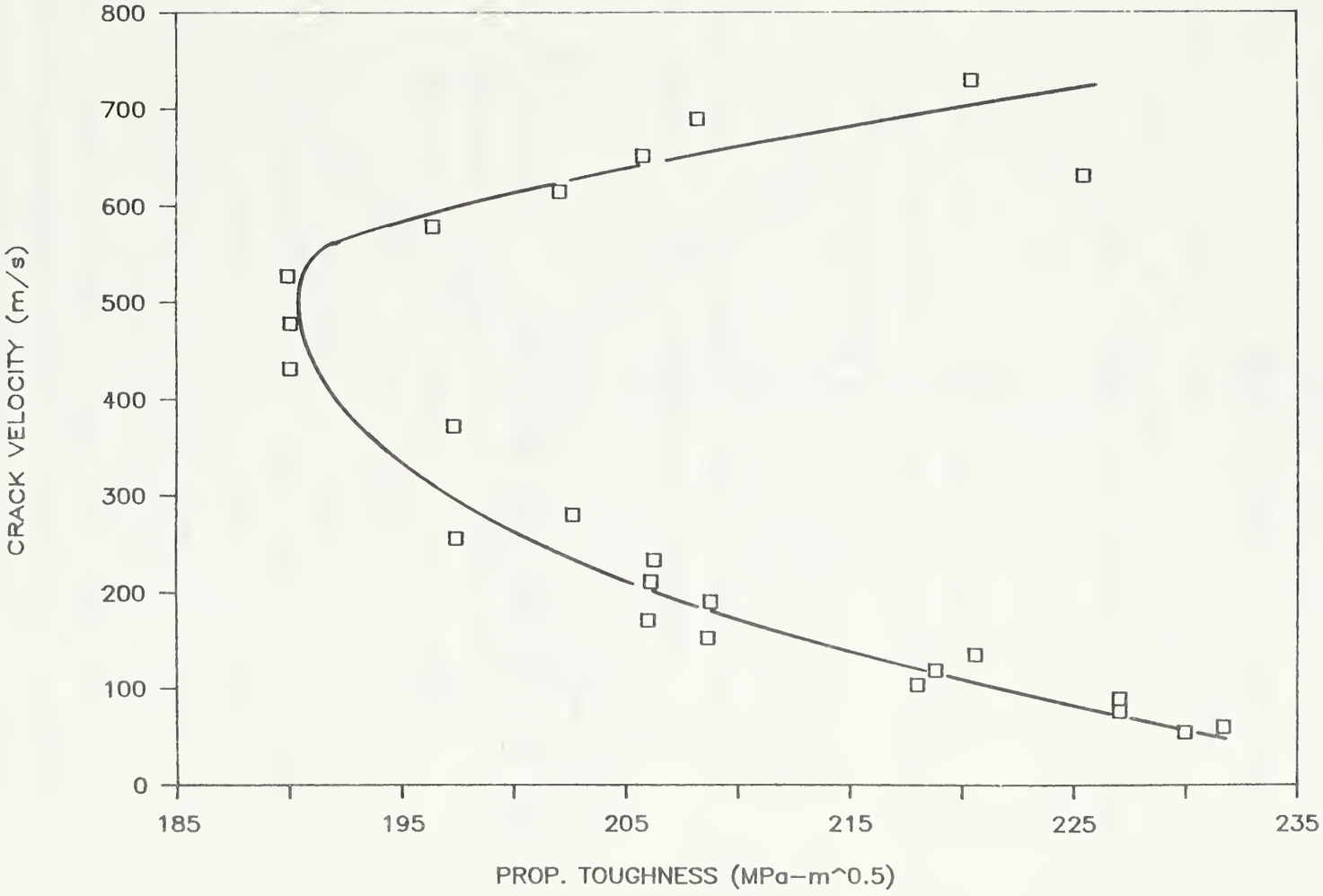

Fig. 5.18 Propagation toughness-crack velocity relation for WP-2.6.

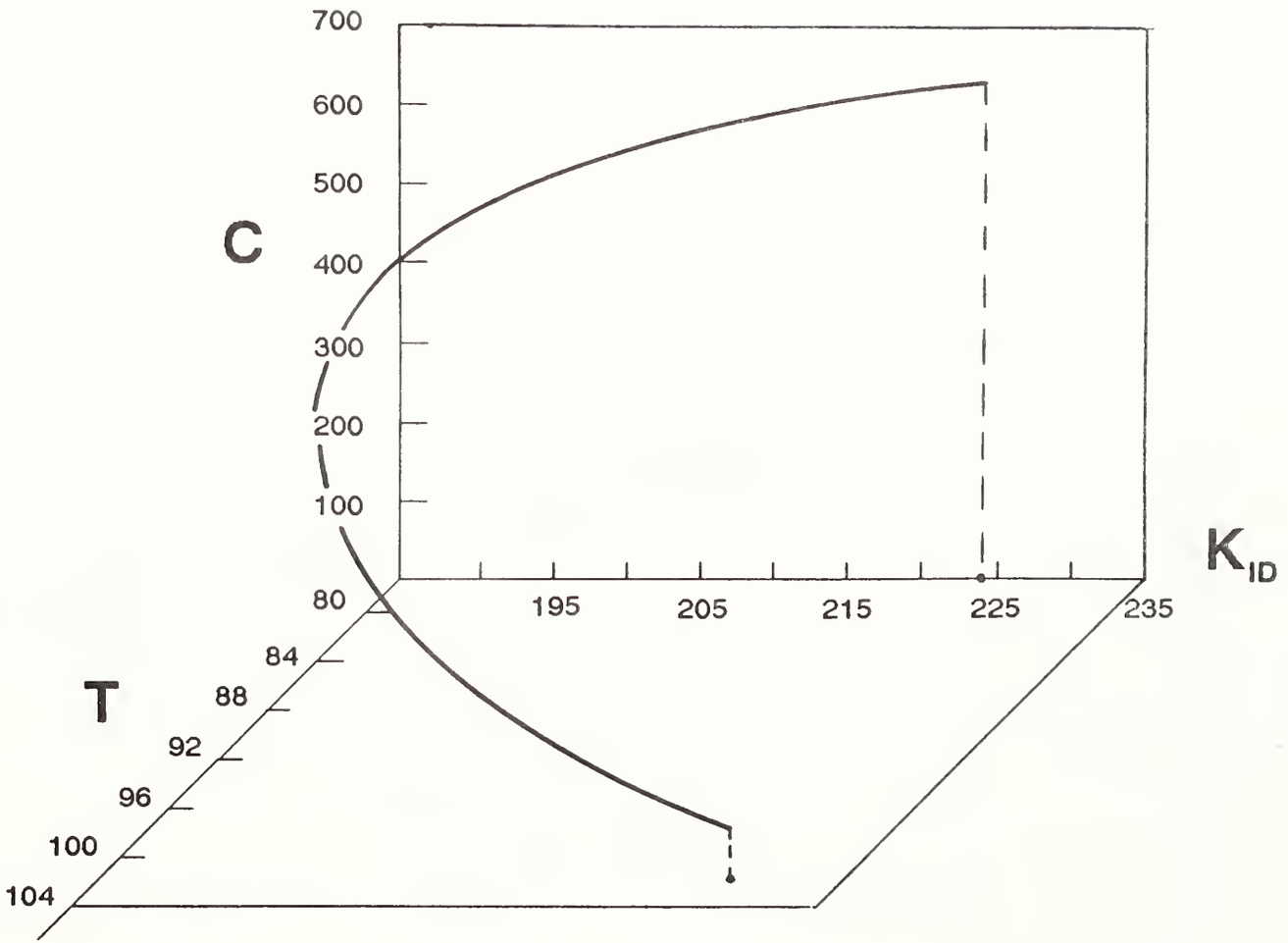

Fig. 5.19 Propagation toughness-crack velocity-temperature contour for WP-2.6

CHAPTER 6
CONCLUSIONS AND DISCUSSION

A variety of analytic techniques suitable for studying the strain field surrounding either a stationary or propagating crack have been presented in this report. The use of strain measurements in fracture analysis is attractive due to the relative simplicity of the experiments and the measurement of quantities in immediate vicinity of the crack tip. By employing the methodologies developed here, fracture parameters can be extracted from the strain records.

In reviewing the work presented in this dissertation, several important conclusions can be made concerning fracture analysis based on strain measurements:

(1) The feasibility of using strain measurements to obtain fracture parameters has been demonstrated By using the series representations of the strain field for stationary or propagating cracks, several analysis schemes were developed.

(2) The importance of including the nonsingular term A_1 became evident in the development of the algorithms for crack propagation analysis. Even though this particular parameter could not be determined accurately, it was necessary to include it in order to determine K_{ID} with sufficient accuracy.

(3) For dynamic crack propagation, two algorithms were developed to take advantage of either the spatial or temporal variation in the strain field. The viability of these algorithms was proved on a demonstration experiment conducted in 4340 steel.

(4) Orientation of the strain gage with respect to the crack propagation path is of paramount importance to optimize the strain signal for analysis and to locate the crack tip. A significant number of experiments in which the orientation suggested here was not employed have been conducted, and crack tip location was shown to be a significant problem in attempting to analyze these

records.

(5) The algorithms developed here were successfully applied to analyze a large-scale, crack-arrest test conducted in a nuclear pressure vessel steel. Both the arrest toughness and the propagation toughness-crack speed relation along a contour determined by the imposed temperature gradient were determined through the strain analysis.

6.1 SUGGESTIONS FOR FUTURE WORK

The work reported here has generated many areas worthy of investigation. These can be broadly divided into numerical analysis and fracture mechanics issues:

1. Numerical analysis issues. The large amount of data in existence for dynamic crack propagation experiments where the gages were not oriented as suggested here deem the crack tip location problem worthy of further investigation. For developing improved numerical schemes to analyze of crack tip position with $\alpha = 0^{\circ}$ rosettes we offer the following suggestions:

(i) The algorithms available in the optimization literature may offer improvements over the Newton-Raphson method used here. Although many of these algorithms are simply modifications to this method, other techniques which use direct-search methods, restricted iteration steps, conjugate gradients, or robust loss functions are available. In certain optimization case histories a simple scaling of a parameter, say scaling x to αx, changes the contours in the residual space from a highly elongated to a more desirable circular shape. By employing one or a combination of these techniques, the analysis of $\alpha = 0^{\circ}$ rosettes for crack-tip position may be possible.

(ii) The difference between a true convergence criterion versus a termination criterion for the solution algorithm should be examined. No distinction is necessary for the $\alpha = 45^{\circ}$ rosette

analysis, but a clear distinction is evident for the $\alpha = 0^{\circ}$ analysis. Perhaps a true measure of convergence based on concurrently evaluating several factors (such as the match to the applied strain field, expected coefficient values, relative changes in the parameters) would improve the $\alpha = 0^{\circ}$ results.

2. Fracture mechanics issues.

(i) The three-dimensional nature of fracture is an extremely difficult problem, especially as it relates to curvature of the crack front. However, three-dimensional elasto-plastic finite element analysis may yield useful results for relating crack tip positions determined from surface measurements to the curved crack front.

(ii) The development in Chapter 4 of regions of validity for the three-parameter model were performed at only one crack length-to-specimen width ratio and with a stationary crack. Validity zones taking crack velocity and crack extension into account would be useful for more accurately defining criteria for inclusion or exclusion of strain gages in the analysis.

(iii) The gage orientation developed here was based on eliminating nonsingular terms, primarily σ_{ox}, from the gage response. However, further studies on gage orientation may provide useful results for determining only individual parameters such as crack tip position, propagation toughness, or crack velocity.

6.2 ACKNOWLEDGEMENTS

The work presented in this report represents the dissertation submitted by the first author to the Department of Mechanical Engineering at the University of Maryland, College Park, Maryland. The authors thank Dr. H. I. McHenry, Chief of the Materials Reliability Division at the National Institute of Standards and Technology in Boulder, Colorado, for providing both time and facilities to complete this work.

APPENDIX A

THE LINEAR LEAST SQUARES PROBLEM

In Chapter 2, the formulation of the strain analysis for the stationary crack problem required the solution of a linear least squares problem. In this Appendix, we detail the theory of the linear least squares problem, present the orthogonal decomposition used to solve the system of equations, and provide the elements to the system matrices of Section 2.2.

A.1 THEORY OF LINEAR LEAST SQUARES

The general linear least squares problem,

$$\mathbb{A}\mathbf{x} = \mathbf{b}, \tag{A.1}$$

involves finding a vector $\mathbf{x}$ which minimizes the residual

$$r^2 = \| \mathbf{r} \|_2^2 = \| \mathbf{b} - \mathbb{A}\mathbf{x} \|_2^2 , \tag{A.2}$$

where $\mathbb{A}$ is a fixed $m \times n$, $m > n$, matrix of constant multipliers, $\mathbf{b}$ is a known m-vector, and $\mathbf{x}$ is the n-vector of unknown coefficients. The norm indicated by $\| \cdot \|_2$ represents the Euclidean 2-norm of a vector,

$$\| \mathbf{r} \|_2 = \left[\sum_{j=1}^{J} r_j^2 \right]^{1/2} . \tag{A.3}$$

Since the system given by eq (A.1) is overdetermined, a consistent solution usually does not exist. However, we can obtain a least squares solution to eq (A.1) by finding the best-fit vector $\mathbf{x}$ which minimizes the residual in eq (A.2).

Before establishing the procedure by which a least squares solution to eq (A.1) can be found, it is necessary to review some basic definitions and theorems from linear algebra. The theorems (offered without proof) and the definitions are standard and can be found in [A.1, A.2] or other books dealing with linear algebra.

First, the *column space* of an $m \times n$ matrix, $\mathbb{A}$, written $\mathcal{R}(\mathbb{A})$, is the subspace which is spanned by the columns of $\mathbb{A}$. Second, two complementary vector subspaces are said to be *orthogonal*

complements if and only if they are orthogonal to one another. That is, if $\mathcal{S}$ and $\mathcal{T}$ are orthogonal complements, any vector, x, can be written as $\mathbf{x} = \mathbf{s} + \mathbf{t}$ where $\mathbf{s} \in \mathcal{S}$, $\mathbf{t} \in \mathcal{T}$, and $\mathbf{s}$ is orthogonal to $\mathbf{t}$. Finally, if a vector, $\mathbf{r}$, is the projection of any vector onto the orthogonal complement of $\mathcal{R}(\mathbb{A})$, then $\mathbf{r}$ is orthogonal to $\mathcal{R}(\mathbb{A})$ and $\mathbb{A}^T\mathbf{r} = 0$ (where $\mathbb{A}^T$ is the transpose of $\mathbb{A}$).

Using these concepts, we can now formally present the solution to the linear least squares problem and outline its proof following [A.1]. If $\mathbf{x}$ is a solution to the least squares problem of minimizing eq (A.2), then the residual vector satisfies

$$\mathbb{A}^T \mathbf{r} = 0. \tag{A.4}$$

By substituting $\mathbf{r} = \mathbf{b} - \mathbb{A}\mathbf{x}$ into eq (A.4) we have the equivalent statement,

$$\mathbb{A}^T \mathbb{A}\, \mathbf{x} = \mathbb{A}^T \mathbf{b}, \tag{A.5}$$

which are commonly called the normal equations of eq (A.1). From eq (A.4) we can see that the residual vector must therefore be orthogonal to $\mathcal{R}(\mathbb{A})$.

To understand the proof that eq (A.4) solves the linear least squares problem, it is easiest to consider the problem from a graphical viewpoint and then offer the formal proof. To construct the graphical presentation, note that as the vector $\mathbf{x}$ varies the vector $\mathbf{y} = \mathbb{A}\,\mathbf{x}$ varies over the column space of $\mathbb{A}$, $\mathcal{R}(\mathbb{A})$. Therefore, minimizing eq (A.2) is equivalent to finding the vector $\mathbf{y}_{MIN}$ which minimizes $\| \mathbf{b} - \mathbf{y} \|_2^2$. This residual is obtained when $\mathbf{b} - \mathbf{y}$ is orthogonal to $\mathcal{R}(\mathbb{A})$ as can be seen in figure A.1. In the figure, the minimum length of the vector, $\mathbf{r}$, is attained when it is orthogonal to $\mathbf{y}$ (keep in mind that $\mathbf{b}$ is of "fixed" length and we are varying $\mathbf{y}$). This is a simple two-dimensional view of the multi-dimensional least squares problem, but it is quite helpful in understanding the role of orthogonal projections in linear least squares.

With reference to figure A.1, let $\mathbf{b}_1$ lie in $\mathcal{R}(\mathbb{A})$ and $\mathbf{b}_2$ lie

in the orthogonal complement of $\mathcal{R}(\mathbb{A})$. Then $\mathbf{b} = \mathbf{b}_1 + \mathbf{b}_2$, the vector $\mathbf{y}_{MIN} = \mathbf{b}_1$ and the residual vector $\mathbf{r} = \mathbf{b}_2$. The linear least squares problem can thus be considered a multi-dimensional orthogonal projection problem. On obtaining $\mathbf{y}_{MIN}$, we have minimized eq (A.2).

Now, returning to the proof that eq (A.4) represents the least squares solution to eq (A.1), if $\mathbf{x}$ minimizes eq (A.2) then $\mathbb{A}\mathbf{x} = \mathbf{b}_1$ and $\mathbf{r} = \mathbf{b}_2 = \mathbf{b} - \mathbf{b}_1$. However, as discussed in the previous paragraph, $\mathbf{b}_2$ is in the orthogonal complement of $\mathcal{R}(\mathbb{A})$. Then, by definition, $\mathbb{A}^T\mathbf{b}_2 = 0$. So, $\mathbb{A}^T\mathbf{r} = 0$ which is eq (A.4). Therefore, the solution of eq (A.1) by the normal equations has been proved.

The implementation of the normal equations has been found to generate numerical instabilities in certain cases [A.3, A.4], not all of which involved models with large numbers of terms. Even Stewart [A.1] states that the normal equations are "tricky to use," even if double precision is used on the computer, since the condition of the normal equations may be even worse than the condition of the original least squares problem. A numerically stable method of calculating the solution to the linear least squares problem can be obtained using a method of orthogonalization known as the QR decomposition.

A.2 THE QR DECOMPOSITION

To present the details of the QR decomposition, it is again necessary to review several concepts from linear algebra [A.1, A.2]. Most of these deal with the properties of orthogonal vectors, matrices, and transformations which play a central role in the theory of the decomposition described here. Orthogonal transformations are inherently stable and have low storage requirements and are therefore of great interest in numerical

linear algebra.

Constructing the QR decomposition requires the use of an orthogonal transformation which is called a variety of names including an elementary reflector, an elementary orthogonal matrix, or an elementary Hermitian matrix. These transformations are matrices of the form,

$$\mathbb{H} = \mathbb{I} - 2\,\mathbf{u}\,\mathbf{u}^T, \tag{A.6}$$

where $\mathbf{u}$ is an n-vector which satisfies

$$\| \mathbf{u} \|_2 = \mathbf{u}^T\mathbf{u} = 1, \tag{A.7}$$

and $\mathbb{I}$ is the identity matrix. In general, a matrix $\mathbb{Q}$ is orthogonal if

$$\mathbb{Q}^{-1} = \mathbb{Q}^T \tag{A.8}$$

and

$$\| \mathbb{Q}\,\mathbf{y} \|_2 = \| \mathbb{Q}^T\,\mathbf{y} \|_2 = \| \mathbf{y} \|_2 \tag{A.9}$$

for any vector $\mathbf{y}$. The matrix $\mathbb{H}$ is called an elementary orthogonal matrix because it satisfies

$$\mathbb{H}^{-1} = \mathbb{H}^T = \mathbb{H}, \tag{A.10}$$

which can be proved through the use of eq (A.7). Finally, $\mathbb{H}$ is completely determined by the vector, $\mathbf{u}$. This is helpful in computations since only $\mathbf{u}$ need be stored.

Recall from basic linear algebra that the method of Gauss elimination can be performed by applying a series of transformations which transform a matrix into one that is in upper triangular form; that is, the transformations introduce zeros into the matrix below the main diagonal. Similarly, we can choose the form of $\mathbf{u}$ in eq (A.6) so that when a series of these transformations are applied to a matrix it is reduced to upper triangular form. The particular form of $\mathbb{H}$ which allows us to perform this operation is known as a Householder transformation.

Without proof, we define the Householder transformation as

$$\mathbb{H} = \mathbb{I} - \frac{1}{\beta} \mathbf{v}\,\mathbf{v}^T. \tag{A.11}$$

Details regarding the proof of orthogonality, etc., can be found in [A.2]. The terms in eq (A.11) are defined as

$$\beta = \alpha\,(\alpha - x_1) \tag{A.12}$$

$$\alpha = \| \mathbf{x} \|_2 \tag{A.13}$$

$$\mathbf{v} = (x_1 - \alpha,\ x_2,\ x_3,\ \ldots,\ x_n), \tag{A.14}$$

where $\mathbf{x}$ is the first column of the matrix $\mathbb{A}$ which is to be reduced. Finally, the vectors $\mathbf{u}$ and $\mathbf{v}$ are related by

$$\mathbf{u} = \frac{1}{\|\mathbf{v}\|_2} \mathbf{v}, \tag{A.15}$$

which is simply a normalization of $\mathbf{v}$. Iterative formulas similar to eqs (A.12) - (A.14) are given in [A.2] for constructing the Householder transformation for the remaining columns of $\mathbb{A}$.

Now, if $\mathbb{A}$ is an m x n matrix, we can apply a series of Householder transformations to reduce $\mathbb{A}$ to triangular form. We apply the first transformation, $\mathbb{H}_1$, to introduce zeros in the first column of $\mathbb{A}$ below $(\mathbb{A})_{11}$. A second transformation, $\mathbb{H}_2$, is then applied to $\mathbb{H}_1\mathbb{A}$, which introduces zeros in the second column of $\mathbb{H}_1\mathbb{A}$ below $(\mathbb{H}_1\mathbb{A})_{22}$. Continuing this sequence n - 1 times, we arrive at the matrix $\mathbb{R}$, which is upper triangular with a nonzero diagonal,

$$\mathbb{H}_{n-1} \cdot \cdot \cdot \mathbb{H}_3\, \mathbb{H}_2\, \mathbb{H}_1\, \mathbb{A} = \mathbb{R}. \tag{A.16}$$

Now we take advantage of the property of elementary orthogonal transformations given in eq (A.10) to write

$$\begin{aligned} \mathbb{A} &= \mathbb{H}_1^{-1}\, \mathbb{H}_2^{-1}\, \mathbb{H}_3^{-1} \cdot \cdot \cdot \mathbb{H}_{n-1}^{-1}\, \mathbb{R} \\ &= \mathbb{H}_1\, \mathbb{H}_2\, \mathbb{H}_3 \cdot \cdot \cdot \mathbb{H}_{n-1}\, \mathbb{R}. \end{aligned} \tag{A.17}$$

Now, let us define

$$\mathbb{Q} = \mathbb{H}_1 \mathbb{H}_2 \mathbb{H}_3 \cdots \mathbb{H}_{n-1}, \tag{A.18}$$

where $\mathbb{Q}$ is orthogonal based on the properties of the $\mathbb{H}_j$'s. We then have the orthogonal decomposition

$$\mathbb{A} = \mathbb{Q}\,\mathbb{R}. \tag{A.19}$$

Since $\mathbb{R}$ is an m x n upper triangular matrix, we can partition it as

$$\mathbb{R} = \begin{bmatrix} \mathbb{R}_1 \\ 0 \end{bmatrix}. \tag{A.20}$$

We now return to the linear least squares problem where we wish to minimize the residual

$$\mathbf{r} = \mathbf{b} - \mathbb{A}\,\mathbf{x}. \tag{A.21}$$

Multiplying eq (A.21) by $\mathbb{Q}^T$ yields

$$\mathbb{Q}^T \mathbf{r} = \mathbb{Q}^T \mathbf{b} - \mathbb{Q}^T \mathbb{A}\,\mathbf{x}. \tag{A.22}$$

If we define the partitioned product

$$\mathbb{Q}^T \mathbf{b} = \begin{bmatrix} \mathbf{c} \\ \mathbf{d} \end{bmatrix}, \tag{A.23}$$

then eq (A.22) becomes

$$\mathbb{Q}^T \mathbf{r} = \begin{bmatrix} \mathbf{c} \\ \mathbf{d} \end{bmatrix} - \mathbb{Q}^T \mathbb{A}\,\mathbf{x}. \tag{A.24}$$

Now, since $\mathbb{A} = \mathbb{Q}\,\mathbb{R}$ and $\mathbb{Q}$ is orthogonal ($\mathbb{Q}^T = \mathbb{Q}^{-1}$),

$$\mathbb{Q}^T \mathbf{r} = \begin{bmatrix} \mathbf{c} \\ \mathbf{d} \end{bmatrix} - \mathbb{R}\,\mathbf{x}. \tag{A.25}$$

Substituting the partitioning of eq (A.20) we obtain

$$\mathbb{Q}^T \mathbf{r} = \begin{bmatrix} \mathbf{c} \\ \mathbf{d} \end{bmatrix} - \begin{bmatrix} \mathbb{R}_1 \\ 0 \end{bmatrix} \mathbf{x}$$

$$= \begin{bmatrix} \mathbf{c} - \mathbb{R}_1 \mathbf{x} \\ \mathbf{d} \end{bmatrix}. \tag{A.26}$$

Now, let us form the expression for the norm of eq (A.26) where we can take advantage of the orthogonality of $\mathbb{Q}$ defined in eq (A.9),

$$\| \mathbb{Q}^T \mathbf{r} \|_2^2 = \| \mathbf{r} \|_2^2 = \| \mathbf{c} - \mathbb{R}_1 \mathbf{x} \|_2^2 + \| \mathbf{d} \|_2^2. \qquad (A.27)$$

Now, since $\mathbf{d}$ is "fixed" we can minimize the residual by finding $\mathbf{x}$ such that $\| \mathbf{c} - \mathbb{R}_1 \mathbf{x} \|_2^2 = 0$. This is a straightforward task since $\mathbb{R}_1$ is $n \times n$; i.e., we simply solve the determined system

$$\mathbf{c} - \mathbb{R}_1 \mathbf{x} = 0. \qquad (A.28)$$

Note that we can also directly calculate the residual since, if we solve eq (A.28),

$$\| \mathbf{r} \|_2^2 = \| \mathbf{d} \|_2^2. \qquad (A.29)$$

Also, from eq (A.26) with $\mathbf{c} - \mathbb{R}_1 \mathbf{x} = 0$, we can form $\mathbf{r}$ from

$$\mathbb{Q}^T \mathbf{r} = \begin{bmatrix} 0 \\ \mathbf{d} \end{bmatrix}. \qquad (A.30)$$

Since $\mathbb{Q}$ is orthogonal we can directly calculate $\mathbf{r}$ as

$$\mathbf{r} = \mathbb{Q} \begin{bmatrix} 0 \\ \mathbf{d} \end{bmatrix}. \qquad (A.31)$$

The description of the QR decomposition given above provides the outline for an efficient algorithm. Well developed, stable algorithms for the decomposition have been included in the Linpack package of linear algebra subroutines [A.5]. The Linpack package was used throughout this dissertation for solving both the linear least squares problem and the linear portion of the nonlinear least squares problem.

A.3 ELEMENTS OF THE MATRICES

In Section 2.2, the strain gage analysis was formulated as a linear least squares problem,

$$\mathbb{D}\,\mathbf{c} = \mathbf{b}. \tag{A.32}$$

In this section we define the elements of the matrix and vectors in eq (A.32). First, we define the multiplier matrix $\mathbb{D}$ using the definitions of the f_j and g_j from Section 2.2. The lowermost subscript indicates the gage number:

$$\mathbb{D} = \begin{bmatrix} f_{0_1} & g_{0_1} & f_{1_1} & g_{1_1} & f_{2_1} & g_{2_1} \\ f_{0_2} & g_{0_2} & f_{1_2} & g_{1_2} & f_{2_2} & g_{2_2} \\ \cdot & \cdot & \cdot & \cdot & \cdot & \cdot \\ \cdot & \cdot & \cdot & \cdot & \cdot & \cdot \\ \cdot & \cdot & \cdot & \cdot & \cdot & \cdot \\ f_{0_n} & g_{0_n} & f_{1_n} & g_{1_n} & f_{2_n} & g_{2_n} \end{bmatrix}. \tag{A.33}$$

The vector $\mathbf{c}$ contains the unknown series coefficients,

$$\mathbf{c} = \left[A_0,\ B_0,\ A_1,\ B_1,\ A_2,\ B_2 \right]^T, \tag{A.34}$$

and the vector $\mathbf{b}$ contains the data from the n strain gages,

$$\mathbf{b} = \left[2\mu\varepsilon_{g_1},\ 2\mu\varepsilon_{g_2},\ \cdots\ 2\mu\varepsilon_{g_n} \right]^T. \tag{A.35}$$

REFERENCES

[A.1] Stewart, G. W., **Introduction to Matrix Computations**, Academic Press, New York, New York (1973).

[A.2] Leon, S. J., **Linear Algebra with Applications**, Macmillan Publishing Co., New York, New York (1980).

[A.3] Eason, E. D., "A Review of Least-Squares Methods for Solving Partial Differential Equations," **International Journal for Numerical Methods in Engineering**, Vol. 10, pp. 1021-1046 (1976).

[A.4] Longley, J. W., **Least Squares Computations Using Orthogonalization Methods**, Marcel Dekker, Inc., New York, New York (1984).

[A.5] Dungarra, J.J., Moler, C.B., Bunch, J.R., and Stewart, G.W., **Linpack Users Guide**, Society for Industrial and Applied Mathematics,
1979.

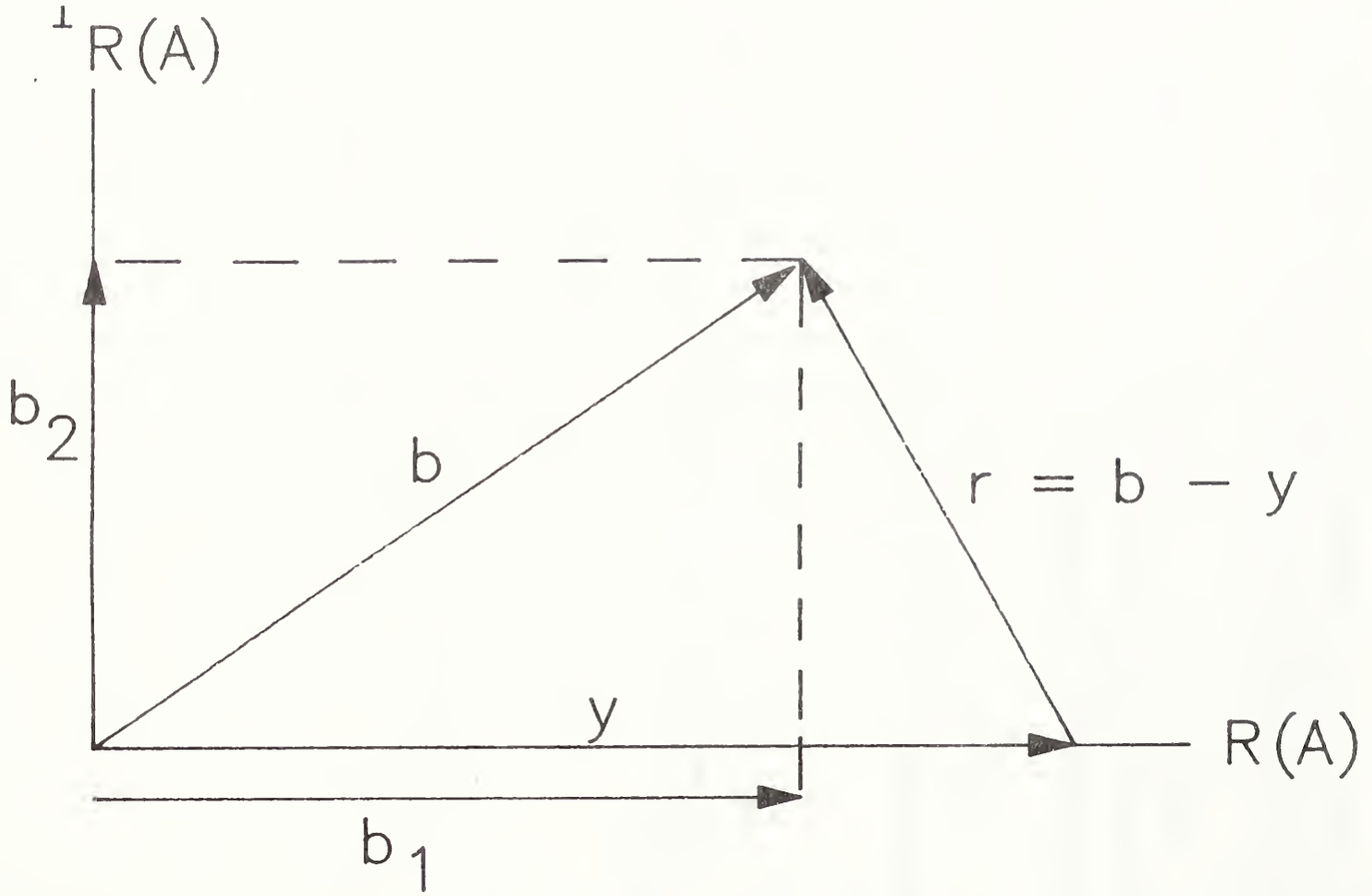

Fig. A.1 Graphical interpretation of the linear least squares problem.

APPENDIX B

THE NONLINEAR LEAST SQUARES PROBLEM

In Chapter 3, an algorithm was presented which took advantage of the spatial variations in strain to determine the fracture parameters. The resulting system of equations was overdetermined and nonlinear in one of the three variables. In this appendix, we discuss the theory of nonlinear least squares problems, present the Newton-Rapheson (or Newton) method for iteratively solving the system of equations, and provide the elements of the system matrices in Section 3.3.

B.1 THEORY OF NONLINEAR LEAST SQUARES

The general problem of determining the least squares solution to a system of equations

$$\mathbf{y} = f(\mathbf{t}) \tag{B.1}$$

requires us to minimize the 2-norm of the least squares residual

$$r = \| \mathbf{r} \|_2^2 = \| \mathbf{y} - f(\mathbf{t}) \|_2^2, \tag{B.2}$$

where $\mathbf{t}$ are unknown parameters, some or all of which are related nonlinearly to $\mathbf{y}$; and the defintion of the 2-norm is given in Appendix A. Although the general problem presented here holds many parallels to the linear least squares problem presented in Appendix A, one important difference is the fact that we may find many local minima to eq (B.2). In linear least squares analysis we are guarnteed to only have one minimum. This fact, together with the inability to analytically solve the normal equations for the system, renders nonlinear least squares analysis considerably more difficult than its linear counterpart.

At a minimum, say at $\mathbf{t} = \mathbf{t}^*$, the derivative of r must satisfy

$$\left. \frac{\partial r}{\partial \mathbf{t}} \right|_{\mathbf{t}=\mathbf{t}^*} = 0. \tag{B.3}$$

From eqs (B.2) and (B.3), one can arrive at the normal equations which were shown in Appendix A. However, here the normal

equations can not be solved analytically, and we are forced to use iterative techniques.

B.1 THE NEWTON-RAPHSON ITERATIVE PROCEDURE

A variety of techniques are available for the solution of systems of nonlinear equations. Here we will show the details of a solution using the Newton-Raphson, or Newton, method. Details of other methods can be found in [B.1 - B.3]. Although the Newton-Raphson method is perhaps the most elementary of the methods, the algorithm has been found to work well in a variety of applications.

Restating the problem, we wish to find a zero of the residual function

$$\mathbf{r} = \mathbf{y} - f(\mathbf{t}) = 0. \tag{B.4}$$

Expanding eq (B.4) into a Taylor series and retaining only the first two terms we obtain

$$\mathbf{r}_{i+1} = \mathbf{r}_i + \frac{\partial f}{\partial \mathbf{t}} \Delta \mathbf{t}, \tag{B.5}$$

where i is the iteration step and $\Delta \mathbf{t}$ is the increment in the parameters $\mathbf{t}$. Since the desired result is $\mathbf{r}_{i+1} = 0$, we obtain the linearization,

$$-\mathbf{r}_i = \frac{\partial f}{\partial \mathbf{t}} \Delta \mathbf{t}. \tag{B.6}$$

Note that eq (B.6) is simply a multivariable form of the well known Newton's method of finding roots of equations. With the linearization of eq (B.6), we can solve for the increments in the parameters, $\Delta \mathbf{t}$, using the methods presented in Appendix A. The solution is then iterated until a reasonable measure of convergence is attained.

B.3 ELEMENTS OF THE MATRICES

In this section we will present the details of implementing the Newton-Raphson method for the strain field equations presented in Chapter 3. Referring to eq (B.5), we recast the strain response equation, eq (3.50), as

$$(g_j)_i = (A_0 f_{0_j})_i + (A_1 f_{1_j})_i - 2\mu\varepsilon_{g_j} , \tag{B.7}$$

where i is the iteration counter and j is the gage number. From eq (B.6) we then obtain

$$-(g_j)_i = \left[\frac{\partial g_j}{\partial A_0}\right]_i \Delta A_0 + \left[\frac{\partial g_j}{\partial A_1}\right]_i \Delta A_1 + \left[\frac{\partial g_j}{\partial \theta}\right]_i \Delta\theta \tag{B.8}$$

for the i^{th} iteration. From eq (B.7), we can evaluate the partial derivatives in eq (B.8),

$$\frac{\partial g}{\partial A_0} = f_0 \tag{B.9}$$

$$\frac{\partial g}{\partial A_1} = f_1 \tag{B.10}$$

$$\frac{\partial g}{\partial \theta} = A_0 \frac{\partial f_0}{\partial \theta} + A_1 \frac{\partial f_1}{\partial \theta} . \tag{B.11}$$

Equations (B.9) and (B.10) can be evaluated by inspection from eqs (3.38) and (3.39) for the single-element-gage or eqs (3.46) and (3.47) for the rosette. Equation (B.11) requires performing a partial derivative with respect to θ. For the case of the single-element gage, the required expressions are:

$$\frac{\partial f_0}{\partial \theta} = -0.5\, r_1^{-3/2} \frac{\partial r_1}{\partial \theta} \beta_1 \Big[\cos(\theta_1/2)\, \Lambda + 2\lambda_1 \sin(\theta_1/2)\sin 2\alpha \Big]$$

$$+ r_1^{-1/2}\, \beta_1 \frac{\partial \theta_1}{\partial \theta} \Big[-0.5 \sin(\theta_1/2)\Lambda + \lambda_1 \cos(\theta_1/2)\sin(2\alpha) \Big]$$

$$- 0.5\, r_2^{-3/2} \frac{\partial r_2}{\partial \theta} \beta_1 \Big[-\beta_3 \cos(\theta_2/2) \cos(2\alpha)$$

$$- 2\lambda_1 \sin(\theta_2/2) \sin(2\alpha) \Big]$$

$$+ r_2^{-1/2}\, \beta_1 \frac{\partial \theta_2}{\partial \theta} \Big[0.5\, \beta_3 \sin(\theta_2/2) \cos(2\alpha)$$

$$- \lambda_1 \cos(\theta_2/2)\sin(2\alpha) \Big] \qquad \text{(B.12)}$$

$$\frac{\partial f_1}{\partial \theta} = 0.5\, r_1^{-1/2} \frac{\partial r_1}{\partial \theta} \beta_1 \Big[\cos(\theta_1/2)\, \Lambda - 2\lambda_1 \sin(\theta_1/2)\sin 2\alpha \} \Big]$$

$$+ r_1^{1/2}\, \beta_1 \frac{\partial \theta_1}{\partial \theta} \Big[-0.5 \sin(\theta_1/2)\, \Lambda$$

$$- \lambda_1 \cos(\theta_1/2)\, \sin(2\alpha) \Big]$$

$$+ 0.5\, r_2^{-1/2} \frac{\partial r_2}{\partial \theta} \beta_1 \Big[-\beta_3 \cos(\theta_2/2) \cos(2\alpha)$$

$$+ 2\, \lambda_1 \sin(\theta_2/2)\, \sin(2\alpha) \Big]$$

$$+ r_2^{1/2} \beta_1 \frac{\partial \theta_2}{\partial \theta} \left[0.5 \beta_3 \sin(\theta_2/2) \cos(2\alpha) \right.$$

$$\left. + \lambda_1 \cos(\theta_2/2) \sin(2\alpha) \right] . \qquad \text{(B.13)}$$

For the case of the rosette, the required expressions are:

$$\frac{\partial f_0}{\partial \theta} = - r_1^{-3/2} \frac{\partial r_1}{\partial \theta} \beta_1 \left[- (1+\lambda_1^2) \cos(\theta_1/2) \cos 2\alpha \right.$$

$$\left. - 2\lambda_1 \sin(\theta_1/2) \sin 2\alpha \right]$$

$$+ 2r_1^{-1/2} \beta_1 \frac{\partial \theta_1}{\partial \theta} \left[0.5 (1+\lambda_1^2) \sin(\theta_1/2) \cos 2\alpha \right.$$

$$\left. - \lambda_1 \cos(\theta_1/2) \sin 2\alpha \right]$$

$$+ r_2^{-3/2} \frac{\partial r_2}{\partial \theta} \beta_1 \left[-\beta_3 \cos(\theta_2/2) \cos 2\alpha \right.$$

$$\left. + 2\lambda_1 \sin(\theta_2/2) \sin 2\alpha \right]$$

$$+ 2r_2^{-1/2} \beta_1 \frac{\partial \theta_2}{\partial \theta} \left[-0.5 \beta_3 \sin(\theta_2/2) \cos 2\alpha \right.$$

$$\left. + \lambda_1 \cos(\theta_2/2) \sin 2\alpha \right] \qquad \text{(B.14)}$$

$$\frac{\partial f_1}{\partial \theta} = r_1^{-1/2} \frac{\partial r_1}{\partial \theta} \beta_1 \Big[-(1+\lambda_1^2) \cos(\theta_1/2) \cos 2\alpha$$

$$+ 2\lambda_1 \sin(\theta_1/2) \sin 2\alpha \Big]$$

$$+ 2r_1^{1/2} \beta_1 \frac{\partial \theta_1}{\partial \theta} \Big[0.5\ (1+\lambda_1^2) \sin(\theta_1/2) \cos 2\alpha$$

$$+ \lambda_1 \cos(\theta_1/2) \sin 2\alpha \Big]$$

$$+ r_2^{-1/2} \frac{\partial r_2}{\partial \theta} \beta_1 \Big[\beta_3 \cos(\theta_2/2) \cos 2\alpha$$

$$- 2\lambda_1 \sin(\theta_2/2) \sin 2\alpha \Big]$$

$$+ 2r_2^{1/2} \beta_1 \frac{\partial \theta_2}{\partial \theta} \Big[-0.5\ \beta_3 \sin(\theta_2/2) \cos 2\alpha$$

$$- \lambda_1 \cos(\theta_2/2) \sin 2\alpha \Big] , \qquad \text{(B.15)}$$

where the β_j and k have been defined in Chapter 3 and

$$\Lambda = k\ (\lambda_1^2 - \lambda_2^2) + (1+\lambda_1^2) \cos 2\alpha, \qquad \text{(B.16)}$$

$$\frac{\partial \theta_j}{\partial \theta} = \frac{\lambda_j \sec^2\theta}{1 + (\lambda_j \tan\theta)^2} \quad ; \ j = 1,\ 2 \qquad \text{(B.17)}$$

$$\frac{\partial r_j}{\partial \theta} = - \frac{y_g \cot\theta \csc^2\theta}{\left[\cot^2\theta + \lambda_j^2\right]^{1/2}} \quad ; \ j = 1,\ 2\ . \qquad \text{(B.18)}$$

Using eqs (B.6) - (B.11) we can form the following system of

equations linear in the increments ΔA_0, ΔA_1, and $\Delta\theta$ for the i^{th} increment:

$$\begin{bmatrix} -g_1 \\ -g_2 \\ \cdot \\ \cdot \\ \cdot \\ -g_n \end{bmatrix} = \begin{bmatrix} (f_0)_1 & (f_1)_1 & (A_0f'_0+A_1f'_1)_1 \\ (f_0)_2 & (f_1)_2 & (A_0f'_0+A_1f'_1)_2 \\ \cdot & \cdot & \cdot \\ \cdot & \cdot & \cdot \\ \cdot & \cdot & \cdot \\ (f_0)_n & (f_1)_n & (A_0f'_0+A_1f'_1)_n \end{bmatrix} \begin{bmatrix} \Delta A_0 \\ \Delta A_1 \\ \Delta\theta \end{bmatrix}, \qquad \text{(B.19)}$$

where for brevity we have dropped the iteration counter i and used primes to denote the derivatives with respect to theta. Writing eq (B.19) in matrix form we obtain

$$\mathbf{b} = \mathbb{H}\,\mathbf{x}. \qquad \text{(B.20)}$$

Equation (B.20) is a linear least squares problem which is solved using the methods of Appendix A. Upon solution of the system we revise the values of A_0, A_1, and θ and continue on to the next iteration step. We then repeat the procedure until the changes in A_0, A_1, and θ are small and the convergence criteria of eq (3.60) is satisfied.

REFERENCES

[B.1] Seber, G. A. F. and Wild, C. J., **Nonlinear Regression**, Wiley and Sons, New York, NY (1989).

[B.2] Rheinboldt, W. C., **Methods for Solving Systems of Nonlinear Equations**, Society for Industrial and Applied Mathematics, Philadelphia, Pennsylvania (1974).

[B.3] Vanderplaats, G. N., **Numerical Optimization Techniques for Engineering Design**, McGraw-Hill, New York, New York (1984).

BL-114A
(5-90)

U.S. DEPARTMENT OF COMMERCE
NATIONAL INSTITUTE OF STANDARDS AND TECHNOLOGY

BIBLIOGRAPHIC DATA SHEET

1. PUBLICATION OR REPORT NUMBER
NISTIR 3952

2. PERFORMING ORGANIZATION REPORT NUMBER

3. PUBLICATION DATE
September 1990

4. TITLE AND SUBTITLE

Study of Static and Dynamic Fracture Using Strain Measurements

5. AUTHOR(S)

John R. Berger and James W. Dally

6. PERFORMING ORGANIZATION (IF JOINT OR OTHER THAN NIST, SEE INSTRUCTIONS)

U.S. DEPARTMENT OF COMMERCE
NATIONAL INSTITUTE OF STANDARDS AND TECHNOLOGY
BOULDER, COLORADO 80303-3328

7. CONTRACT/GRANT NUMBER

8. TYPE OF REPORT AND PERIOD COVERED

9. SPONSORING ORGANIZATION NAME AND COMPLETE ADDRESS (STREET, CITY, STATE, ZIP)

10. SUPPLEMENTARY NOTES

11. ABSTRACT (A 200-WORD OR LESS FACTUAL SUMMARY OF MOST SIGNIFICANT INFORMATION. IF DOCUMENT INCLUDES A SIGNIFICANT BIBLIOGRAPHY OR LITERATURE SURVEY, MENTION IT HERE.)

The analysis of strain fields surrounding both stationary and propagating cracks is presented. Series expansions of the static and dynamic strain fields are developed. Gage orientation angles are then studied to optimize the strain response. The orientation angles are found to be dependent on gage type and material.

Algorithms are developed which use the temporal or spatial strain variations to extract fracture parameters. The accuracy of the parameter determinations is shown to be excellent, and limits are placed on the validity of the developed methods. The methods are then applied to the analysis of a large scale crack arrest test conducted in a pressure vessel steel. The behavior of the crack-tip position with time and the propagation toughness with time, temperature and position are determined. From this information, details of the conditions at crack arrest are extracted. The propagation toughness-crack-velocity relation is then constructed.

12. KEY WORDS (6 TO 12 ENTRIES; ALPHABETICAL ORDER; CAPITALIZE ONLY PROPER NAMES; AND SEPARATE KEY WORDS BY SEMICOLONS)

13. AVAILABILITY

X	UNLIMITED
	FOR OFFICIAL DISTRIBUTION. DO NOT RELEASE TO NATIONAL TECHNICAL INFORMATION SERVICE (NTIS).
	ORDER FROM SUPERINTENDENT OF DOCUMENTS, U.S. GOVERNMENT PRINTING OFFICE, WASHINGTON, DC 20402.
X	ORDER FROM NATIONAL TECHNICAL INFORMATION SERVICE (NTIS), SPRINGFIELD, VA 22161.

14. NUMBER OF PRINTED PAGES
188

15. PRICE

ELECTRONIC FORM